November 2020

# Tuning Degradation and Cell Adhesion in Next Generation Resorbable Implants

Ufuomaroghene Ikoba
*University of South Florida*

# Tuning Degradation and Cell Adhesion in Next Generation Resorbable Implants

by

Ufuomaroghene Ikoba

A dissertation submitted in partial fulfillment
of the requirements for the degree of
Doctor of Philosophy in Biomedical Engineering
Department of Medical Engineering
College of Engineering
University of South Florida

Co-Major Professor: Ryan Toomey, Ph.D.
Co-Major Professor: Nathan Gallant, Ph.D.
William Lee III, Ph.D.
Piyush Koria, Ph.D.
Julie Harmon, Ph.D.

Date of Approval:
November 13, 2020

Keywords: Polymers, Crystallization, Surface Coatings, Poly(lactic-co-glycolic acid), Osteoblast Characterization

**Acknowledgements**

I would like to thank my family, friends, advisors. I would like to say a sincere thank to Dr. Ryan Toomey and Dr. Nathan Gallant for their support and contributions throughout the course of this program. I thank my committee members, Dr. Piyush Koria, Dr. William Lee, and Dr. Julie Harmon for guidance and support.

I would like to thank Mr. Bernard Batson, the Alfred P. Sloan Foundation, McKnight Dissertation Fellowship, and ConMed Corporation for the support of this work. I like to say thank you to Dr. Yusuf Emirov, Robert Tufts, and Sclafani Louis-Jeune from the Nanotechnology Research Education Center (NREC) for their help with atomic force imaging and x-ray diffraction. Thank you to all my fellow lab mates, and colleagues in the department of Medical Engineering and Chemical and Biomedical Engineering.

## Table of Contents

## List of Figures

## Abstract

Osteoarthritic and bone degenerative diseases are expected to grow immensely as the aging population, 65 years and older increases. Orthopedic implants are one sub-class of medical devices that are used to treat bone breaks and fractures. Traditionally, internal fixation implants are manufactured using titanium or stainless steel. Magnesium, a bioresorbable and biodegradable material, has been proposed as an alternative to titanium and stainless steel. The goal of this research is to control the degradation behavior of magnesium implants by developing crystallized thin poly(lactic acid) copolymer films as protective coatings. To do this, this work was divided into two aims. Aim I focused on characterizing the crystallization and degradation behavior of the films. Aim II focused on investigating the adhesion behavior of MC3T3 cells to ultrathin films. PLGA films ranging from 50nm to 200nm were prepared by spin casting and were either isothermal annealed to obtain crystallization or thermally erased to remove sample history. To test for degradation, films were immersed in simulated body fluid at 37°C and their dry mass was measured weekly. The glass transition, melt temperature, and thermal expansion coefficient was determined by ellipsometry on a heating stage. The surface morphology of the films was evaluated using atomic force microscopy. The adhesion strength was measured using the spinning disk apparatus. For 200nm films, the glass transition temperature on cooling was 59°C. The degree of crystallization increased with longer annealing times and the films reached maximum crystallinity by five days. The degree of crystallization raised the thin film melt temperature by 6°C, but the glass transition temperature remained unaffected by crystallization.

Crystallized films eroded three times slower than thermally erased films, indicating that crystallization can tune the degradation rate of PLGA thin films. Lastly, the adhesion strength of MC3T3 cells increased by 1.5 times when hydroxyapatite was incorporated into the films. Future work should include degradation testing of magnesium coated with crystallized hydroxyapatite-PLGA films.

# Chapter 1: Introduction

## 1.1 Project Motivation and Significance

By 2060, it is expected that the number of Americans 65 and older will double and make up 23.4% of the total population [1]. The aging population, ages 65 and over are at higher risk for bone diseases and arthritic damages. The decrease in bone mineral and loss of bone density results in higher frequency of fractures, breaks and osteoporosis associated with aging [2, 3]. As a result of a fracture, the bone becomes less capable to bear weight, is under greater strain due to the fracture gap and the area is more susceptible to infection, bleeding, and hypoxia because the vascular system of the bone becomes disrupted and exposed. The body's natural response to fracture healing is to restore hemostasis by stimulating cytokines and producing platelets and fibrin using the coagulation cascade. Afterwards, tissue regeneration is stimulated as necrotic tissue is removed [4, 5].

In addition to the deliberating effects of osteoporosis on bone health, it is also important to consider the contribution of environmental factors to the prevalence of fractures. The energy that is generated from one fall is enough to severely damage various bones in the body, such as in the wrist, ankle, and fingers. 80% of fractures are attributed to falling [6]. There are several factors to consider that can result in a fall. For example, fluctuations in blood pressure, weakening of muscle, motor, and balance skills, an unbalanced diet, and mental health diagnosis

make elderly patients more vulnerable to falls. Additionally, footwear, prescribed medication and reduced grip strength can all result in a fall [7].

Globally, 40% of the population are exposed to a lifetime risk of fractures and every three seconds fractures occur [8]. As a result, surgery costs and surgery recovery time have a tendency of being high and long. The average hospitalization cost for an elderly patient who has an orthopedic surgery is $20,000 [9]. Considering the total aging population, the percentage of risk of fractures and hospital costs, the total cost of healthcare for orthopedic surgeries could be projected to be close to $3 trillion by 2060. From 2008 to 2025, the United States GDP for national health care spending costs is expected to increase by more than 50%, while 5% of the GDP will be spent on treatment of musculoskeletal diseases [10, 11]. It is also important to consider that the productivity losses due to surgery and recovery from orthopedic procedures are high and can be greater than the overall costs of the surgery [12]. Additionally, 1.2 to 2% of surgeries are from infections from the implantation site or from the surgery, and as a result these infections can triple the costs of hospitalization, rehabilitation, and recovery time [13, 14].

Current technology for treating ortho-related diseases has traditionally been limited to titanium and stainless steel for implants. The gap for bone compatible materials can be filled by magnesium because magnesium is a mineral naturally found in the body, biodegradable, and bioresorbable [15]. However, the shortcoming of magnesium is that it corrodes rapidly upon exposure to water.  Therefore, this dissertation seeks to provide a solution to the rapid degradation of magnesium by utilizing biodegradable polylactic acid copolymers as protective coatings.

## 1.2 Project Objective and Research Aims

The objective of this dissertation was to develop and investigate the potential of thin polylactic acid copolymers as surface coatings for bioresorable implants. We hypothesized that crystallizable thin films can control degradation and improve osteoblast adhesion at the implantation site. To test this hypothesis, this dissertation was divided into three aims: Aim I, Aim II, and Aim III.

### 1.2.1 Aim I

The purpose of aim I was to characterize the crystallization and degradation behavior of poly(lactic-co-glycolic acid), PLGA, thin films. PLGA films were prepared between 50nm to 200nm using spin casting on silicon wafers. The percent crystallization in the films was varied and controlled by isothermal annealing between 10 minutes and five days. Characterization of the film thickness and crystallization behavior was performed by ellipsometry, grazing incidence x-ray diffraction and atomic force microscopy. Additionally, by performing a heating and cooling scan, the melt temperature, thermal expansion coefficient, and the glass transition temperature on heating and cooling was determined.

To better understand how thin films deviate from their bulk counterparts, bulk PLGA was investigated following similar experimental conditions of thin films. Bulk PLGA was thermally erased to remove sample history and isothermally annealed for six hours and up to seven days. The glass transition temperatures and the melt temperatures were evaluated using differential scanning calorimetry. The results of the bulk studies were compared to the results of the thin film experiments.

### 1.2.2 Aim III

To investigate the degradation behavior of crystallized and thermally erased PLGA, 200nm films were incubated at 37°C in simulated body fluid. The changes in the dry thickness and refractive index were measured weekly using ellipsometry. The surface morphology of crystallized films and thermally erased films were evaluated using atomic force microscopy at the beginning and end of the degradation studies.

### 1.2.3 Aim II

The purpose of aim II was to investigate the role of crystallization and hydroxyapatite in thin PLGA films in improving the adhesion strength of osteoblast cells. Hydroxyapatite nanopowder was incorporated into the polymer solution and sonicated to ensure dispersion of the hydroxyapatite nanoparticles in the polymer. Hydroxyapatite-PLGA films were prepared at 200nm film thicknesses using spin casting. The hydroxyapatite-PLGA films were crystallized by isothermal annealing at 100°C or thermally erased at 150°C.

MC3T3 cells were cultured in an Alpha-MEM growth media containing fetal bovine serum, and penicillin/streptomycin in a 37°C incubator with 5% CO2. Cells were passaged at confluency and then passaged onto 25mm circular glass coverslips. To prevent the growth of bacteria, coverslips were disinfected with a bleach and water solution and the medium was changed regularly. Cells were adhered onto the surfaces of the hydroxyapatite films for 24 hours prior to adhesion strength testing.

The adhesion strength of MC3T3 cells were evaluated by using the spinning disk apparatus in dextrose spinning buffer. Cells were spun at speeds as high as 5000 rpm. Cells were fixed and stained using a formaldehyde, triton x-100, and an ethidium homodimer dye. The adherent cell fraction was counted by using fluorescent microscopy and SigmaPlot. The surface roughness and morphology of the hydroxyapatite films were analyzed using atomic force microscopy.

## Chapter 2: Background

Over the past several decades, there have been major improvements in the materials used for implantable orthopedic devices. There are different classes of orthopedic devices, for example, there are internal fixation devices and devices used in total replacement procedures. The primary focus of this dissertation concerns the use of internal fixation devices, such as screws, plates, and pins that are used to hold the bone in place for a short period of time until the bone heals or until the implant is removed. Internal fixation devices are commonly used in fractures, brakes, and temporary adjustments of the bone. The main advantage of internal fixation devices is that they are not permanent. In several cases, following healing of an injury, most patients are left with the screw, plates or pins inside their body even though they are no longer needed. Alternatively, the orthopedic specialist and the patient may proceed with a secondary surgery to remove the fixation devices. A secondary surgery usually results in more costs, recovery time and loss of work and employment for a period of time. Resorbable implants can provide an alternative solution to secondary surgeries and unremoved internal fixation devices.

Resorbable implants are made of materials that can be naturally resorbed by the body. An example of a resorbable material is magnesium. Magnesium is a naturally occurring mineral in the body. Magnesium serves a very important function to preventing osteoporosis by increasing the bone mineral density and is used in the formation of bone. In addition to its bone aiding

processes, magnesium also helps to regulate blood pressure and sugar, nerve and muscle function, and is used in energy production. Also, 65% of magnesium is located in the bone [16-18]. The absorption pathway of magnesium in the body is transportation as an ion into the small intestine. Here, magnesium is either transported via the paracellular mechanism by solvent drag or the electrochemical gradient or by TRPM, transient receptor potential channel melastatin member via the transcellular pathway and excreted by the kidneys or stored in bone [17, 18].

Given the current information and knowledge base, magnesium presents itself as a strong candidate as a resorbable internal fixation device material on the basis that its degradation rate can be controlled. To optimize its functionality, it is paramount for the magnesium degradation rate to match the bone healing rate. In this way, there can be a controlled release of magnesium into the body, absorbed by the intestine and stored in the bone. As the storage of magnesium increases in the body upon implant degradation, it could help stimulate bone regeneration to compensate for the loss of bone from fractures or breaks. Matching of the degradation and healing rate is also essential to ensure that the bone has completely healed before the internal fixation device dissolves. Lastly, because magnesium is a naturally occurring mineral, the by-products of degradation and resorption could be considered biocompatible and unharmful to the body. In contrast to traditional materials like titanium, cobalt, or stainless steel, the human body already has systems and pathways in place to handle the transport of magnesium as discussed earlier.

There are several factors that affect the performance of biomedical implantable materials in the human body. These factors generally include, mechanical strength, corrosion rate, biodegradability, biocompatibility, stress shielding, and Young's modulus. Orthopedic implants are generally made from titanium, stainless steel, cobalt, and more recently polymers. Given the long history of metallic implants, it is crucial for the purposes of this discourse to make a comparative analysis concerning the overall performance of some of these materials in comparison to magnesium and bone.

Although, titanium, stainless steel, cobalt, and magnesium are considered biocompatible, only magnesium is considered as a biodegradable metal. As such, compared to other metals, magnesium is one of the few metals that is bioresorbable [19]. The shortcoming of titanium and stainless steel and its alloys is that as it degrades the metallic particles can be considered toxic or allergic and can lead to increase inflammation of the injury site or biofilm formation [15]. Magnesium also has the lowest density, Young's Modulus, stress-shielding effect against other metals when compared to bone [20]. The Young's Modulus of magnesium is 41 GPa and its density is 1.74 g/cm$^3$. Bone has a density and Young's Modulus of 2 g/cm$^3$ and 23 GPa, respectively. Titanium has a density and Young's Modulus of 4.4 g/cm3 and 114 GPa, respectively. Stainless steel has a density of 8.1 g/cm3 and a Young's Modulus of 205 GPa [15, 21-23]. Magnesium possess several advantages as a resorbable internal fixation device, however, the greatest limitation of magnesium still persists – its rapid degradation rate.

One method to overcome the shortcoming of the rapid degradation of magnesium is by using polylactic acid copolymers as surface coatings on the magnesium implants. Polylactic acid can help to tune the degradation of magnesium, by acting as the first degradable layer of the implant and as a barrier to water penetration to magnesium, while also participating in drug delivery. Poly(lactic-co-glycolic acid) is also advantageous because it is biodegradable, biocompatible, and FDA approved and can be readily available in the medical device industry [24]. PLGA and PLA are a class of semi-crystalline hydrophobic polymers that can be synthesized by azeotropic dehydration condensation, ring opening polymerization, and polycondensation [25-27]. PLGA exists stereochemically with either D or L enantiomers, containing glycolic acid and lactic acid units [28, 29]. Polylactic acid and its copolymers are generally characterized by their glass transition temperature, melt temperature, Young's Modulus, and tensile strength. The glass transition temperature of bulk PLA ranges between 43°C-80°C and the melt temperature ranges between 120°C-190°C [30-33]. Several factors can affect their thermal and mechanical properties, such as the degree of crystallization, copolymer ratio, and the molecular weight. Bigg reports that increasing the copolymer ratio from 80/20 (L-/D,L) PLA to pure PLA raised the glass transition temperature by 7°C and increased the melt temperature by up to 53°C [34].

Polylactic acid is most commonly synthesized using polycondensation or ring-opening polymerization. Polycondensation involves the removal of water using high temperatures and vacuum, polycondensation of the oligomer groups, and melt or solution condensation of the polymer. The end result of polycondensation is polymers that have low-to-medium molecular weights. Chain extenders or esterification-promoting agents can be used to increase the

molecular weight via the polycondensation method [35, 36]. Ring-opening polymerization involves using a catalyst for ring opening of the lactide group (lactic acid cyclic dimer). Ring-opening involves process steps that include polycondensation, depolymerization, and ring opening polymerization. Polymers produced by ring-opening polymerization have greater purity and high molecular weights. In the case for PLGA, PLGA is synthesized by co-polymerization of the cyclic dimers of lactide (lactic acid) and glycolide (glycolic acid) using ring opening polymerization. PLGA is formed through ester bonds linkages under the presence of a catalyst, such as stannous octoate or stannous chloride [37, 38].

PLGA has found use in a variety of biomedical applications. PLGA has been studied extensively for their use in drug delivery, vaccine therapy, vasculogenesis, and nerve and tissue regeneration applications, and even as dissolvable stents [39-46]. PLGA can be designed to contain hydrophobic or hydrophilic molecules and have optimal release times that match the degradation rate of the polymer. As a drug delivery carrier, PLGA can encapsulate a product, ions, or chemical and release the drug over time. Lin et al. developed a PLGA microsphere system to control the release of magnesium oxide nanoparticles [47]. In an eight week period, there was a 60% increase in the percentage of new bone volume from the PLGA-magnesium oxide-alginate core-shell microspheres (compared to the sham control), which suggests that PLGA microspheres are effective in promoting bone regeneration by releasing of magnesium ions [47]. One of the risks of implantation surgery is the formation of a bacterial biofilm layer around the implant site that can result in infections. Incorporation of cinnamaldehyde, an essential oil, into a thin PLGA film resulted in the inhibition and reduction of *E. coli* and *S.*

*aureus* formation [48]. Not only can PLGA thin films be used as drug delivery vesicles but they can also be used in controlling the spread of infection at the surgical implantation site.

There have been several works that have investigated the capability and involvement of polymer coatings in the reduction of the degradation rate of magnesium alloys [49-55]. Lakalayeh et al. demonstrated that when WE43 magnesium alloy was coated with both PLGA and PLA coatings, the corrosion resistance was higher than the bare magnesium, the intensity of resistance was reduced by half (compared to bare magnesium), and the HUVEC cell viability was maintained at 70% and higher within two days, while the cell viability on bare magnesium was 10% or less [56]. In another study by Li et al., Mg-6Zn magnesium alloy coated with 2% and 4% PLGA maintained close to 0 $mg/cm^2$ weight loss, while bare Mg-6Zn lost about 20 $mg/cm^2$ in the first 20 days of degradation in a NaCl solution, and the degradation rate was at least 200 times faster for uncoated magnesium [57]. These studies demonstrate that PLGA has the potential to serve as effective coatings on magnesium alloys, while promoting cell viability by modification of the PLGA thickness. However, more work should be conducted and is the focus of the present dissertation to evaluate the role of crystallization in ultrathin films to tune degradation properties of PLGA.

# Chapter 3: Tuning the Crystallization Behavior of Thin Poly(D,L-lactic acid) Copolymers

## 3.1 Introduction

Orthopedic implants, such as rods, screws, and plates are commonly made out of titanium or stainless steel alloys. More recently, polymers, such as polylactic acid (PLA) and poly(lactic-co-glyolic acid) (PLGA), have become more widespread as alternative materials for implantable devices. Some of the key advantages of using polylactic acid and PLGA are that these materials are biocompatible and biodegradable [58], [59]. In tissue engineering, surface coatings can help to extend the longevity of the implants by providing an additional layer of protection from the harsh environments of the body. Though widely studied as bulk or scaffolds, characterizing the morphology and thermal behavior of thin polylactide films have become increasingly important. Much work has been done to characterize the glass transition temperature of polymers, such as polystyrene. However, more work is needed to characterize the glass transition temperature upon heating and the melting behavior of polylactide copolymer films. Modification of the thin film by crystallization and thickness can yield crystals of different orientations and morphologies, which could affect the melt transition and the recrystallization process [60-63]. In a study by Fitz et al., they observed that increases in the isothermal crystallization of poly(L-(-)-lactide) yielded an increase in the glass transition temperature under unconstrained conditions. Although, under partially constrained conditions, the glass transition temperature of PLLA reduced [64].

Glass transition temperature is also known to be affected by film thickness and interfacial interactions [65-68]. For ultrathin films, many have reported a sensitivity of the relaxation time and the glass transition temperature to the cooling rate [69-76]. Moreover, during cooling there is greater freedom for contraction of the film [77]. Tsui et al. reported that changes in the thermal expansion coefficient in thin films occurred in a small window between the glass and liquid regime [67]. Interactions between the polymer and the substrate are known to effect the glass transition temperature, where increasing the thickness can led to a weaker dependence on the polymer-substrate interaction [68]. In their study, Roth et al. demonstrated that regardless of the addition of a polystyrene capping layer to tune the interactions of the poly(2-vinylpyridine) to a silica substrate, the substrate interactions dominated in influencing the glass transition temperature [78].

The unit structure of polymer chains in thin films can enhance the polymer-substrate interaction and can thus reduce the mobility of the chain structure. Polymer mobility can be improved by increasing the volume of the free surface and by the addition of chain groups on the free surface [78-84]. Given the extensive amount of information available on the polymer mobility dynamics on the glass transition temperature, more investigation is needed to understand the impact of crystallization and polymer mobility on the melt, and glass transition temperatures of polylactide copolymer films. The purpose of this chapter is to investigate the effects of crystallization and thickness on the melt temperature, heating glass transition temperature and the cooling glass transition temperature in thin poly(lactic-co-glycolic acid) films and in the bulk. The influence of crystallization on the coefficient of thermal expansion will also be discussed.

### 3.2 Materials and Methods

Poly(D,L-co-glycolic acid) (85L/5D/10G), PLGA, was obtained from ConMed Corporation [Mw:1259.34 kg/mol; Polydispersity: 1.955 determined using a polystyrene standard] (figure 3.1). One sided polished silicon wafers were cleaned by plasma etching. Films were prepared in chloroform and spin coated on plasma etched silicon wafers at a speed of 3000 rpm. After spin coating, samples were annealed at 100˚C for 24 hours and five days. The thickness and index of refraction were characterized by ellipsometry.

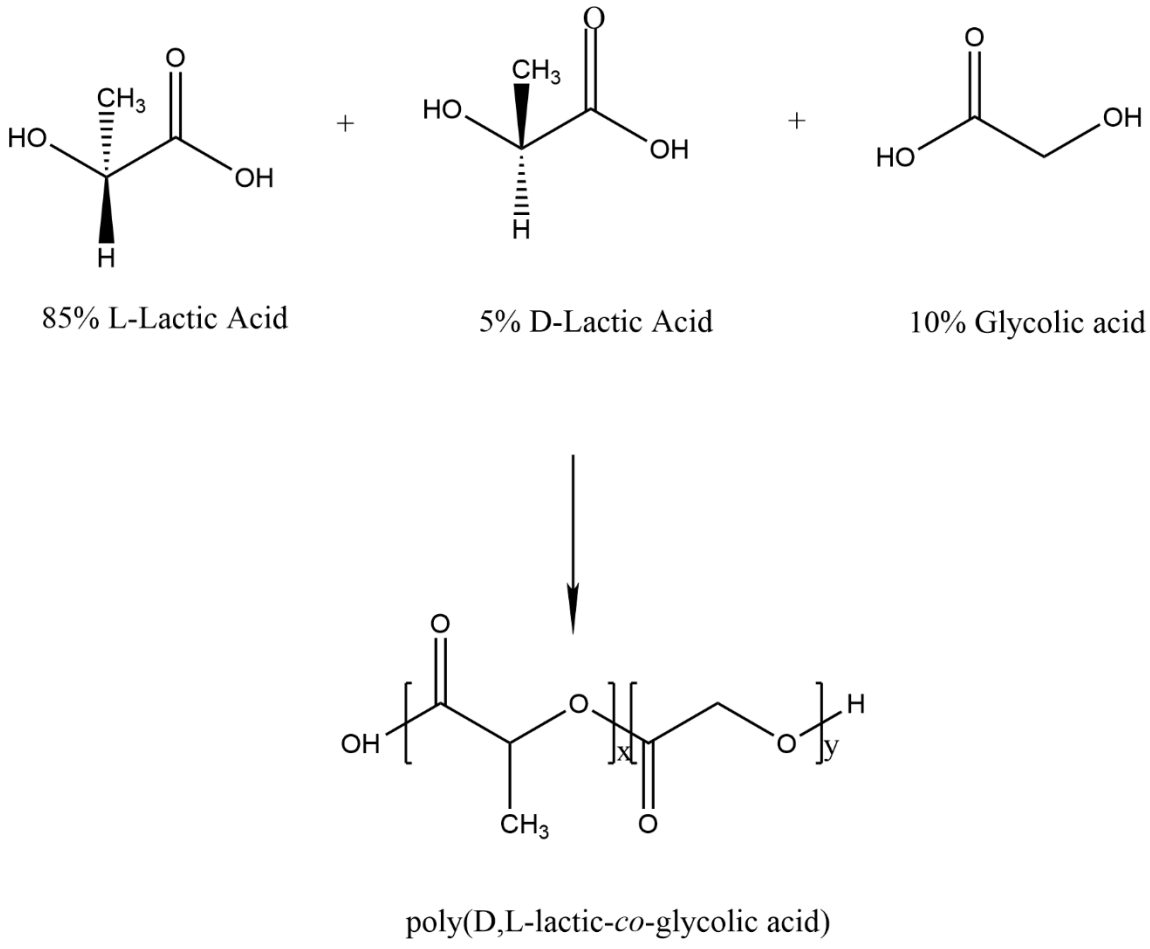


Figure 3.1 The structure of 85L/5D/10G poly(D,L-lactic-*co*-glycolic acid)

### 3.2.1 Ellipsometry

A home-built variable-angle rotating compensator ellipsometer was used at a fixed angle of incidence. The ellipsometer used a He-Ne laser light source with a wavelength, λ, of 633nm. Films were heated on a heating stage from 30˚C to 150˚C at a heating rate of 10˚C/min and cooled from 150˚C to 30˚C at a cooling rate of about 10˚C/min, while psi and delta were recorded simultaneously. Psi represents the amplitude ratio and delta is the phase difference. By obtaining psi, Ψ and delta, Δ, experimentally, the index of refraction, $N_1$, and the film thickness, d, could be solved. The equations account for the air-film interface and the film-substrate interface. ρ is the reflection ratio obtained from psi and delta, $\theta_0$ is the incident angle, and β is the film phase thickness. The notation of 0 refers to the ambient environment, 1 refers to the film and 2 refers to the substrate. The following Drude and Snell law equations were used to fit psi and delta to obtain the film thickness and refractive index [77, 85].

$$\rho=\tan\psi \exp^{j\Delta} \tag{3.1}$$

$$\rho = R_s/R_p \tag{3.2}$$

$$N_0\sin\Theta_0=N_1\sin\Theta_1=N_2\sin\Theta_2 \tag{3.3}$$

$$\beta = 2\pi(d/\lambda)N_1\cos\theta_1 \tag{3.4}$$

Figure 3.2 displays the ellipsometry setup that was used to perform heating and cooling scan measurements and dry thickness measurements. A heating stage made out of aluminum was custom built to have heat cartridges and a thermocouple housed inside the stage. The thermocouple was connected to the benchtop controller and to the Labview software on the computer. The connection of the thermocouple to the computer allowed for continuous measurements of the temperature with psi and delta. The films were placed upright on the heating stage and were held in place with flathead screws and washers.

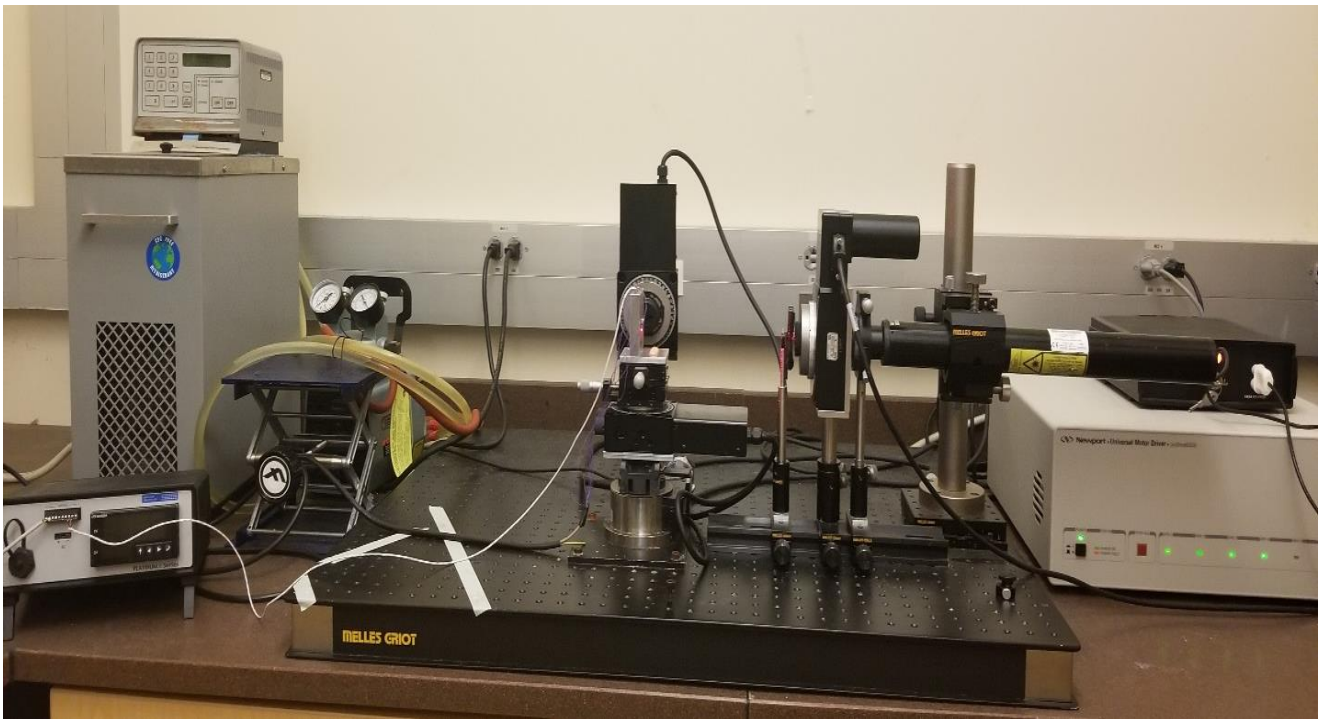


Figure 3.2 The ellipsometer setup for testing film thickness and refractive index

### 3.2.2 Differential Scanning Calorimetry

Differential scanning calorimetry (DSC) was performed on bulk PLGA samples. The DSC chamber contained an enclosed pan of the bulk PLGA and an empty reference pan. The changes in heat flow were measured as a function of temperature. Bulk PLGA samples were heated from 30˚C to 150˚C and cooled from 150˚C to 30˚C both at a heating and cooling rate of 10˚C/min. This was done to match the experimental setup in ellipsometry and to compare the results of the glass transition and melt temperature between the thin film and the bulk state.

### 3.2.3 Grazing Incidence X-Ray Diffraction

Grazing Incidence X-ray diffraction (GIXRD) using a Panalytical X'Pert Pro diffractometer was used to evaluate the crystal behavior of a thin film. The diffractometer was set with an incident omega angle of one degree and a copper anode material with a CuKα of 1.54060 angstroms. The samples were scanned on a 2θ axis with a starting angle of 10˚ and an ending angle of 30˚, a step size of 0.0200 [2θ˚]. Samples were annealed at 100˚C from 10 minutes to five days and compared to samples that were un-annealed.

### 3.2.4 Atomic Force Microscopy

The surface topography of films of 133nm thickness were characterized using atomic force microscopy, AFM, on a heating stage. The 133nm films were initially annealed at 100˚C for 24 hours, thermally erased using the AFM heating stage and then re-annealed at 100˚C for 24 hours. Afterwards, films were heated from 30˚C to 150˚C and cooled from 150˚C to 30˚C both at a rate of 10˚C/min.

### 3.3 Results and Discussion

To confirm the accuracy of the ellipsometry measurements, a 400nm polyethylene oxide, PEO (Mv: 400,000), thin film was used. The published range for the melt temperature for PEO is between 65°C-70°C [86, 87]. As seen in figure 3.3, the melt temperature that was measured for PEO using ellipsometry was within the published range. Therefore, it confirmed that the measurements for the melt and glass transition temperatures for the PLGA thin film samples were accurate using ellipsometry.

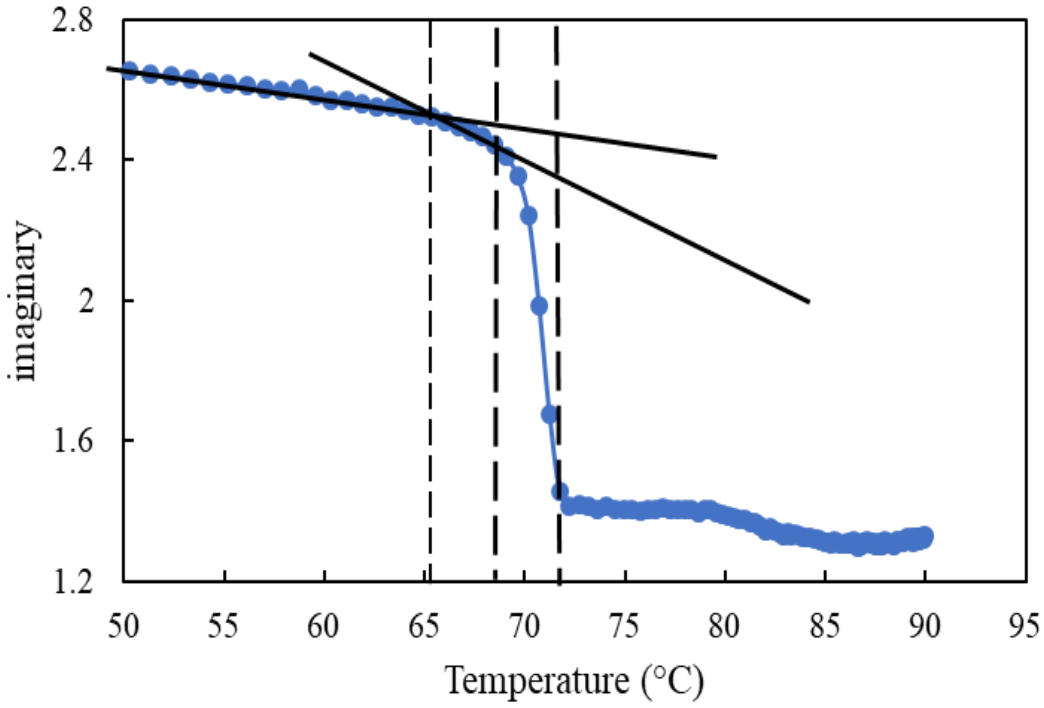


Figure 3.3. The ellipsometry scan of the melt temperature for a 400nm PEO film

Thin coatings of PLGA were spin-cast between 50 and 200 nm followed by isothermal annealing at 100 ˚C for up to 5 days. Figure 3.4a shows two heating and cooling ellipsometry scan cycles for a 200 nm thick PLGA coating that was annealed for 5 days after spin-casting, which corresponds to maximum crystallinity. On the first heating run (10 ˚C/min), as highlighted in Figure 3.4b, two prominent transitions are observed, a transition from the glassy to the rubbery semi-crystalline state and a melting transition to the fully amorphous state. The first transition ($T_{g,h1}$) occurs at a temperature of 53 +/- 1 ˚C, which is determined by the intersection of the asymptotes of the glass and rubbery semi-crystalline states taken between 30 and 50 ˚C and 70 and 90 ˚C, respectively. $T_{g,h1}$ is sometimes classified as the fictive temperature, and it is correlated to the structure of the glass. Here the thermal expansion of the layer increases from 0.05 nm/ ˚C in the glassy state to 0.11 nm/˚C in the rubbery semi-crystalline state.

The second transition, or the melt transition between the rubbery semi-crystalline to the rubbery amorphous state, takes place between 120 ˚C and 145 ˚C, the midpoint ($T_m$) occurring at 137 +/- 1 ˚C. At the midpoint of this transition, the PLGA film experiences a 2% increase in thickness from 206 nm to 210 nm. In the fully melt regime, the thermal expansion increases to 0.20 nm/˚C. Figure 3.4c highlights the first cooling from 150 ˚C to room temperature (also at a rate of 10˚C/min), the thermal contraction stays constant at 0.20 nm/˚C until the transition temperature of ($T_{g,c1}$) of 59 +/- 1 ˚C. In the glassy region, the thermal contraction of the layer is 0.05 nm/ ˚C, roughly equivalent to the value of at the start of the heating run.

Two features from these experimental runs stand out. First, the transition temperature between the glassy and rubbery semi-crystalline state $T_{g,h1}$ upon heating is lower than the associated transition temperature $T_{g,c1}$ upon cooling by 6 ˚C. This observation is consistent with PLA that has been crystallized under constrained conditions, where the transition temperature from the glassy to the rubbery semi-crystalline state was found to up to 30 ˚C less than the fully amorphous sample [64].

Second, during cooling, the film contracts at nearly twice the rate than it expands during heating. At 75 ˚C, the thicknesses between the cooling and heating runs cross. At the end of the cooling run, the thickness is 4 nm less than the thickness at the start of the heating run (194 vs 198 nm). It should be noted that such a cross-over is not always consistently observed. However, the contraction of the coating from the melt to room temperature always overcomes the increase in the coating thickness gained upon melting in the heating run. This phenomenon may be due to the effect of the constraining substrate, which prevents contraction or expansion of the coating laterally to the substrate. On cooling from the annealing, the crystallites frustrate relaxation of the coating leading to excessive free volume compared to an equivalent bulk sample that can contract in all three dimensions. This frustration is responsible for both the cross-over between the cooling and heating runs as well as the diminished value of $T_{g,h1}$ versus $T_{g,c1}$.

On the second heating and cooling run cycle, the thickness vs. temperature curves now almost completely overlap. The expansion coefficient above the glass transition temperature is 0.20 nm/˚C for both runs; however, there is a small discrepancy in the two runs near the glass transition, as shown in Figure 3.4d. The transition temperature $T_{g,h2}$ upon heating is 57 +/- 1 ˚C

and the transition temperature $T_{g,c2}$ upon cooling is 59 +/- 1 ˚C. Interestingly, there is more curvature in thickness vs. temperature near the glass transition upon cooling than during heating. While $T_{g,h2}$ is still less than $T_{g,c2}$, it is now only by 2 ˚C.

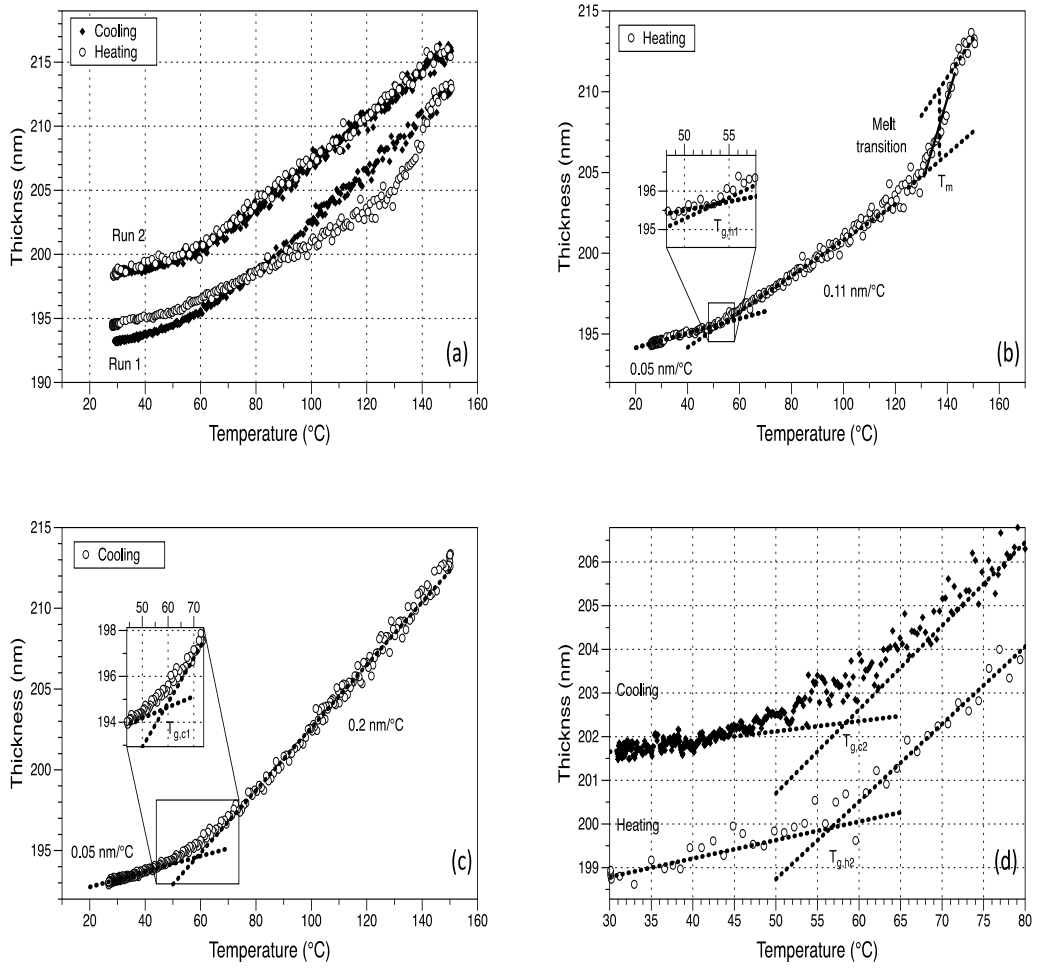


Figure 3.4. (a)Ellipsometry graph of a 200nm PLDGA film, (b)melt temperature, (c)glass transition temperature during cooling, (d)the glass transition temperature between the heating and cooling run.

The linear thermal expansion coefficient [88, 89], $\alpha = \left(\frac{dl}{dT}\right)\frac{1}{l_0}$, for the glass, rubbery semi-crystalline, and amorphous states were 3 +/-1 x $10^{-4}$ /˚C, 5 +/- 1 x $10^{-4}$ /˚C, and 9 +/-1 x $10^{-4}$/˚C respectively (Figure 3.16). Similar values were found for all coatings between thicknesses of 50 nm up to 200 nm for samples annealed for 5 days at 100 ˚C. The literature value of the volumetric thermal expansion of PLA in the melt is 7.4 x $10^{-4}$ /˚C [90]. The corresponding linear thermal expansion coefficient is approximately 1/3 this value, or 2.5 x $10^{-4}$ /˚C. Interestingly, the measured values of 9 +/-1 x $10^{-3}$/˚C in the melt is approximately the same value as the reported volumetric expansion coefficient, suggesting that the amorphous PLDGA is undergoing almost pure one-dimensional expansion during the heating and cooling runs. This is in line with what has also been overserved on ellipsometry measurements of poly(styrene) films [77].

To put the ellipsometry findings into perspective, Figure 3.5 depicts the DSC scan of bulk PLGA that was quenched from 150 ˚C and annealed at 100 ˚C for 5 days to mimic the same thermal history of the 200 nm thick coating, whereas figure 3.6 reflects the DSC scan on cooling. Similar to the first ellipsometry heating scans, two prominent transitions are observed on the first heating run of the DSC. The first transition temperature $T_{g,h1}$between the glassy and rubbery semi-crystalline state occurs at 63 ˚C, or 10 ˚C above the value of the 200 nm film.

In the second transition, there are two pronounced peaks, labeled I and II (figure 3.5). The presence of two melting peaks have also been observed in PLGA (84L/16G). [91] Peak I is representative of the melting of lamellae associated with secondary crystallization and occurs between 115 ˚C and 130 ˚C. Peak II is the melting of the primary lamellae, and it occurs between 130 and 142 ˚C. The melt temperature $T_m$ of the bulk sample is defined at the center of

peak II, which is 138 ˚C, the same melt temperature as observed for the 200 nm coating. The reported enthalpy of melting for crystalline PLA is 93.7 J/g [92].

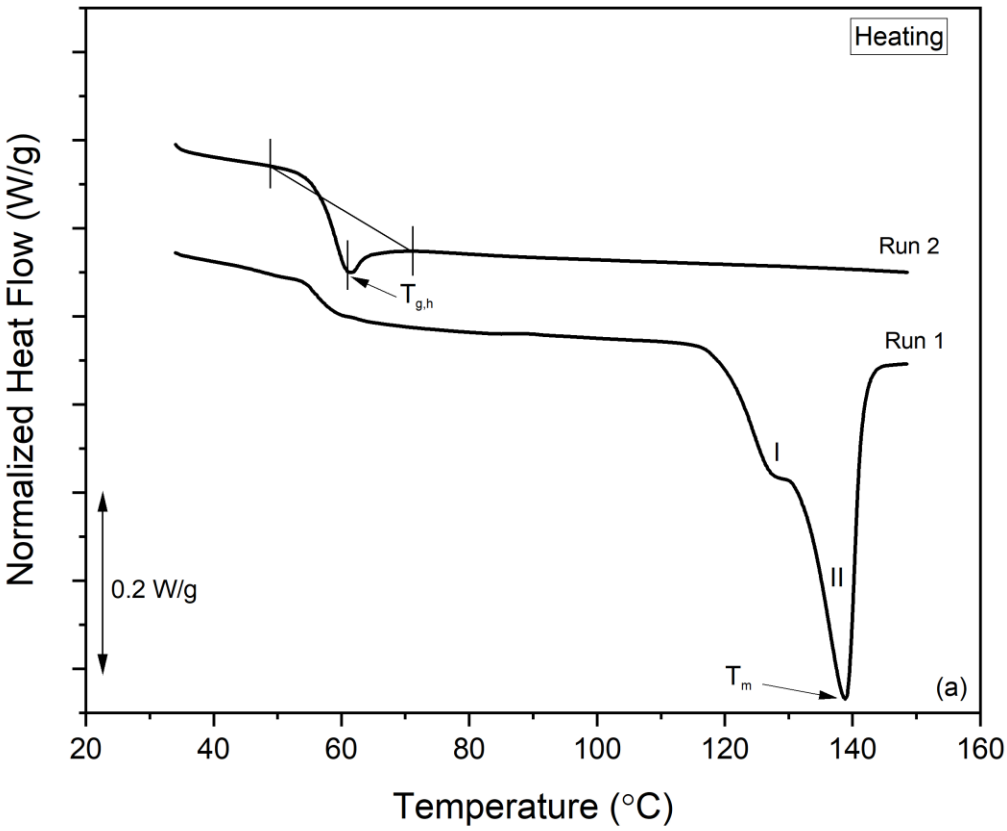


Figure 3.5 A DSC graph of a five day annealed PLDGA undergoing heating, where run 1 is black and run 2 is red. The sample is amorphous on run 2 because there is no presence of a melt peak. I refers to endotherm I and II refers to endotherm II.

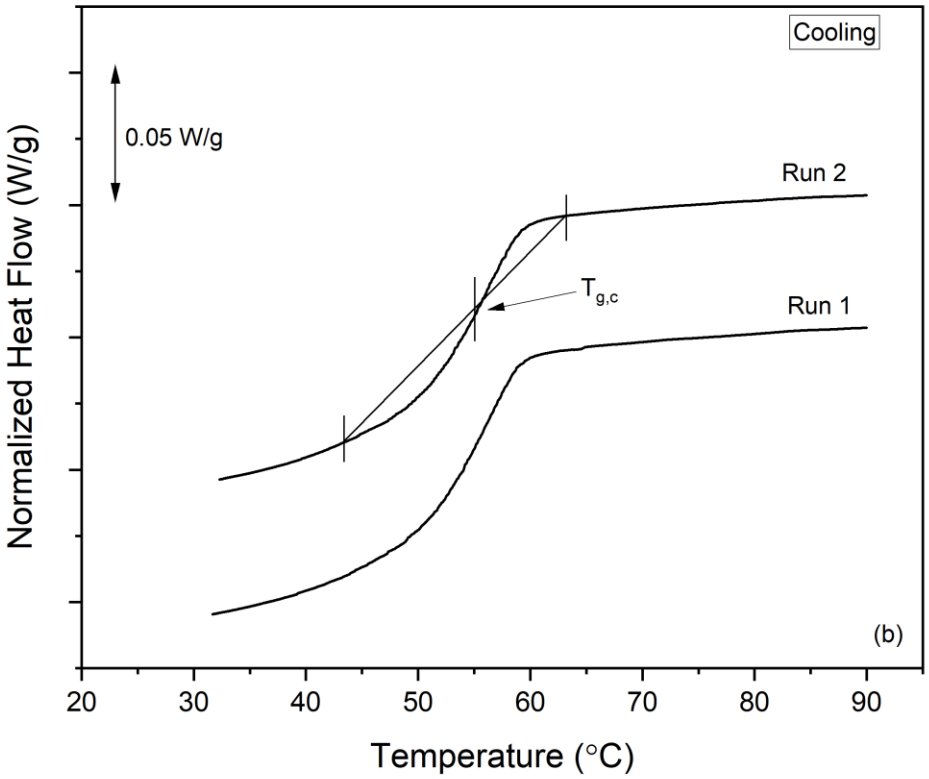


Figure 3.6. A graph of Tg,c and Tg,h on run 2, where all sample history is erased. Tg,c is measured on cooling and Tg,h is measured on heating.

### 3.3.1 Heating and Cooling Rate Dependency in Bulk PLGA

The dependency of the bulk melt temperature and glass transition temperatures on the heating and cooling rate was determined by increasing the rate from 1°C/min to 15°C/min. Unlike the effects of anneal time and crystallization, the melt temperature remained constant at 136.4°C +/- 0.44°C when the heating rate was varied (figure 3.8). $T_{g,h1}$ and $T_{g,h2}$ both increased by 5°C, when the heating rate increased from 1°C/min to 15°C/min (figure 3.8). The increase in $T_{g,h}$ indicated that the glass transition temperature upon heating is a rate-dependent property in bulk PLGA, regardless if sample history was present or not. Although in figure 3.9, it appears that $T_{g,c1}$ and $T_{g,c2}$ are increasing and decreasing with rate, given the standard deviation, $T_{g,c1}$ and $T_{g,c2}$ was determined to be independent of cooling rate.

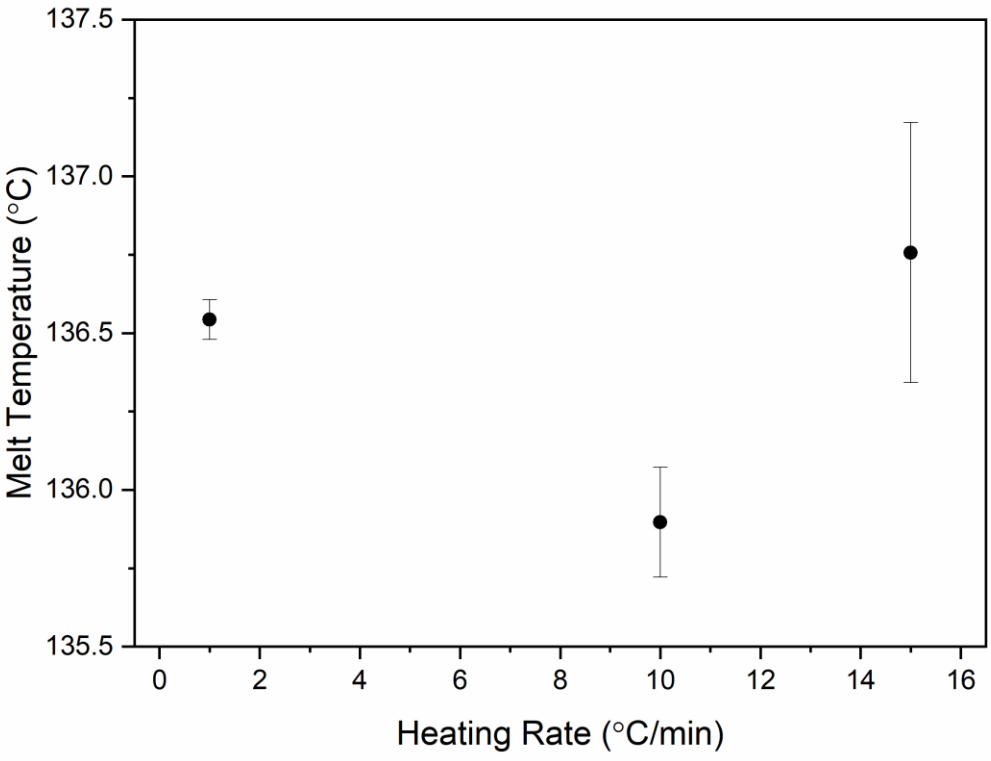


Figure 3.7 Bulk melt temperature remained constant with increased heating rate

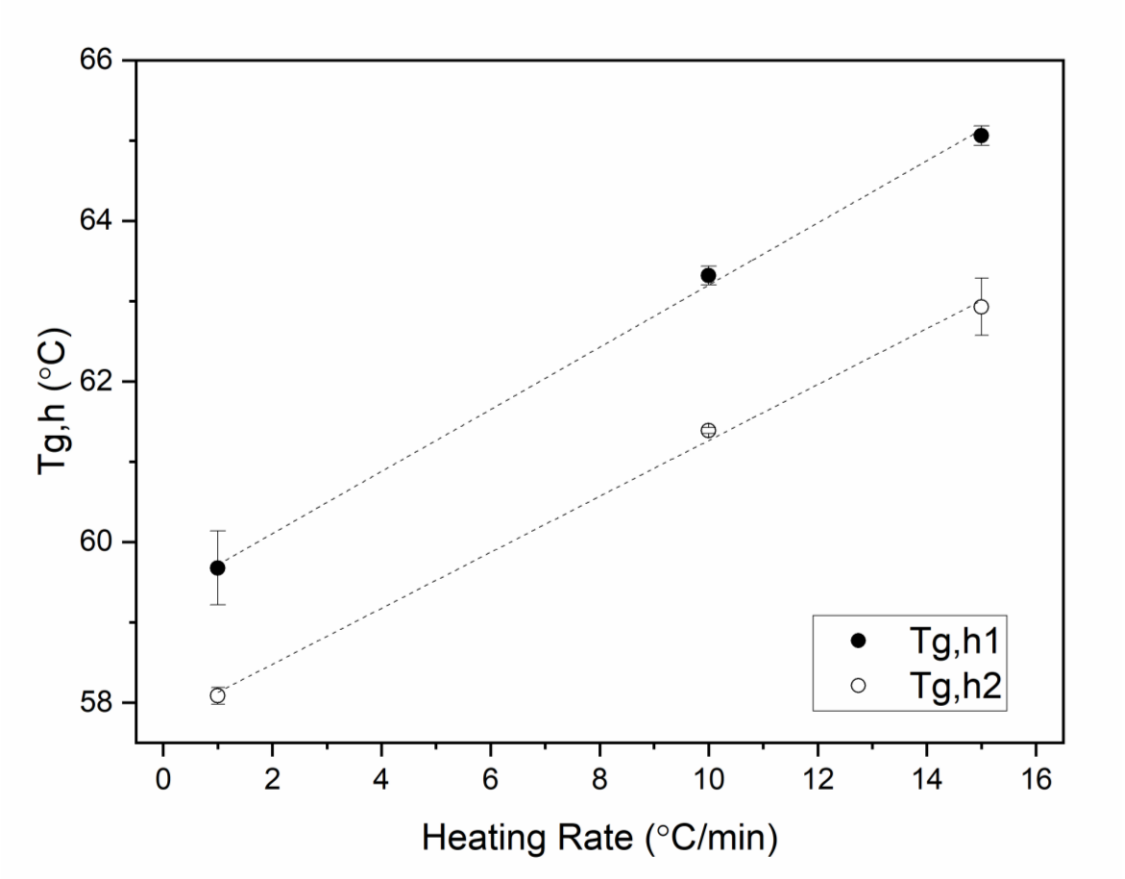


Figure 3.8 The bulk glass transition temperature on heating for both run 1 and 2, Tg,h1 and Tg,h2, increased linearly with heating rate.

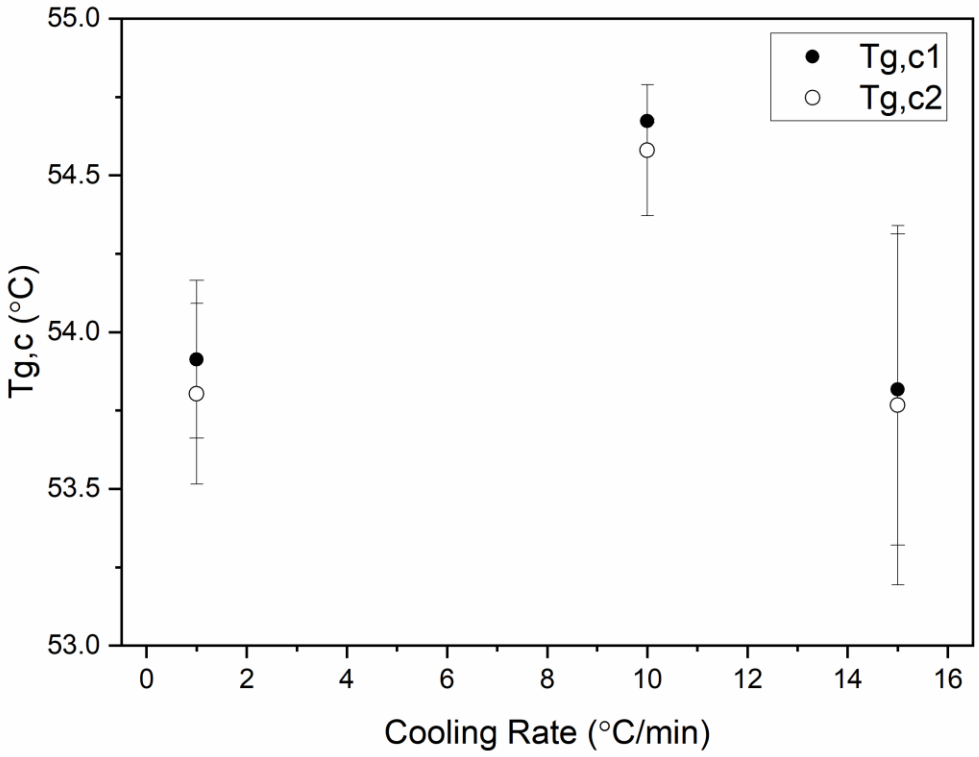


Figure 3.9 The bulk glass transition temperature on cooling during runs 1 and 2, Tg,c1 and Tg,c2 remained constant with increasing cooling rate.

3.3.2 Role of Crystallization in $T_m$, $T_g$, and α

In the first cooling run of DSC, the sample was brought down from the melt state at 150 ˚C to room temperature. In this cooling run, there are no signs of crystallization and the transition from the rubbery to the glassy state occurs at $T_{g,c1}$= 54 ˚C. In the subsequent DSC heating run of the bulk sample, $T_{g,h2}$ is 60 ˚C with no characteristic melt transition. Upon cooling, $T_{g,c2}$ is 54 ˚C. Here it is to be noted that $T_{g,h2} - T_{g,c2}$ = 6 ˚C, whereas in the 200 nm coating, $T_{g,h2} - T_{g,c2}$ = -2 ˚C.

Comparing the ellipsometry and DSC results, the melting transition starts at 115 ˚C. Upon closer examination of the first heating run of the 200 nm PLDGA coating, there is a gradual increase in the thermal expansion of the film from 0.11 nm / ˚C to 0.13 nm/˚C between 100 ˚C and 130 ˚C. To bring this into focus, Figure 3.10 shows the deviation (or residual) between the measured thickness and the expected thickness based on an 0.11 nm/ ˚C expansion coefficient. At approximately 120 ˚C, this deviation shifts to exceedingly positive values, which may be consistent with the Peak I endotherm in the DSC. The effect is relatively small, only accounting for a 1% increase in thickness.

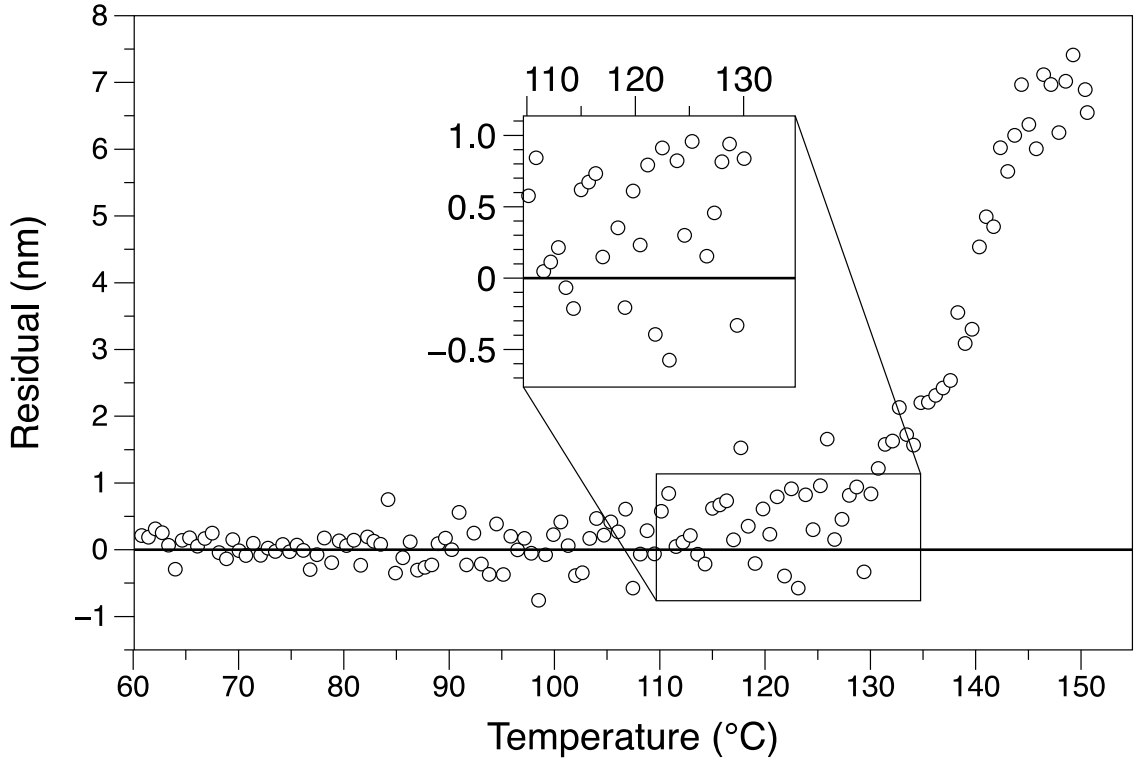


Figure 3.10 Deviation between expected and actual thicknesses for a 200nm film

If we define the beginning of the melt transition at the clear slope change at 130 ˚C, the midpoint is 137 ˚C, as depicted in Figure 3.5. At 137 ˚C, the change in thickness is determined by extrapolating the thickness before melting and the thickness after melting, which can be used to estimate crystallinity. Using the literature values for the densities of amorphous PLA ($\rho_a =$ 1.25 g/cm$^3$) and crystalline PLA ($\rho_c = 1.49$ g/cm$^3$), the density of semi-crystalline PLGA can be estimated as

$$\rho_x = (1 - x)\rho_a + x\rho_c \tag{3.1}$$

Where $\rho_x$ is the density corresponding to a crystalline fraction $x$. If the thickness of the semi-crystalline layer at the start of the melt transition is $L_x$ and the thickness of the amorphous layer at the end of the melt transition the is $L_0$, the relationship between $L_0/L_x$ and $\rho_x/\rho_0$ is

$$\frac{L_0}{L_x} = \left(\frac{\rho_x}{\rho_0}\right)^{1/3} \tag{3.2}$$

which enables determination of $x$. Based on the analysis in Figure 3.4b, the fraction of crystallinity is 0.32, which is remarkably similar to the 0.26 fraction obtained from DSC. Depending on how one selects the baseline for the start of the transition, there can be considerable error in this estimate (+/- 20%). Therefore, the relative degree of crystallization was measured using grazing incidence x-ray diffraction (GIXRD) on 70 nm thick PLDGA coatings. The relative degree of crystallization in the thin films was determined by measuring the area, $A$ , of the diffracted peaks at the various annealing time periods.

$$\frac{x}{x_{5d}} = \frac{A_t}{A_{5d}} \tag{3.3}$$

Where $x/x_{5d}$ is the crystallinity fraction relative to 5 days. 5 days was chosen as the frame of reference, as there is negligible change in crystallinity in both the thin film and bulk polymer after 5 days of annealing. The GIXRD diffraction pattern of a 70 nm film demonstrated that the height of the peaks increased with increasing annealing time. A single peak was observed in all of the diffraction patterns at 16.9˚ [˚2θ] (Figure 3.11). The d-spacing of 5.24Å and the FWHM of 0.7860 [˚2θ] remained constant across all annealing conditions thus suggesting that the size and type of crystal growth remained the same. The diffraction peak of PLGA in this study was consistent with the finding of Vayer et al., who observed a sharp 2θ peak at 16.5° for a 200 nm poly(L-lactic acid) film that was annealed for five minutes at 80°C [93].

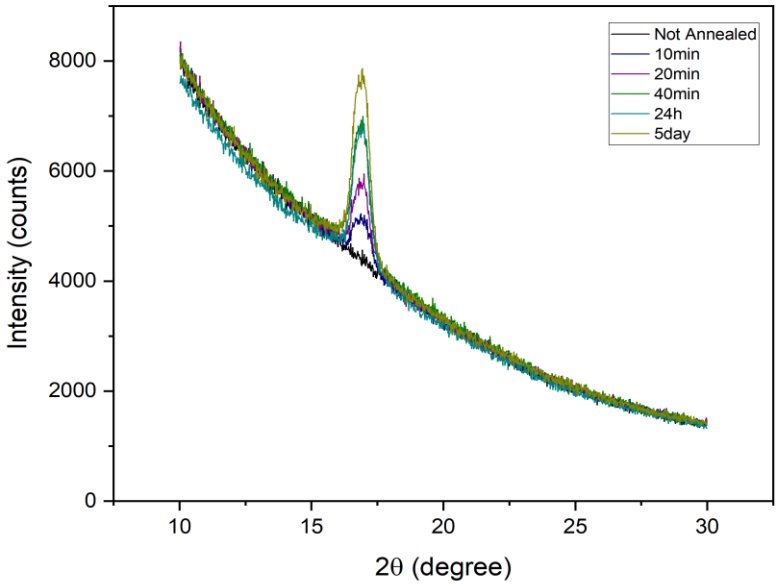


Figure 3.11. The GIXRD plot of a 70nm film annealed at different time periods. The intensity of the peak increased as the annealing time increased to 5 days.

If we use the fraction of crystallinity from the bulk DSC thermogram as a point of reference for the crystallinity in the thin film after 5 days (26%), the degree of crystallization can be determined as a function of annealing time, which is plotted in Figure 3.13 along with the fraction crystallinity of the bulk sample. Furthermore, using the protocol established by equation 3 to determine the fraction of crystallinity in equivalent 60 nm thick coatings of PLGA, the corresponding fractions of crystallinity are also presented in Figure 3.14. The ellipsometry results were in good agreement with the GIXRD results. Crystallization occurred rapidly in the thin films. For example, after annealing at 24 hours, the thin film had developed 24% crystallinity whereas the bulk had only developed 5% crystallinity. Interestingly, despite the different rates of crystallization, the melt temperature of both the film and the bulk sample were highly correlated when plotted as a function of sample crystallinity. The melt temperature was roughly constant at 134 ˚C for up to the 15% crystallinity and then rose to ~140 ˚C between 15 and 25% crystallinity. Finally, the linear thermal expansion coefficient of both the glassy semi-crystalline state (measured below $T_{g,h1}$) and the rubbery semi-crystalline state (measured above $T_{g,h1}$) are provided in Figure 3.16. Here, the thermal expansion coefficient is independent of the fraction of crystallinity in the glassy state but depends linearly on the fraction of crystallinity in the rubbery state, at least up to 25% crystallinity.

The melting endotherm peaks of bulk PLGA grew in intensity and sharpened as the anneal time grew and bulk crystallinity increased (figure 3.12). At 24 hours, melting endotherm I is less pronounced and endotherm II is significantly broad. By day seven, endotherm I and II co-exist and endotherm II narrows. In figure 3.12, there was an observed shift in the positioning of endotherm II with anneal time. The movement of endotherm II correlated to a shift in the bulk

melt temperature of up to 8°C. The narrowing of the endotherm peaks and the increase in melt temperature is due to the higher percentage of crystallization and formation of larger crystals that became present in bulk PLGA.

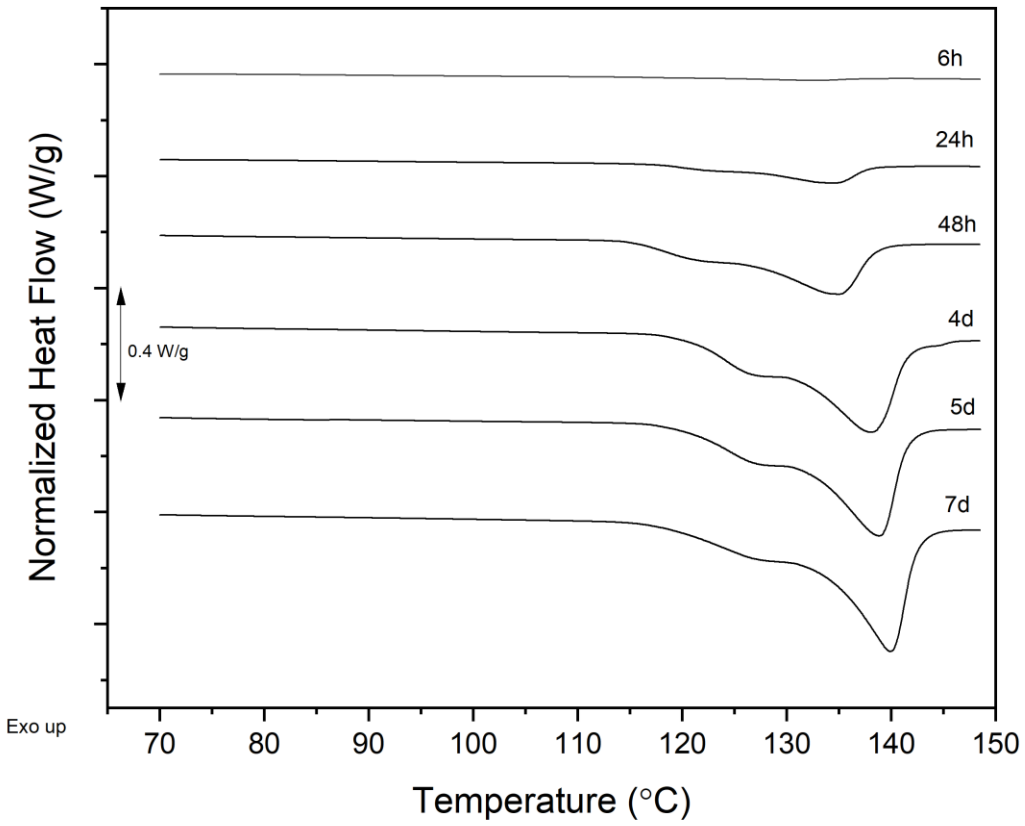


Figure 3.12 The melting endotherms of the annealed bulk PLGA samples

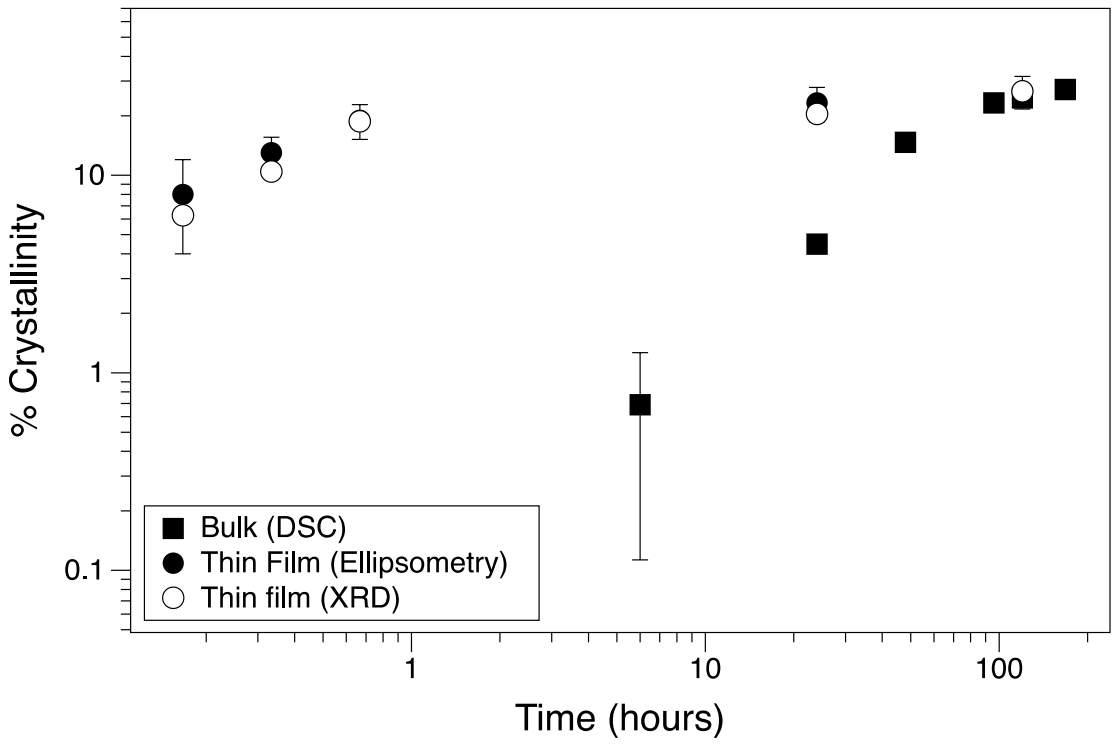


Figure 3.13. The change in crystallinity with increasing anneal time for the bulk and 60nm film.

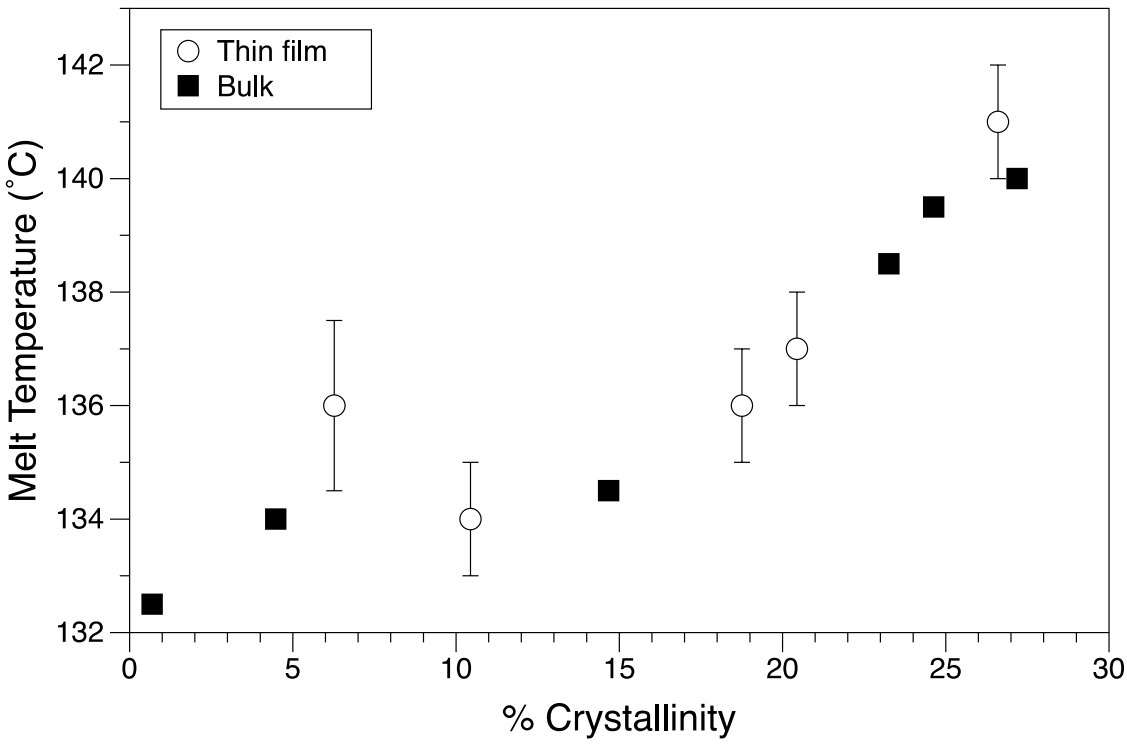


Figure 3.14 The effect of crystallinity on the melt temperature, Tm, for a 60nm film and bulk PLGA

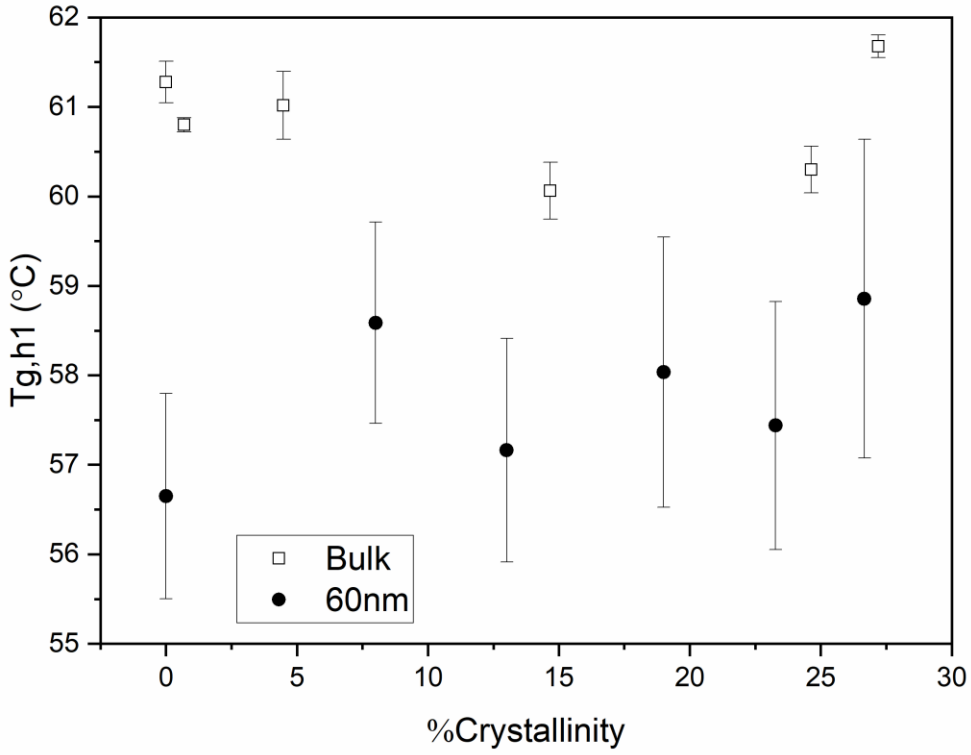


Figure 3.15 The effect of crystallization on Tg,h during run 1

Because both the bulk and thin films were crystallized by isothermal annealing, we would expect to see changes in the glass transition temperature reflected in $T_{g,h1}$ because the samples have not been thermally erased at this point. In figure 3.15, $T_{g,h1}$ for both the bulk and 60nm PLGA films did not significantly change as the result of increases in crystallization. The small increase in the 60nm $T_{g,h1}$ as a result of increases in crystallinity, was considered negligible due to the large deviation in the measurement. Here, it was determined that $T_{g,h1}$ is independent of crystallization.

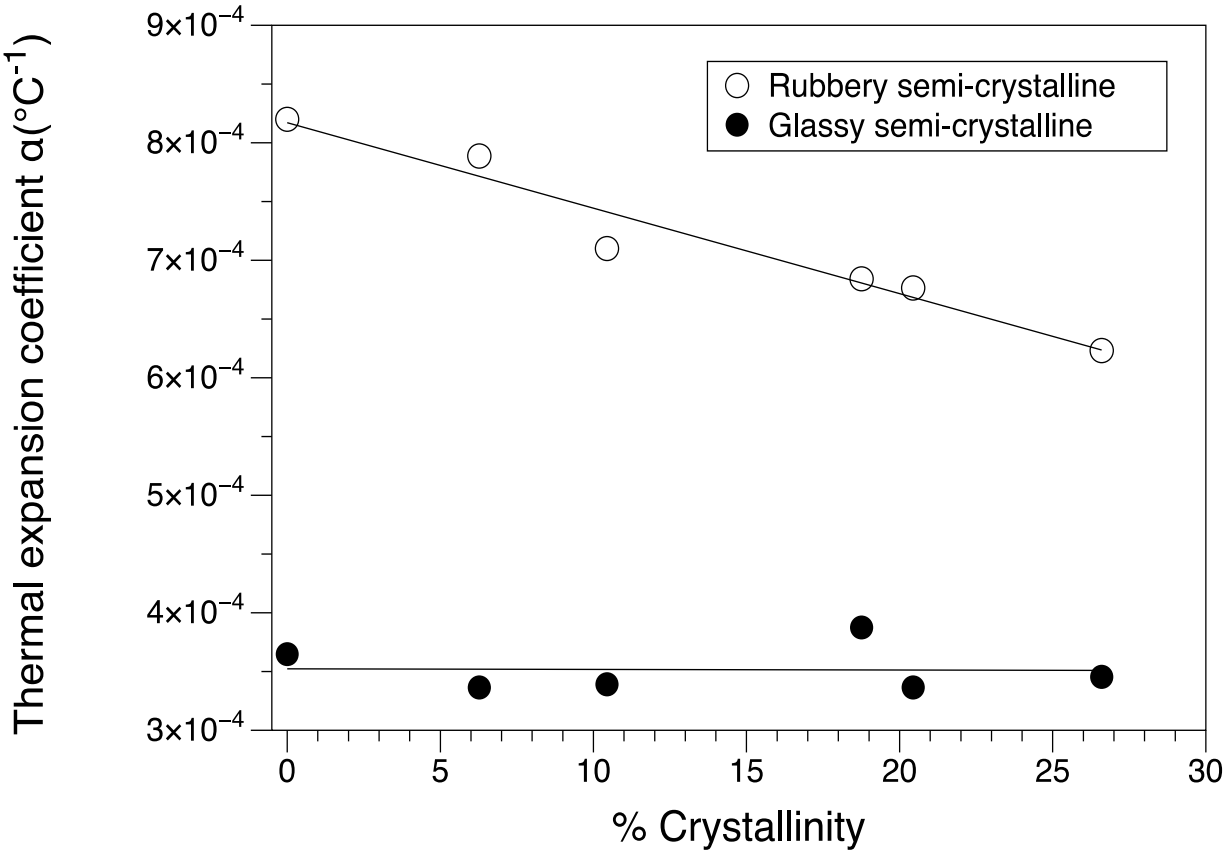


Figure 3.16 Thermal expansion for 60nm films in the glass and rubbery state

To understand the source of the higher value of $T_{g,c2}$ than $T_{g,h2}$ on the second heating/cooling run of the thin film, in which the sample history had been erased [86, 87], figure 3.17 shows AFM height retrace scans of PLGA coatings heated and cooled at a rate of 10˚C/min. Figure 3.17a is a sample that has been annealed at 100 ˚C for 24 hours, showing clear signs of crystallinity. Upon heating, the surface structure is maintained up to 100 ˚C. At 150 ˚C, the surface features are now absent. The appearance of holes in the melting phase of figure 3.17c could be due to changes in the lamellar thickness [63]. Surprisingly, as the film was cooled from 150 ˚C to 30 ˚C at 10 ˚C/s, rod-like crystals formed on the surface. These results indicated that

surface crystallization occurred during the cooling run, but it is insufficient to be readily detected in the subsequent ellipsometry heating run. Surface crystallization may be possible because of the confinement in the film and the increased mobility of the free surface layer [81, 82]. Furthermore, the presence of such surface crystals may frustrate relaxation of the amorphous regions upon vitrification.

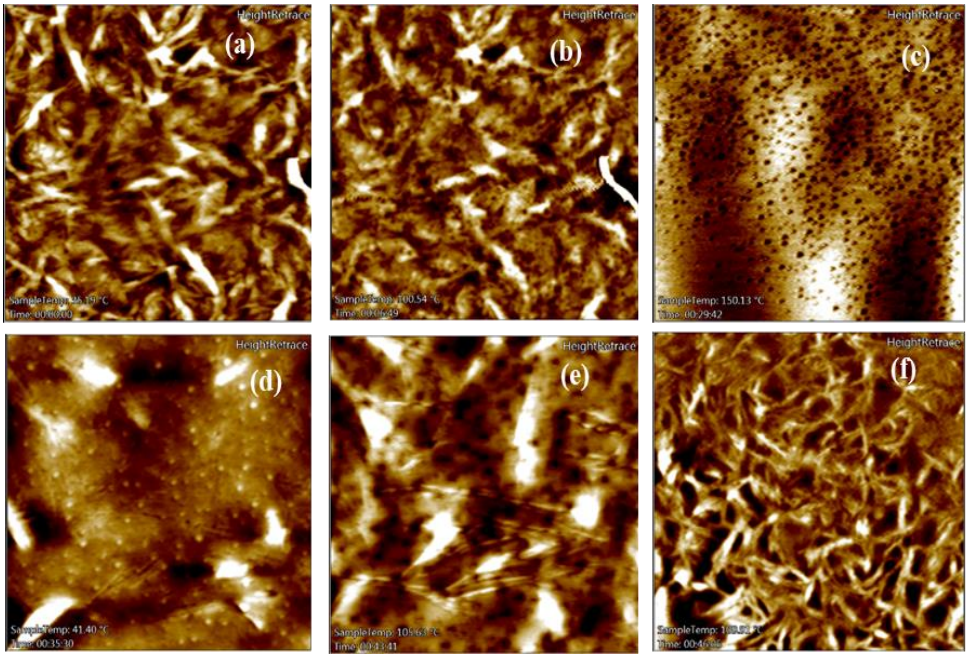


Figure 3.17. AFM images of a 133nm film that went through a heating and cooling scan at 10°C/min (a)film was previously annealed for 24 hours, (b)heating at 100.5°C, (c)heating at 150°C, (d)on the cooling down to 41.4°C (e)heating for a second time at 105.6°C, (f)continued heating at 110°C (images a-c had a scan size of 1µm, image d and e had a scan size of 500nm and image f had a scan size of 2µm).

### 3.3.3 Thickness Dependency in Thin Films

For films with no sample history and thicknesses greater than 50nm, both $T_{g,h2}$ and $T_{g,c2}$ became fairly stable with $T_{g,h2}$ at 55°C +/- 2°C and Tg,c2 at 58°C +/-2°C, where $T_{g,c2}$ was higher than $T_{g,h2}$ (figure 3.18). The result of $T_{g,c2}$ being greater than $T_{g,h2}$ is consistent with other studies and can be attributed to the ability of the film to fully relax while experiencing confinement of the molecular chain groups [68, 72, 77, 94-97]. Interestingly, when the film thickness is less than 50nm, $T_{g,c2}$ sharply decreased and $T_{g,h2}$ increased, making $T_{g,c2}$ less than $T_{g,h2}$. There is also the effect of the silicon substrate on the film. $T_g$ of supported films have been reported higher than $T_g$ of free standing films, this indicates that the increase of substrate polymer interactions and the presence of a free surface causes shifts in $T_g$ [98-101]. Additionally, $T_{g,c2}$ in thin films was comparable to the bulk $T_{g,c2}$. These results demonstrate that the heating and cooling glass transition temperatures are independent of thickness above 50nm.

In the glass regime, the thermal expansion coefficient did not show any sensitivity to increases in the degree of crystallization. However, when the sample history was erased, the thermal expansion coefficients in both the cooling and heating runs were more sensitive to changes in film thickness. In figure 3.19, the thermal expansion coefficient decreased by half (or a factor of 2) between 55 and 124nm in the glass regime. Likewise, the same phenomenon was observed in the melt regime, where the thermal expansion coefficient decreased by half due to increasing thickness (figure 3.20). These results demonstrate that the thermal expansion coefficients have a strong sensitivity and dependency on thickness. Additionally, the decrease in thermal expansion coefficient occurred during both the heating and cooling runs. This indicates that the reduction of the thermal expansion coefficient was more attributed to thickness than due

to the effects of the heating and cooling run in thermally erased films. The increase in the thermal expansion coefficient with decreasing thickness could be due to greater confinement of the molecular chain groups, and the role of substrate binding and mobility in thinner films.

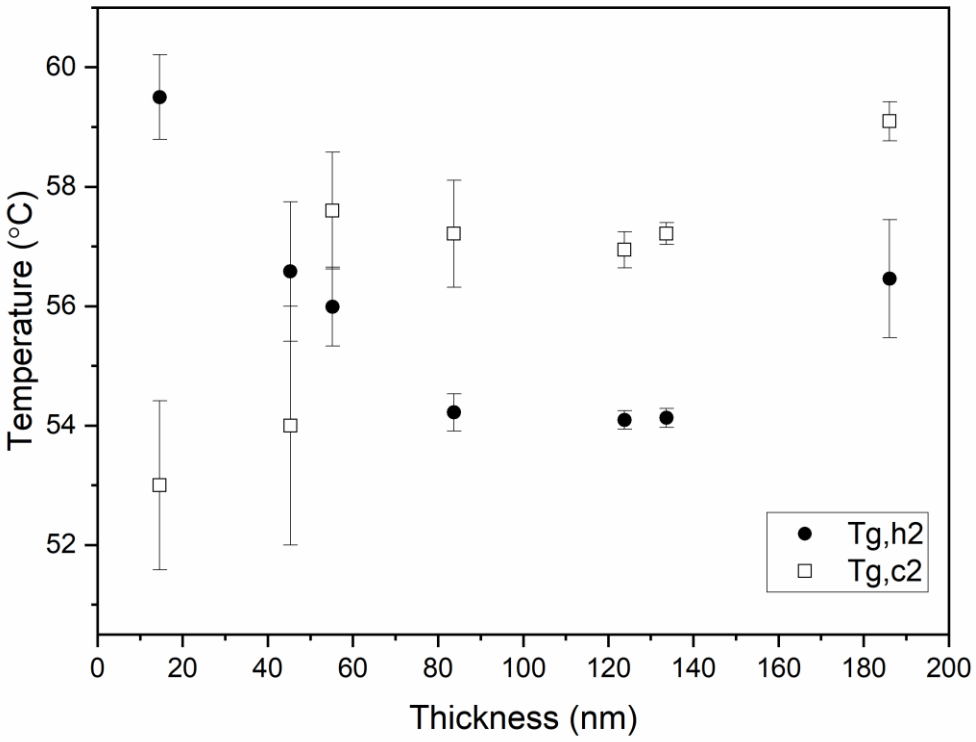


Figure 3.18 The changes in glass transition temperature during heating and cooling for films with no sample history (Tg,h2 and Tg,c2)

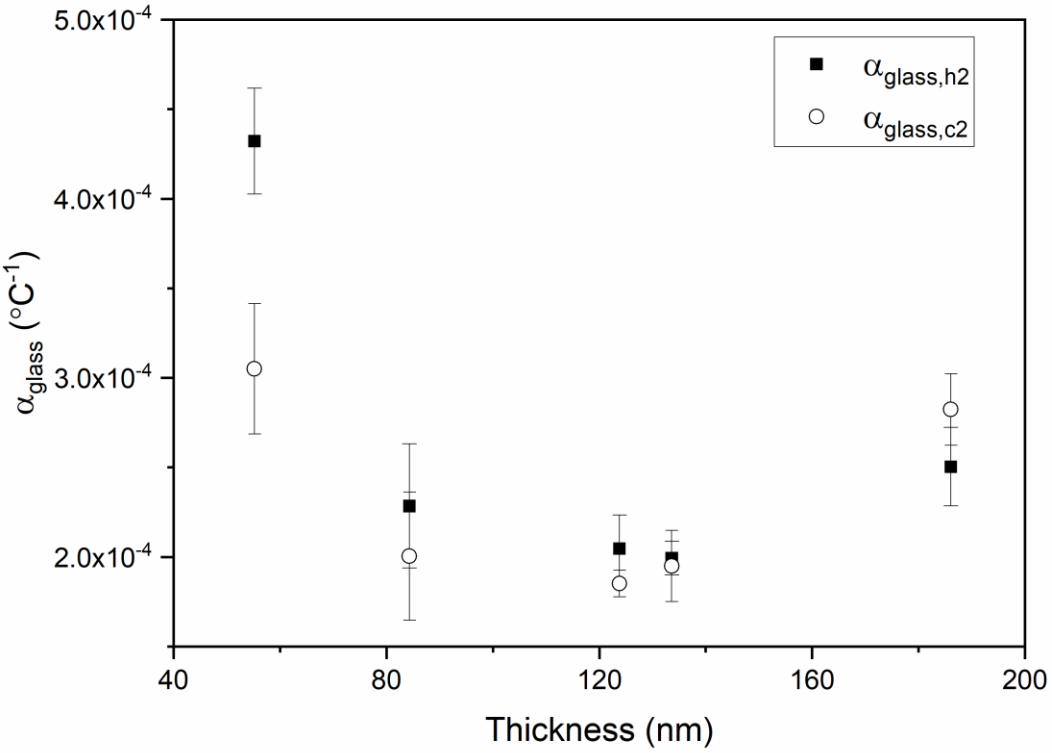


Figure 3.19 The reduction of the thermal expansion coefficient due to increasing thickness in the glass regime for films with no sample history

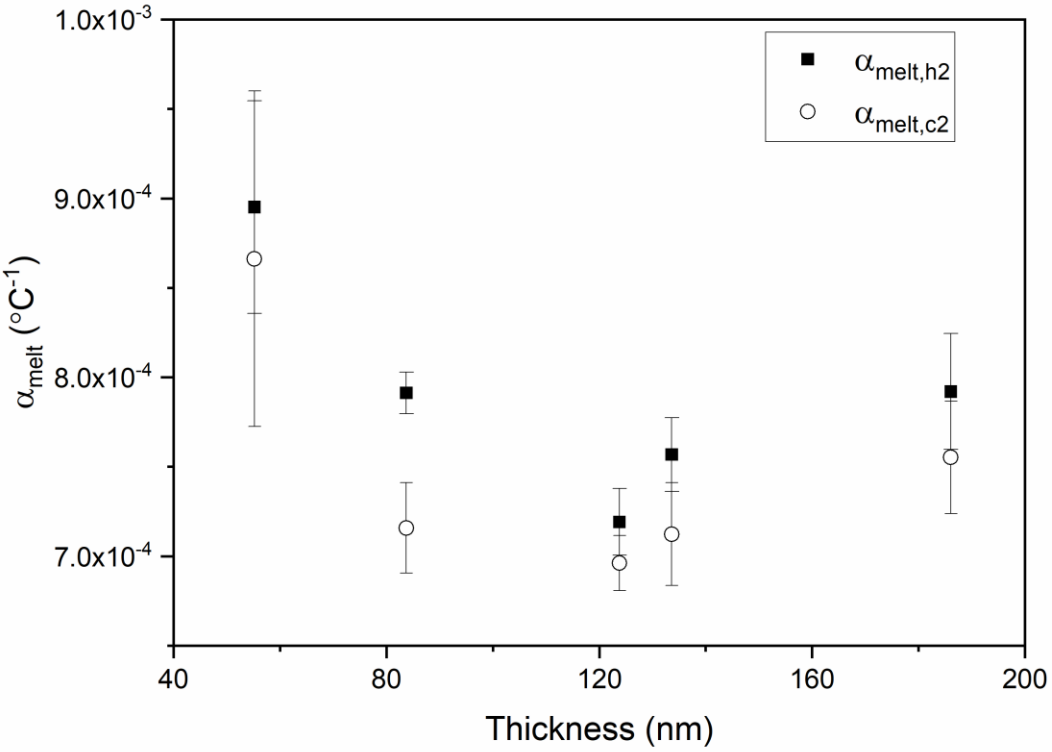


Figure 3.20 The reduction of the thermal expansion coefficient due to increasing thickness in the melt regime for films with no sample history

### 3.3.4 Relaxation Behavior During Heating and Cooling

Interestingly, during the course of heating and cooling the samples, at times the cooling run would be above the heating run, the cooling and heating runs would cross, or the cooling and heating runs would come close to overlapping. In figure 3.21, a 185nm film had a final thickness greater than the starting thickness and the cooling run was above the heating run. For a film of a similar thickness, the cooling run crossed the heating run at about 80°C and the final thickness was greater than the starting thickness (figure 3.22). In a different case, the cooling run remained above the heating run, but at the end of the run, the heating and cooling runs nearly overlapped (figure 3.23). In all three of these cases, the cooling run remained consistently greater than the heating run, immediately after the film transitioned from heating at a temperature beyond the melt temperature. The glass transition on cooling remained fairly constant regardless if the cooling run crossed, overlapped or was higher. In order to understand this phenomenon, films that were not annealed underwent a heating cycle where their sample history was erased at 150°C using the ellipsometry heating cycle. After the sample history was erased, the films were cooled to 100°C and were annealed for sixteen hours at 100°C on the ellipsometry heating stage. The changes in thickness were measured periodically over the course of sixteen hours.

Figure 3.24 provides an overview of the ellipsometry heating and cooling scan during the annealing time hold. After the sample was held at 100°C for sixteen hours, there was a clear reduction in the thickness and the cooling run dropped below the heating run and overlapped the heating run at the end of run 1 (figure 3.25). Moreover, when the sample was reheated for a second heating cycle, there was evidence of a melt temperature, indicating that the film crystallized during the sixteen-hour period (figure 3.26). The difference between the glass

transition temperatures on heating and cooling during run 2 and run 1 was, $T_{g,h2} - T_{g,h1} = 2°C$. However, given the standard deviation of +/- 1°C, it was concluded that the $Tg_{,h1}$ and $T_{g,h2}$ remained fairly constant across the runs, which was consistent with the results discussed earlier that demonstrated that the glass transition temperature is independent of crystallization. The onset melt temperature was 120°C, which is similar to the melt temperature of endotherm I in the bulk. This finding would suggest that there was a presence of smaller crystals in the thin film. The cooling run remained above the heating run during run 2, even though the cooling run almost overlapped with the heating run at the end.

The results of annealing the films for sixteen hours, revealed that there is an interesting relaxation behavior occurring in the thin films, which occurs after the films past the melting regime and enter cooling. During this transitive phase, the films are forced into a relaxation mode. It is important to highlight the importance of the substrate during the relaxation process. There may be additional stress and strain between the mismatch between the substrate and the film, which is enhanced during high heating and immediately with cooling, which could be attributing to the switching behavior of the cooling runs. Furthermore, there is also the role of the degree of mobility at the substrate and film interface and the film and air interface that interplay with the molecular chain confinement. Additionally, the previous afm results demonstrated that there is a thin crystallizable layer that forms on the surface of the film during cooling. The presence of the thin crystallized layer is another factor that contributes to the switching behavior of the cooling runs.

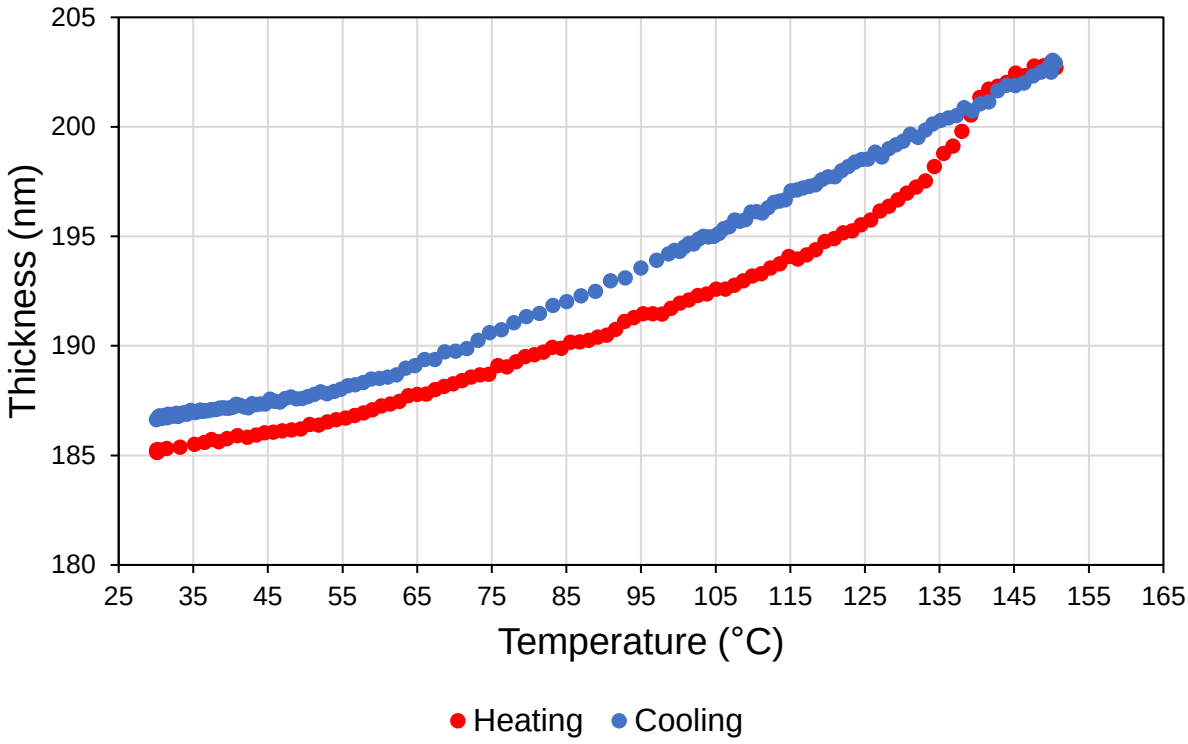


Figure 3.21 Heating and cooling scan during run 1 for a film that was annealed for 24 hours, where the cooling run was above the heating run

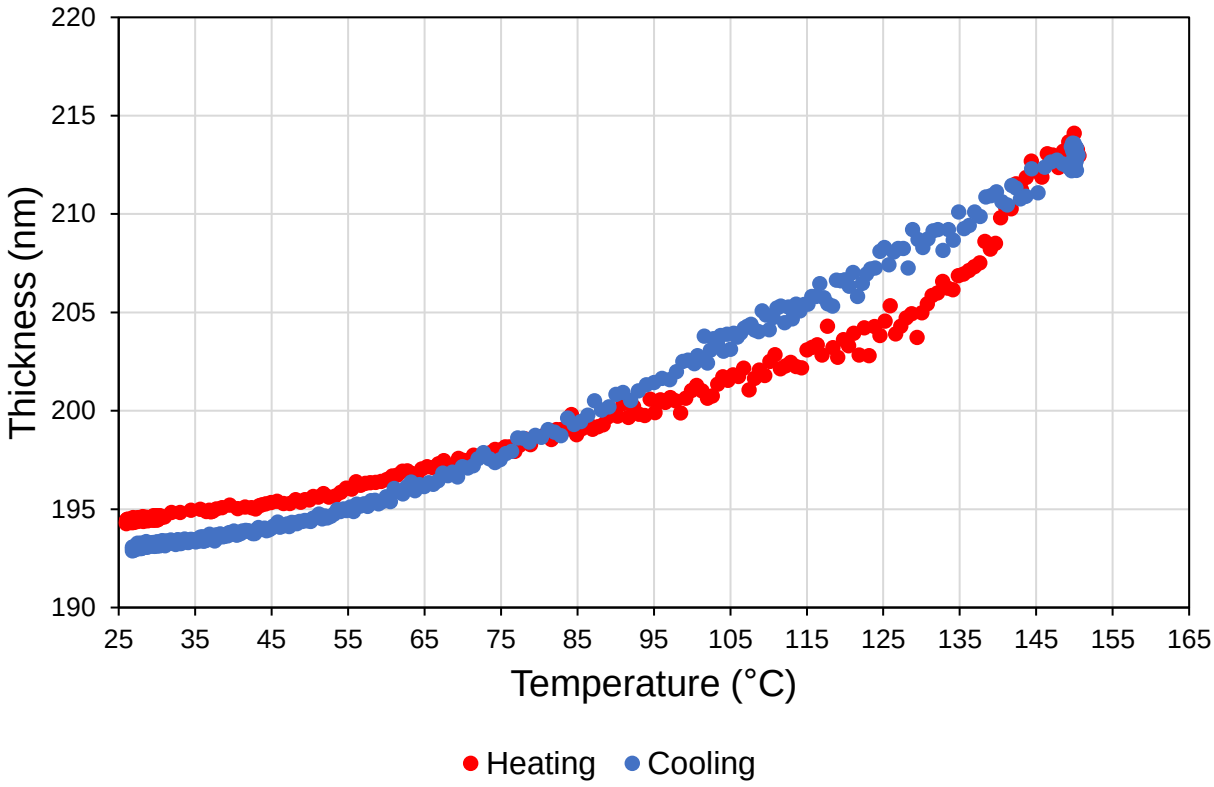


Figure 3.22 Heating and cooling scan during run 1 for a film annealed for 5 days, where the cooling run crossed the heating run

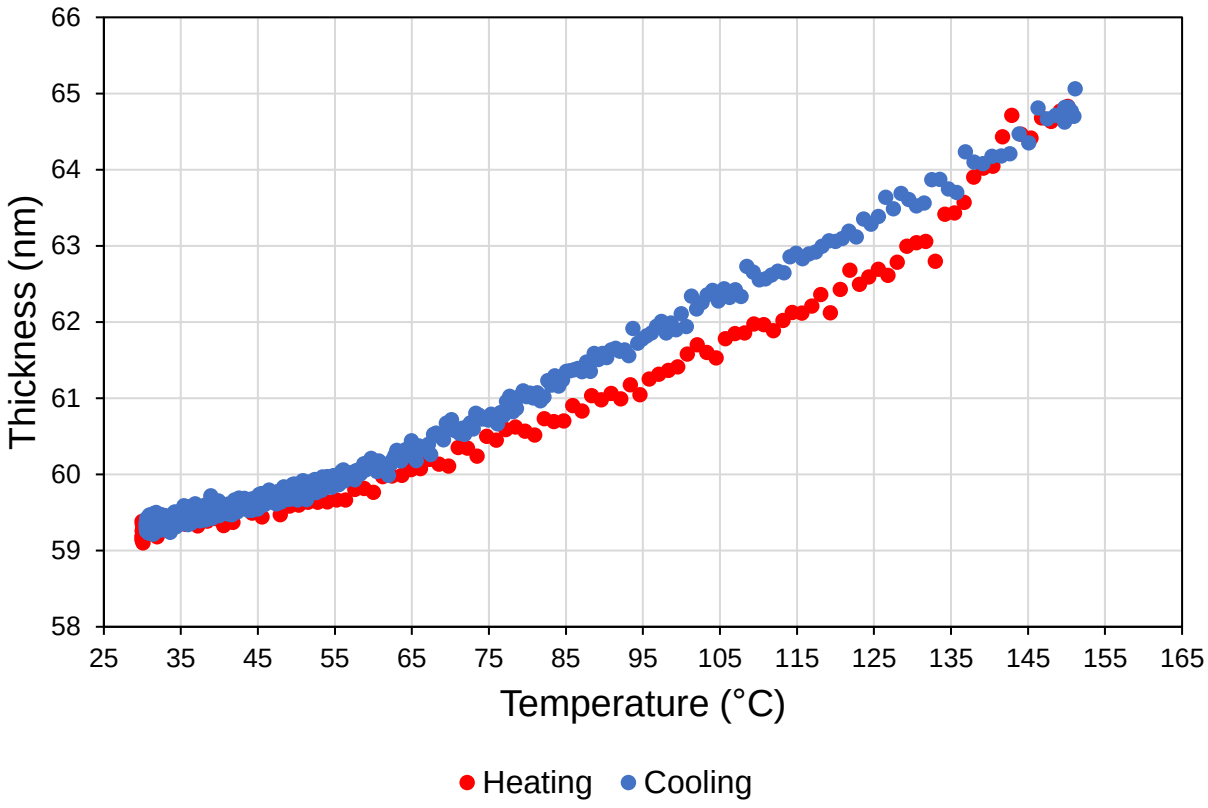


Figure 3.23 Heating and cooling scans during run 1 of a 24h annealed sample, where the heating and cooling runs almost overlap at the end of the run

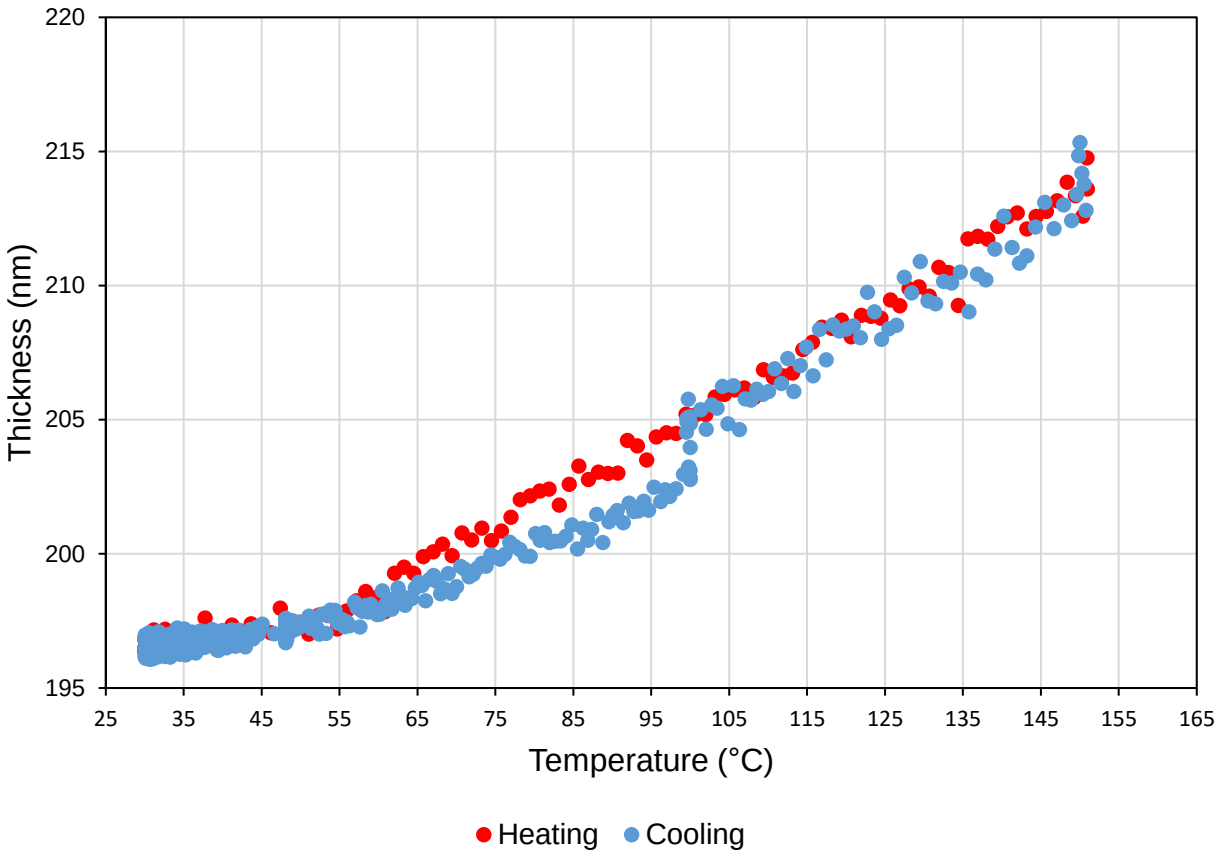


Figure 3.24 The heating and cooling cycle of an un-annealed 200nm sample that was held at 100°C during the cooling run during run 1

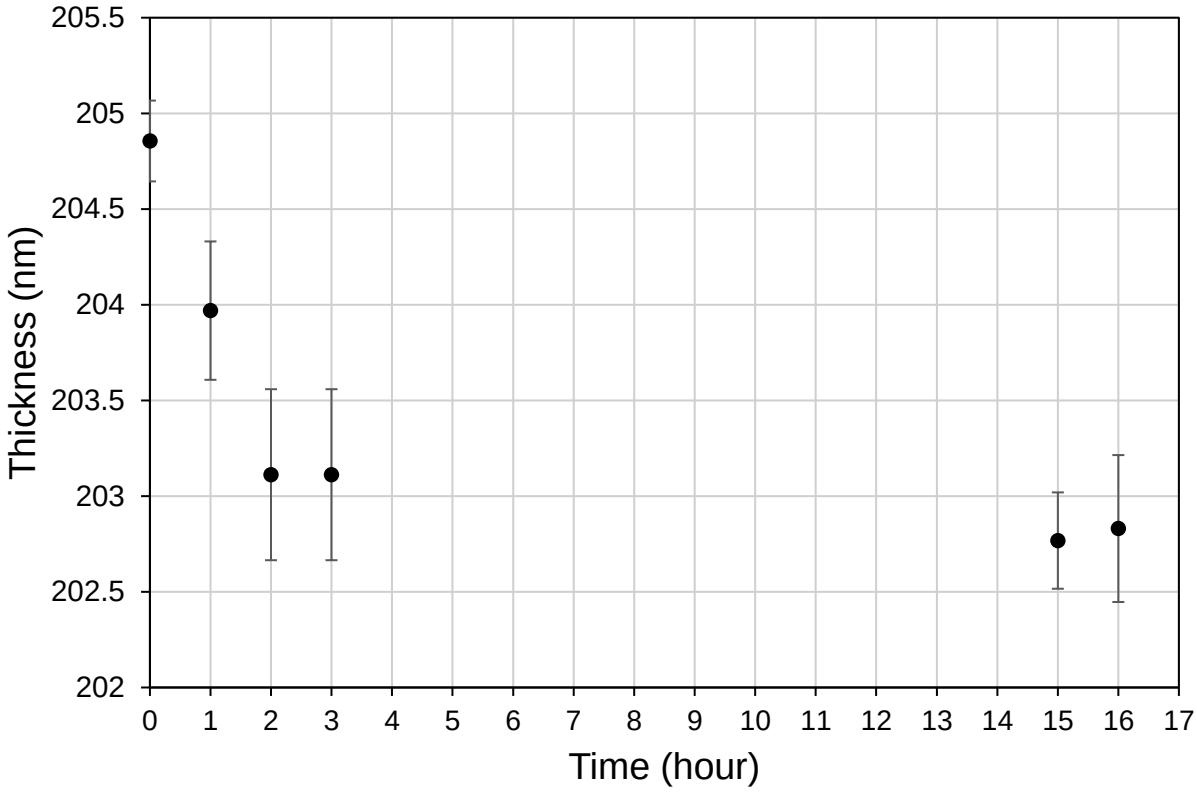


Figure 3.25 The film thickness decreased during 16 hours of crystallization held during the cooling run of run 1

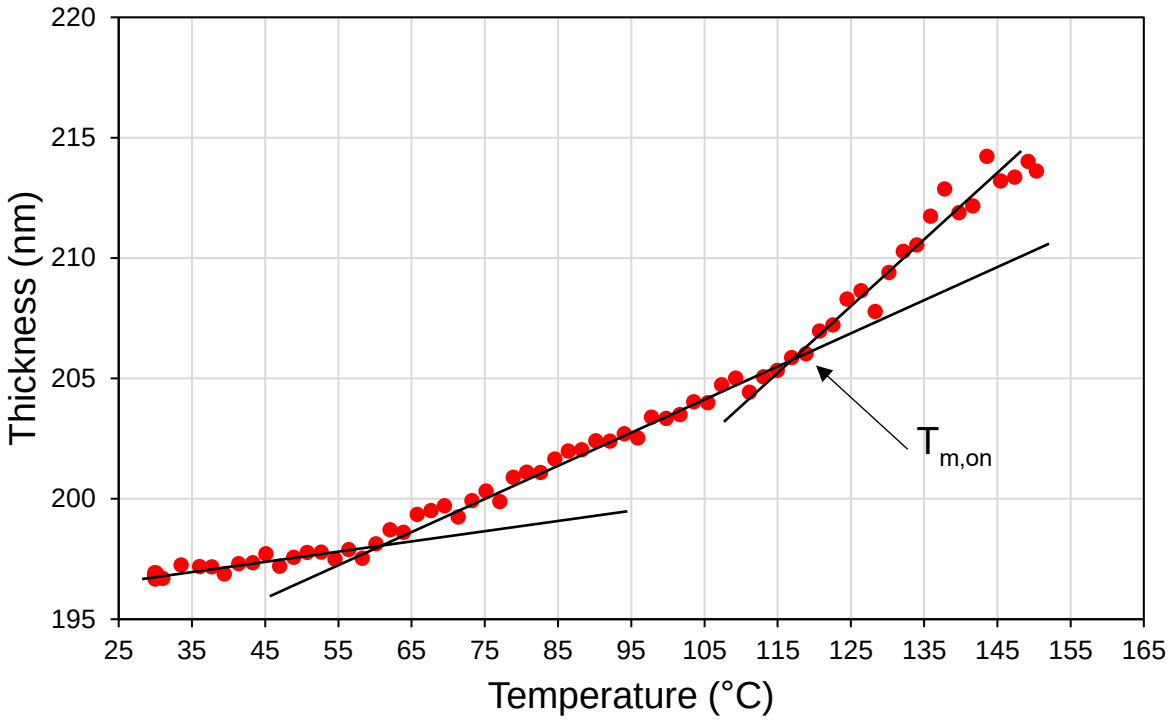


Figure 3.26 The heating curve of run 2 after the film was annealed for 16 hours.
Tm,on is the onset of melting

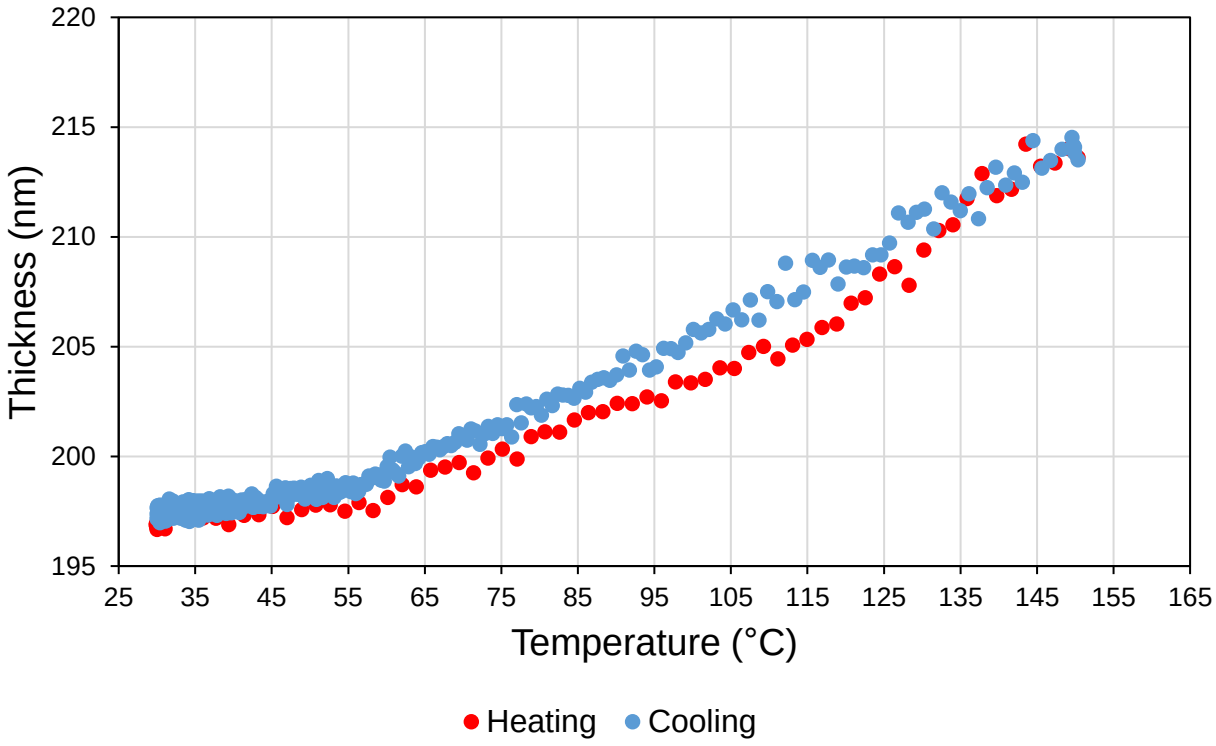


Figure 3.27 The heating and cooling cycle of run 2 after the film was crystallized for 16h on the ellipsometer heating stage

### 3.4 Conclusion

Crystallization behavior in thin PLGA films ranging between 50 and 200nm was investigated by ellipsometry and compared to the bulk. The melt temperatures for the thin film and bulk were comparable and increased with greater degree of crystallization; although crystallization occurred faster in the thin film than the bulk. Interestingly, the ellipsometry results coupled together with the AFM images revealed that during cooling surface crystallization occurred on the film and may be associated with a relaxation behavior that is preventing the film to fully contract and expand. The thermal expansion coefficient for an amorphous film in the rubbery state decreased as the film became more crystalline. The thermal expansion coefficient was also dependent on thickness for films between 50 and 124nm. The glass transition temperatures were found to independent of thickness for films greater than 50nm. More work should be done to determine how surface crystallization on cooling tunes the glass transition temperature and its relaxation behavior in ultrathin films.

# Chapter 4: Surface Degradation of Crystallized Thin PLGA Films

## 4.1 Introduction

Metal and metal alloys commonly serve as materials for orthopedic implants. However, one of the main disadvantages of metals is that when exposed to water, hydrolysis and breakdown of materials occurs. Polymer thin films have the potential to act as surface barriers to aid in reducing the rate of degradation of the metal alloys. More specifically, polylactic acid and poly(lactic-co-glycolic acid), PLGA, are biodegradable and biocompatible polymers approved by FDA and can be used in several biomedical applications [102-104] Degradation in PLGA is known to occur by breaking of the ester backbone due to chain scission. The by-products of hydrolytic chain scission are water soluble, biodegradable products that are absorbed by the body [105-109]. The rate of diffusion of water into the film is a determinant in deciding whether degradation is happening through the bulk of the film or if erosion is happening at the surface. Surface erosion is generally characterized by a mismatch between water diffusion and hydrolysis and can be limited to the amount of chain ends available to catalyze hydrolysis. In the case of surface erosion, water diffusion will become slower than the rate of hydrolysis [110, 111]. There are several factors that can affect the degradation rate of PLGA. Korber highlights that oligomer solubility limited diffusion of PLGA should be considered in evaluating the erosion behavior of PLGA [112]. Molecular weight, porosity, pH, and crystallization are known to affect the degradation rate of polymers [113-119].

Currently the literature has focused on evaluating degradation as a function of molecular weight, copolymer ratios in bulk or in scaffolds. However, more work is needed to understand the nature of degradation relative to the thickness of ultrathin films. Here, it is hypothesize that crystallization will slow the degradation rate. The purpose of this present work is to investigate the role of crystallization in tuning the degradation rate of ultrathin PLGA films.

## 4.2 Materials and Methods

### 4.2.1 Thin Film Preparation

Silicon wafers were plasma etched and silanated with 4% (3-Aminopropyl)triethoxysilane (ATPES) in acetone to promote better adhesion of the films to the substrate (figure 4.1). Poly(D,L-co-glycolic acid) (85L/5D/10G), PLGA, was obtained from ConMed Corporation. PLGA was dissolved in chloroform to form a polymer solution and then spin coated on the silanated wafers for three minutes at a spin speed of 3000 rpm. Afterwards, films were either thermally erased at 150°C to erase sample history or isothermally annealed at 100°C for five days to achieve maximum crystallinity.

Simulated body fluid (SBF) was prepared following the recipe of Bayraktar and Tas at a pH of 7.4 [120]. Films were disinfected with a bleach solution, rinsed in distilled water and placed in SBF at 37°C. Films were removed from SBF weekly, cleaned with a bleach solution and distilled water, and then vacuum dried for two hours to obtain the dry thickness.

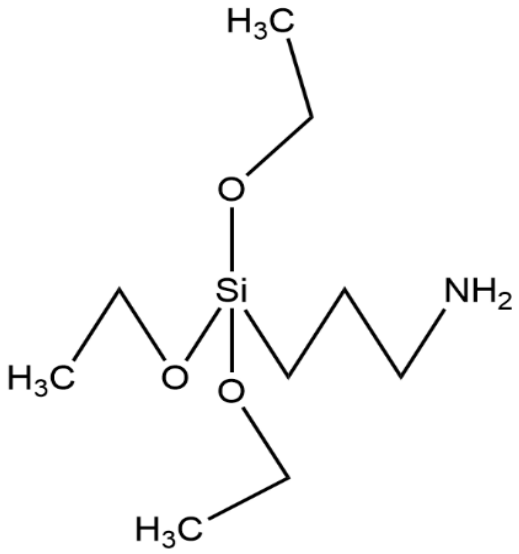


(3-Aminopropyl)triethoxysilane

Figure 4.1 The structure of (3-Aminopropyl)triethoxysilane, APTES

4.2.2 Ellipsometry

A home-built variable-angle rotating compensator ellipsometer was used at a fixed angle of incidence. The ellipsometer used a He-Ne laser light source with a wavelength of 633nm. The thickness of the films were normalized to the initial start thickness.

$$d_{norm} = d_t/d_0 \qquad (5.1)$$

where $d_t$ is the thickness at a specific time period and $d_0$ is the initial film thickness before exposure to SBF. The same normalization procedure was repeated for the refracted index.

$$RI_{norm} = RI_t/RI_0 \quad (5.2)$$

where $RI_t$ is the refractive index at time, t and $RI_0$ is the initial refracted index of the film prior to subjection to degradation in SBF.

### 4.2.3 Statistical Testing

A one-way ANOVA test using a Bonferroni test was used to evaluate the statistical significance of the results. A one-way ANOVA test was chosen because there was only one independent variable considered for this experiment. A Bonferroni correction was used to reduce the risk of a type I error. Here, significance was determined by $p<0.05$. Sample sizes were n=3.

### 4.2.4 Atomic Force Microscopy (AFM)

A Digital Instruments atomic force microscope was used to investigate the surface topography of vacuum dried 70nm and 200nm films. Measurements were made using the tapping mode configuration. Samples were dried in a vacuum oven prior to AFM imaging.

## 4.3 Results and Discussion

### 4.3.1 Thickness Dependent Degradation

70nm and 200nm PLGA films were fully immersed in SBF and incubated at body temperature, 37°C, to investigate degradation behavior in a simulated body environment. There

are two types of methods to model the internal body environment, static and dynamic. The results of this study were done using the static method. Here, the fluid was not constantly moving at specified rate similar to the fluid dynamic behavior of the human body. Over a six week period, there was a strong reduction in the thickness of 200nm thermally erased films (figure 4.2). In contrast, the thickness of the fully crystalline 200nm films remained fairly constant when exposed to SBF during the same time period. There was no statistical difference between the start and end thickness of the fully crystalline films, while, there was a statistical difference between the initial and final thickness of the thermally erased films at six weeks. 200nm thermally erased films eroded three times faster than 200nm crystallized films. The observed linear reductions in the PLGA film thickness over a six week period, indicative of surface erosion, shared similarities with other findings of linear reductions in the molecular weight of PLGA films [121].

The erosion rate for 200nm thermally erased films was -0.0064 normalized units/week versus -0.0028 normalized units/week for crystalline films. The rapid erosion rate can also be associated with the static environment of the films. In the static environment, there is the absence of fluid flowing constantly in one direction, and as a result degradation is happening across the surface of the film, as the film homogeneously absorbs SBF, and as a result autocatalytic degradation can occur. SBF was replaced on a weekly basis to help minimize the effects of acidic by-products that can arise in the absence of dynamic flow. Some contributions of an acidic environment could have caused the rapid degradation rates [122-125]. Huang et. al, demonstrated that for PLGA (50:50) films, degradation rates were higher in static environments rather than in dynamic flow [123].

Secondly, the rapid erosion rate of the thermally erased films can be attributed to its amorphous, highly mobile structure [107, 126]. The dense packing of the crystalline network of the fully crystalline films helps to close and seal pores to prevent water from entering. The lack of a crystalline network leaves the amorphous region exposed and open to water. Additionally, the thermally erased films are spin coated with a polymer chain entanglement configuration formed from spin casting and then thermally erased above the melt temperature for two minutes and immediately removed from the oven, immediately quenching the film.

The PLGA film used in this study consisted of 10% glycolic acid. The lower percentage of glycolic acid used in this film may have attributed to the slower degradation rate, because there is greater hydrophobicity associated with 85% lactic acid. Vey et al. observed that slower degradation rates were associated with PLGA films that contained higher lactic acid units; for example PLGA 50/50 loss six times more mass than PLGA 95/5 within 10 days during in *vitro* degradation in phosphate buffer solution [127]. Studies that evaluated the involvement of glycolic acid in the degradation rate discovered that slower degradation rates were accredited to lower percentages of glycolic acid in the polymer [128, 129].

Compared to the 200nm thermally erased films, the 70nm thermally erased films eroded three times faster than the 200nm films. The erosion rate for the 70nm thermally erased films was -0.018 normalized units/week. Interestingly, the erosion rate also corresponded to the relationship between the thicknesses. The 200nm films were three times thicker than the 70nm films and consequentially, eroded three times slower. It is possible, that the erosion rate

corresponds linearly or is proportional to the reduction of initial film thickness. The contrast in the erosion rates, indicate that crystallization can slow down the erosion rate of thin films. After six weeks, the films began to delaminate from the silicon substrate. Future degradation studies of PLGA thin films should include better adhesion of the films to the substrate to allow for longer study time periods.

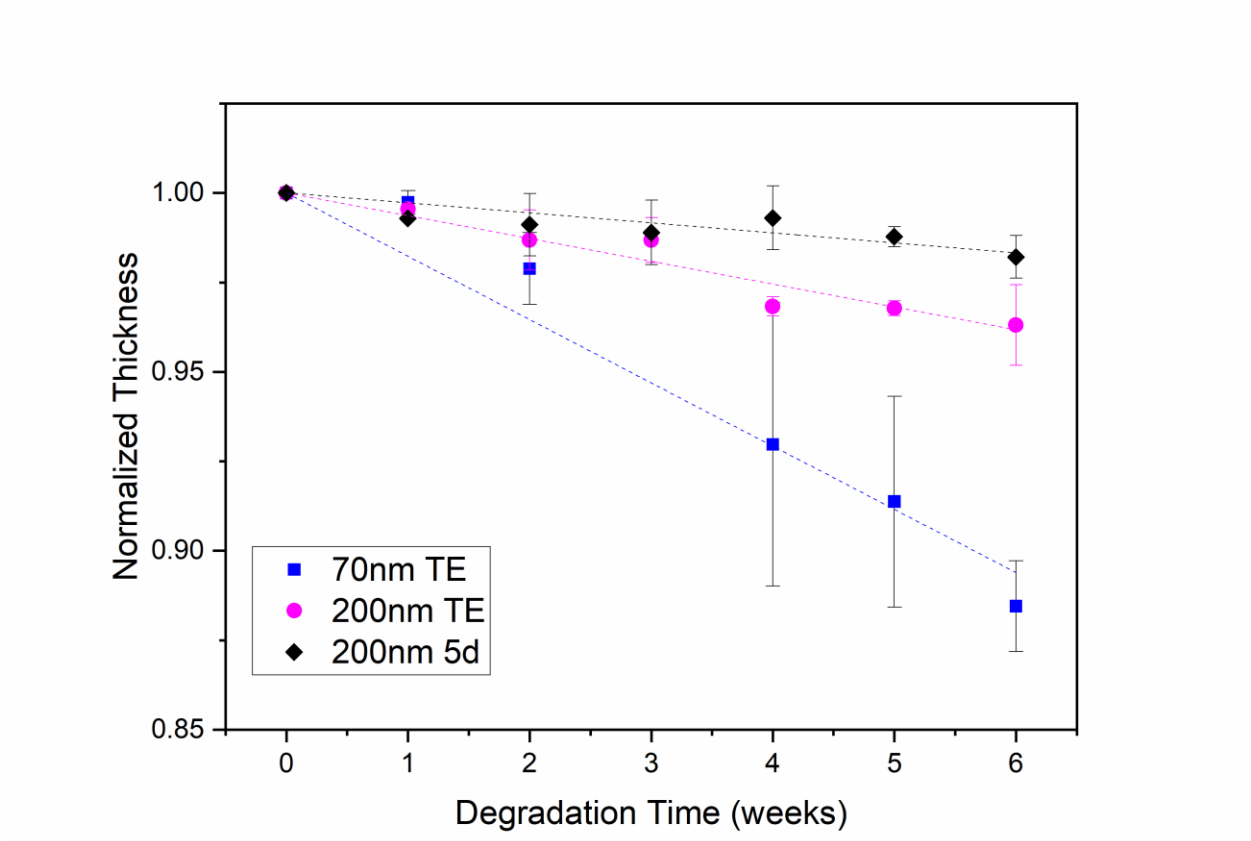


Figure 4.2 The reduction of film thickness in SBF over six weeks. 70nm thermally erased films eroded the fastest, where 200nm fully crystalline (5d) films eroded the slowest.

### 4.3.2 Refractive Index Behavior

Although, there was significant thickness reduction for the thermally erased films, the refractive index remained constant for both the thermally erased and crystalline films (figure 4.3). There was no statistical significance between the refractive indices at the beginning and the end of the degradation experiment. Thus, indicating that surface erosion occurred. In the case for bulk degradation, it would be expected that the refractive index would decrease with decreasing thickness.

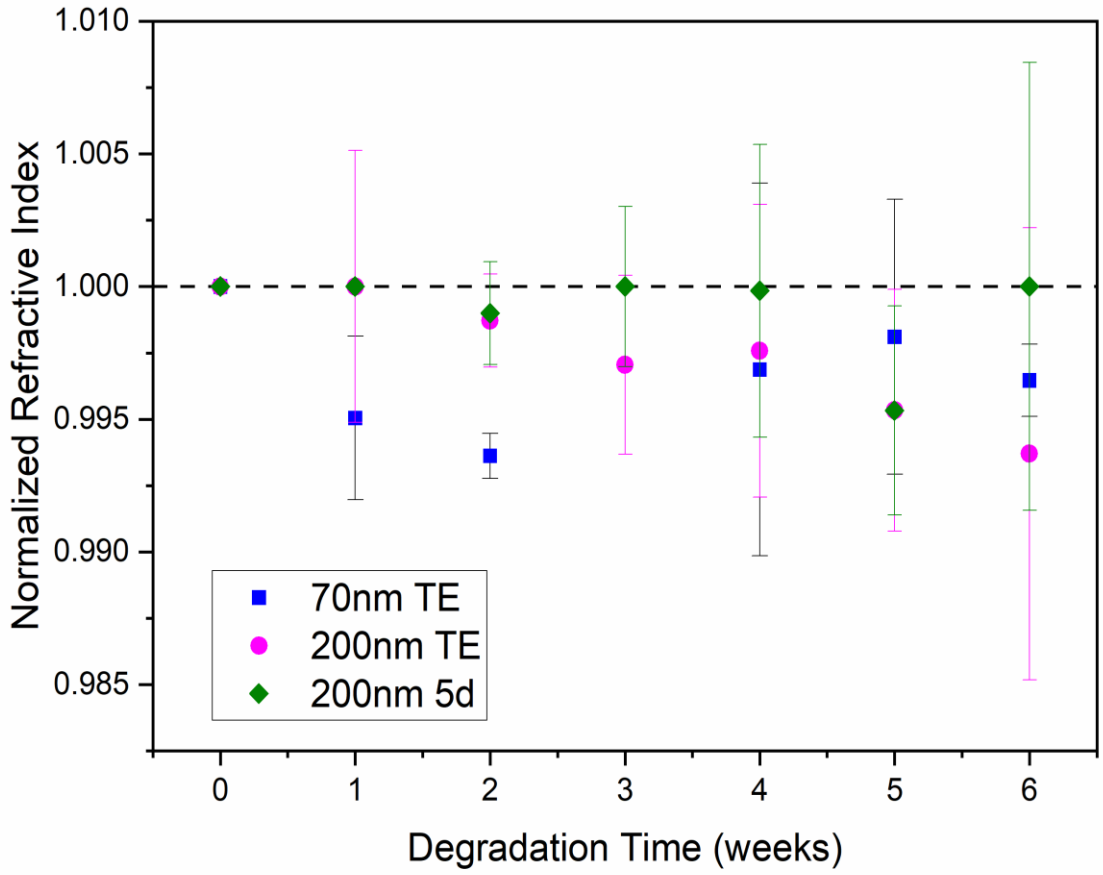


Figure 4.3 There was no statistically significant change of the refractive index for the 70nm and 200nm thermally erased and crystallized PLGA during the six week degradation period

Moreover, the AFM images revealed that there were slight changes to the surface of the 200nm thermally erased film at week five (figure 4.4). The afm images reveal that there was dense packing of the fully crystalline film, which would have helped to reduce the diffusion of water into the film. At week zero and week five there were no changes in the morphology of the crystalline film. The afm images support the conclusion that surface erosion occurred on the films and not degradation through the whole film. Although there were perturbations on the surface of the week five thermally erased films, these perturbations did not cause a strong

increase in the surface roughness. The perturbations on the thermally erased surface could be early indications of surface erosion. Because the amorphous structure was more exposed to water in thermally erased films, it is possible that the glycolic acid units broke down faster, yielding a slightly more acidic environment. The perturbations on the thermally erased film could be due to erosion from an acidic environment, hence if the films were degraded longer in SBF, it would be expected that the surface roughness would dramatically increase.

### 4.4 Conclusion

Surface erosion of the thermally erased films indicated that crystallization can slow down the thin film erosion time. More importantly, this indicates that the crystallized thin films may act as protective layer or barrier to erosion of resorbable implants in body fluid. To expand our understanding of the degradation behavior, longer period of evaluation is necessary.

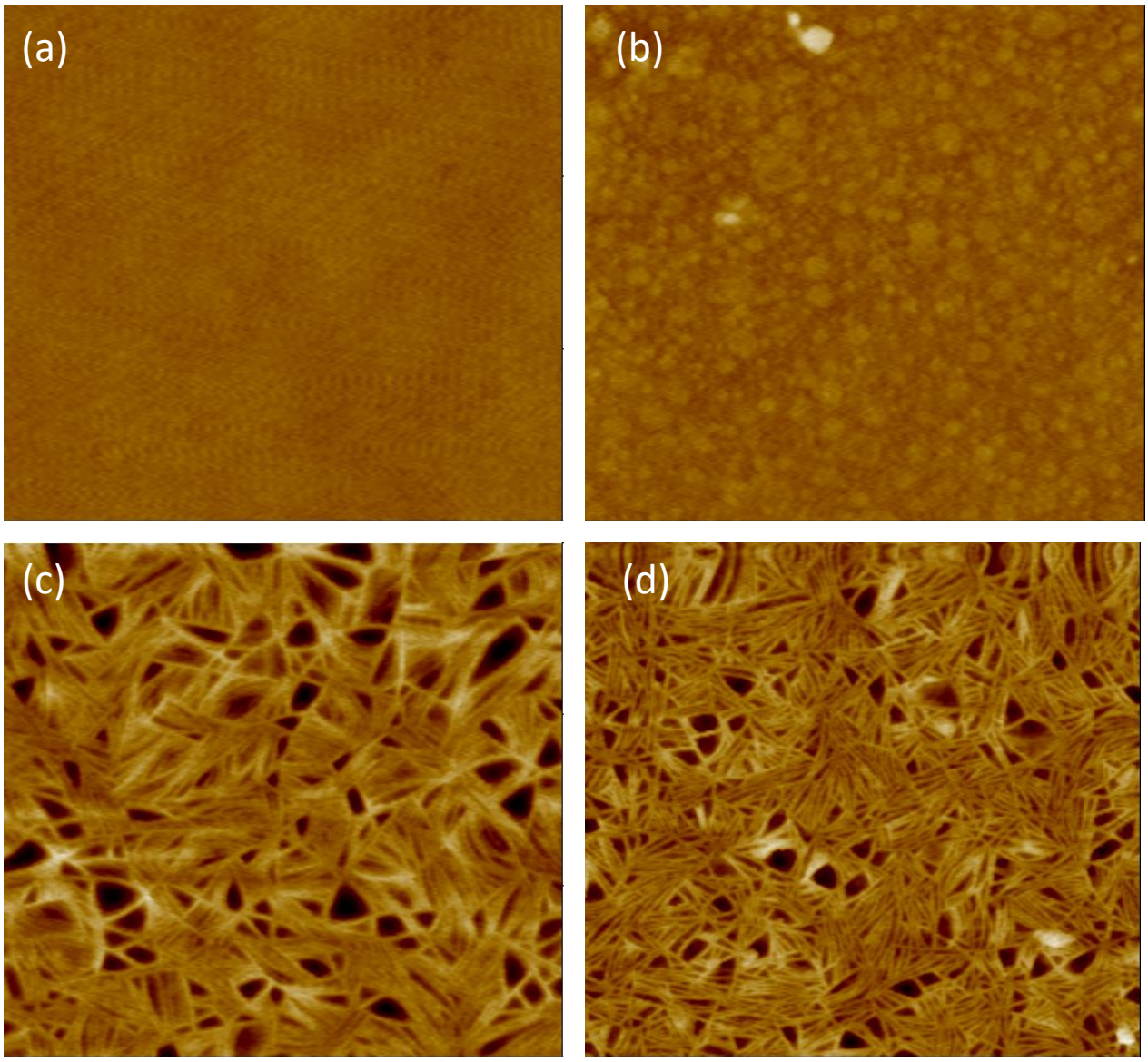


Figure 4.4 Surface morphology changes of 200nm PLGA film eroded in SBF over five weeks. There were slight changes to the surface of the TE films but no visible changes on the 5d annealed films. All images were taken at a scan size of 3μm. (a)TE at 0 weeks, (b)TE at 5 weeks, (c)5d at 0 weeks, (d)5d at 5 weeks. (*TE: thermally erased and 5d: 5 day annealed film, fully crystalline)

# Chapter 5: Adhesion Strength of Osteoblast Cells on Crystallized Thin Films

## 5.1 Introduction

Adhesion and anchorage of osteoblast cells to bone injury sites is of great importance in the field of orthopedics. Majority of orthopedic implants are made out of either metal alloys or biodegradable polymers. Several studies have been done to evaluate the adhesion of osteoblasts in scaffolds and metallic materials. More recently, studies have begun in characterizing osteoblast adhesion and osteoconductivity on polymeric materials. There are several factors that can affect the adhesion strength of cells on surfaces, such as surface roughness, integrin binding, surface chemistry, and material composition. There are three stages of cell adhesion in static environments: sedimentation, attachment and spreading. In stage I, there is initial attachment of the cells to the surface of the film via electrostatic interaction. In stage II, the cells flatten and spread on the surface and initiate binding of receptor-ligand pairs. During stage II, there is also initial formation of the microfilament bundles. In stage III, the cells are fully spread on the surface via focal adhesion and continue to form fully organized matrices of actin microfilament bundles [130]. In addition to the adhesion mechanism of cells on substrates, it is also important to consider the role hydroxyapatite has in modifying the adhesion behavior of cells.

Hydroxyapatite is a bioactive and biocompatible mineral composite that shares properties and compounds similar to bone and can be prepared using sol-gel, wet, dry, and co-precipitation methods [131-133]. It shares similar composition to hard tissue and has a Ca/P ratio of 1.67 [134]. Hydroxyapatite is generally a crystalline material that can exist either in a semi-crystalline or amorphous form. Nagano et al. discussed that crystalline hydroxyapatite has great potential for extending the longevity of coatings, but also has a higher failure load rate than amorphous hydroxyapatite due to the brittleness and fragility of its crystalline structure [135]. The composition, roughness and porosity of hydroxyapatite is known to affect the cellular response. PLA on its own has very low osteoblast and bioactivity and as a result surface modifications are usually utilized to improve cell signaling, proliferation and surface energy [136]. However, inclusion of hydroxyapatite in the PLA can increase osteoblast activity on its surface by up to 400% [137].

There have been several efforts to understand the role that surface modification and environmental cues have in tuning the adhesion and proliferation behavior of cells [138-142]. Cai et al. demonstrated that surface medication of PDLLA due to hydrolysis or swelling resulted in higher cell viability, greater osteoblast proliferation and attachment [139]. In the work by Cui and Sinko, the osteoblast cell density increased by a factor of 5 within seven days on highly crystalline PGA (Xc: 32%) compared to pure PCL (Xc: 27%) [143]. Washburn et al. determined that the number of MC3T3-E1 cells decreased due to the increased surface roughness (of up to 10nm) from higher crystalline PLLA films [144]. The combination of the results from Cui, Sinko, and Washburn et al. suggest that MC3T3-E1 cells are sensitive to surface roughness on the order of nanometers.

It is also important to consider how hydroxyapatite will integrate with the polymer chain. The quality of the dispersion of hydroxyapatite nanoparticles in polymer films is dependent on the route of synthesis. Hydroxyapatite could be embedded into PLGA, form a inorganic-organic hybrid of PLGA, use chemical bonds to form interpenetrating networks, or bond to the backbone of PLGA [145, 146]. Each mechanism of hydroxyapatite inclusion in PLGA will affect the mechanical strength, miscibility, solubility, and adhesion behavior of cells to the surface. However, in the case of ultrathin PLGA films, more work should be done to understand how crystallization alters the adhesion strength and osteoconductivity of bone cells. The purpose of this chapter is to investigate the adhesion behavior of osteoblast cells to crystallized thin PLGA films in *vitro* and the role of hydroxyapatite in improving the adhesion strength.

## 5.2 Materials and Methods

### 5.2.1 Hydroxyapatite Thin Film Preparation

The same PLGA that was used in the previous chapters, that was obtained from ConMed, was used in solution in chloroform. Hydroxyapatite nanopowder, $Ca_5(OH)(PO_4)_3$, HAp, was purchased from Sigma Aldrich. HAp powder was added to the polymer solution, stirred and sonicated in a water bath to ensure particle dispersion in the polymer solution. The HAp-polymer solution was spin coated on circular glass coverslips for three minutes at a spin speed of 3000rpm. Afterwards, films were annealed at 100°C for 24h to become crystalline or thermally erased at 150°C to remove sample history.

### 5.2.2 Cell Culture

MC3T3-E1 Sublcone 4 preosteoblast mouse cells were purchased from ATCC. The growth medium consisted of 10% GIBCO fetal bovine serum, 1% GIBCO penicillin-streptomycin and Alpha Minimum Essential Medium. Cells were passaged using standard subculture techniques. Cells were incubated at 37°C in a 5% CO2 environment. Medium was changed every two to three days. Cells were grown to 80-90% confluency prior to passaging.

### 5.2.3 Spinning Disk Testing

The spinning disk method was utilized to test the adhesion strength of osteoblast cells to thin films. The spinning disk method uses the shear stress at the surface of the disk to quantify the detachment profile of cells. In this method, cells adhered to disks are rotated at a specific speed in a dextrose spinning buffer. During the spinning of the disk in the fluid, shear stress is applied on the surface of the disk.

$$\tau = 0.800r(\rho\mu\omega^3)^{1/2} \tag{5.1}$$

where $\tau$ is the shear stress at the surface of the disk, $r$ is the radius of the disk, $\rho$ is the fluid density, $\mu$ is the fluid viscosity and, $\omega$ is the angular velocity [147].

The fraction of cells that remain adhered to the disk surface, $f$ can be calculated using the following equation,

(5.2)

$$f = \frac{f_0}{1 + \exp\left[b(\tau - \tau_{50})\right]}$$

The mean shear stress, $\tau_{50}$ represents the average amount of force that it takes for 50% of the cells to detach from the surface. At the center of the disk the amount of detachment force applied can be considered to be zero, because it can be assumed that the forces applied are at the outer edge of the disk [148]. SigmaPlot can be used to generate plots for the shear stress and the amount of adhered cells to the disk surface [149].

Figure 5.1 displays the setup for the spinning disk experiment. The spinning disk chamber was filled with 800mL of dextrose spinning buffer. Circular glass coverslips of 25mm diameter were necessary to match the diameter of the coverslip stage (Figure 5.2). The glass coverslips were held in place on the stage by suction during the course of testing. After testing cells were fixed with formaldehyde, 0.1% triton x-100 and stained with ethidium homodimer-1. The amount of adherent cells was measured with fluorescence microscopy.

### 5.2.4 Statistical Testing

A one-way ANOVA test using a Bonferroni test was used to evaluate the statistical significance of the results. Here, significance was determined by $p<0.05$. Sample sizes were $n \geq 3$.

5.2.5 AFM Imaging

A Digital Instruments atomic force microscope was used to investigate the surface morphology of the hydroxyapatite-PLGA films. Measurements were made using the tapping mode configuration.


Figure 5.1 The spinning disk apparatus setup

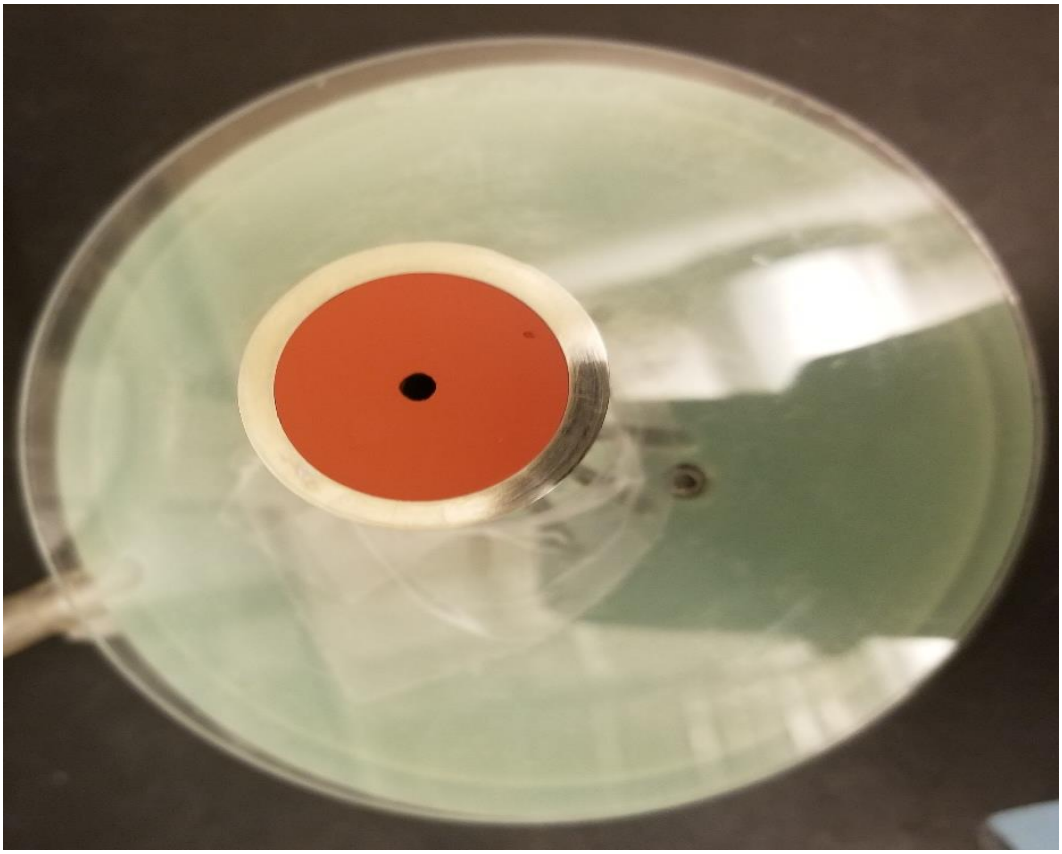

Figure 5.2 The circumference and design of the coverslip stage.

## 5.3 Results and Discussion

200nm films were crystallized for 24h to reach near maximum crystallinity. As mentioned in chapter 3, PLGA films crystallized rapidly and can achieve close to full crystallinity within 24 hours.

### 5.3.1 Adhesion Strength Studies

The adhesion strength of MC3T3 cells adhered to 200nm PLGA thin films treated with hydroxyapatite was tested using the spinning disk apparatus in a dextrose spinning buffer. Prior to testing the adhesion strength, HAp-PLGA films were heated at temperatures above the glass transition temperature of the PLGA film ($T_g$ is 59°C). One advantage of annealing the hydroxyapatite-PLGA films is that it provided an opportunity for the re-arrangement of the polymer chains into a crystalline structure that may have helped to drive the hydroxyapatite nanoparticles into the film. In contrast, when the hydroxyapatite-films are thermally erased, there may not be enough time for chain re-arrangement. This would force the hydroxyapatite nanoparticles to adapt to the polymer chain entanglement from spin casting since the films are immediately removed from the oven and sequentially quenched, preventing surface crystallization from occurring. After HAp-PLGA films finished their heat treatment, MC3T3 cells were adhered to the surface of the films for 24 hours before the adhesion strength test was performed. It is important to note that MC3T3 adhesion occurred in a static environment to model the same environment that was used in the degradation studies. In the static environment design of this present work, there was no dynamic flow rate due to pumps.

The spin speed required to detach cells from the surface ranged between 5000rpm and 5500rpm. Figures 5.3-5.9 provide a general overview and output of the SigmaPlot graphs that demonstrate the relationship of adherent cell fraction to shear stress for thermally erased and 24h annealed crystalline films containing zero HAp to 1:2 HAp. In the SigmaPlot graphs, the adhesion strength that is required to detach 50% of the cells from the surface is measured at the adherent fraction of 0.5. It can be observed from these figures, that as the percentage of HAp increased in the film, there was a shift in the adherent fraction. In figure 5.3, the curve of the shear stress graph is fitted to sigmoidal line. Thermally erased films and 24h crystalline films with no HAp and for thermally erased films with 1:4 HAp about 1000-1100 dyne/cm2 of shear stress was required to completely detach all cells from the film surface (Figure 5.3, 5.4, 5.6-5.7). In contrast, for both the thermally erased and 24h films, large amounts of shear stress of 1400 dyne/cm$^2$ (thermally erased) and 1200 dyne/cm$^2$ (24h) of shear stress was needed to be applied in order to completely detach all cells from the surface (figures 5.5, 5.8-5.9). The complete detachment of all cells from the surface of the film appeared to be more dependent on the percentage of HAp in the film and its corresponding roughness.

TE films lacking hydroxyapatite were considered the control of the experiment and HAp treatments were compared against it. Evaluation of the MC3T3 adhesion strength between crystalline and thermally erased films revealed that there was no statistical difference between the adhesion strength of the thermally erased films and the 24h crystalline films that contained no hydroxyapatite. The average adhesion strength of the thermally erased and crystalline films containing no hydroxyapatite was comparatively at 636 +/-40 dyne/cm$^2$ and 655 +/- 51 dyne/cm$^2$, respectively. Increasing the mass ratio of HAp yielded higher MC3T3 adhesion

strengths on the PLGA films by 1.5 times (figure 5.10). The adhesion strength increased due to the introduction or the presence of HAp in the thermally erased films. TE 1:4 and 24h 1:4 were not statistically different from each other, which indicated that the increase of adhesion strength was due to the presence of HAp and not due to crystallization. The shorter adhesion time for the cells on the surface, helped to ensure that the adhesion strength that was measured was predominately due to changes in roughness and crystallization. If the cells were allowed to be adhered for a longer time period, it would be expected that the adhesion strength would improve with longer adhesion time.

### 5.3.2 Surface Roughness Results

The hydroxyapatite nanoparticles agglomerated in clusters in the 1:4, 1:2 and 1:1 mass ratios of HAp. Measured using afm, the diameter of the nanoparticles was about 400nm and had a height of about 20nm. The large nanoparticle diameter was due to clustering of the nanoparticles and due to the dispersion and miscibility of the nanoparticles in chloroform [146]. Compared to 1:4 HAp, at higher mass ratios there was more nanoparticles covering the surface area of the film (figure 5.11). Interestingly, the HAp nanoparticles seemed to be integrated into the crystalline rods, as seen in the 1:4 HAp afm images. Surface roughness was measured at 10μm scan size in order to adequately compare the surface roughness across the different film treatments. The surface roughness dramatically increased by 9nm for TE films when the lowest mass of HAp, 1:4, was added. Whereas, the surface roughness of the 24h crystallized films increased by 6nm with 1:4 HAp (figure 5.12).

The adhesion strength increased linearly with surface roughness for both the TE and crystallized films. The adhesion strength of the 24h annealed 1:2 and 1:1 treatment groups were higher than the 24h no HAp condition, which indicated that the increase in adhesion strength was due to the presence of HAp (figure 5.13). However, there was a slight reduction in the adhesion strength of the 24h annealed 1:2 and 1:1 treatment groups when compared to the thermally erased films. Considering the large deviation in the TE 1:1 treatment group, it can be concluded that the thermally erased and crystallized films had adhesion strengths fairly similar to each other in the presence of surface roughness. The results of this present study may also present that MC3T3 cells prefer the smoother surfaces of the thermally erased films than the rougher surfaces of the crystallized films. When studying the effects of surface roughness of blends of PDLLA and PLLA on MC3T3-E1, Simon Jr. et al. saw that there was greater cell proliferation on smooth areas of PDLLA within a five day period [150].

## 5.4 Conclusion

The adhesion behavior of MC3T3 osteoblast cells on thermally erased and crystallized PLGA thin film surfaces was investigated. Hydroxyapatite increased the surface roughness of both the crystallized and thermally erased films. Regardless, the adhesion strength of both thermally erased and crystallized thin films significantly improved when hydroxyapatite was incorporated into the film. Future work should include formulation of smaller hydroxyapatite nanoparticles and investigation of the adhesion and osteoconductive behavior of the films in *vitro*.

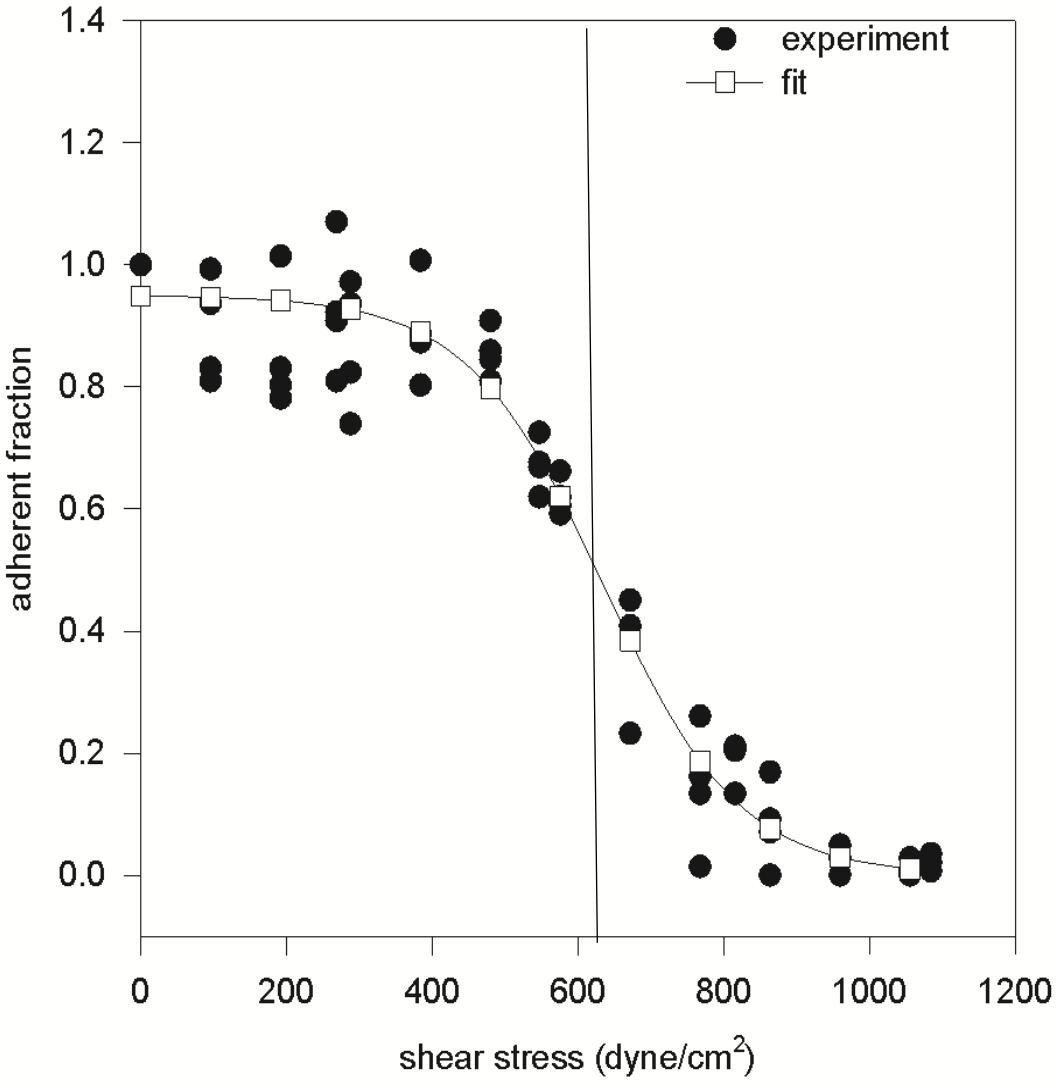


Figure 5.3 The adherent fraction and shear stress plot of thermally erased films with no hydroxyapatite

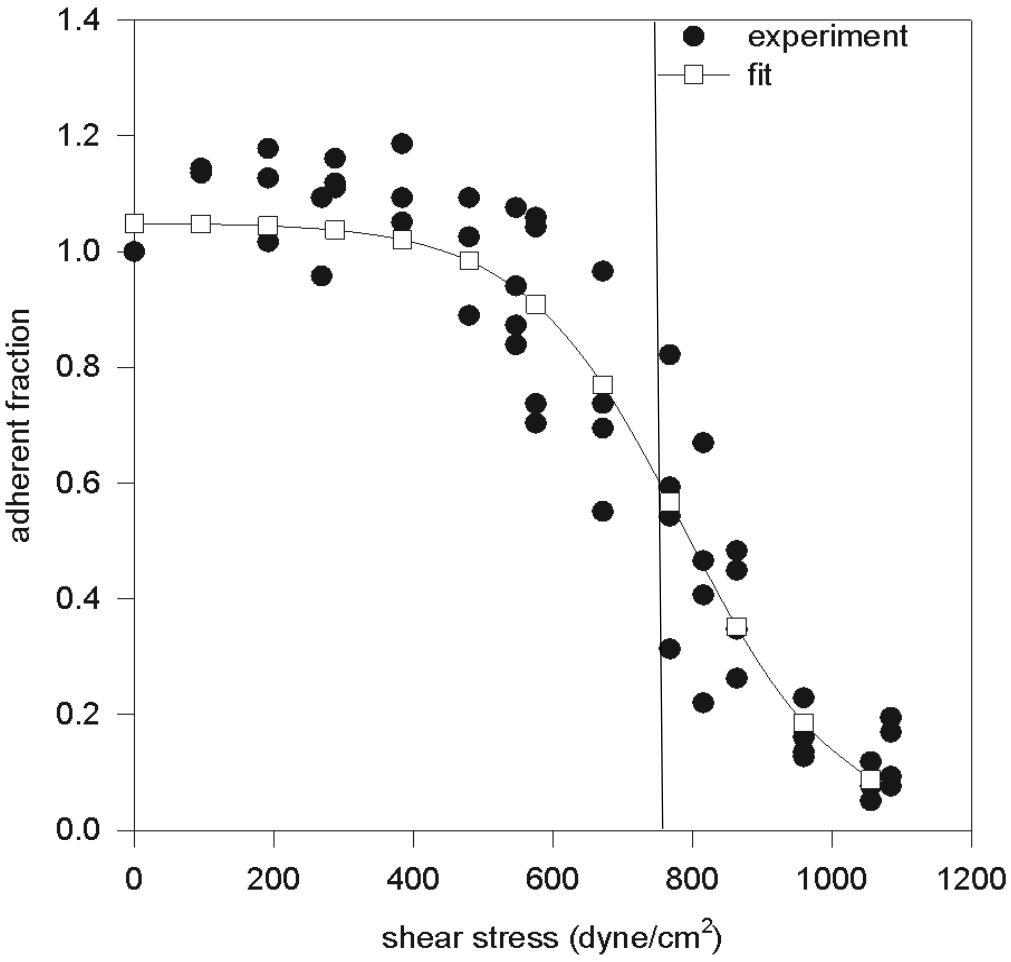


Figure 5.4 The adherent fraction and shear stress plot for thermally erased films containing 1:4 HAp

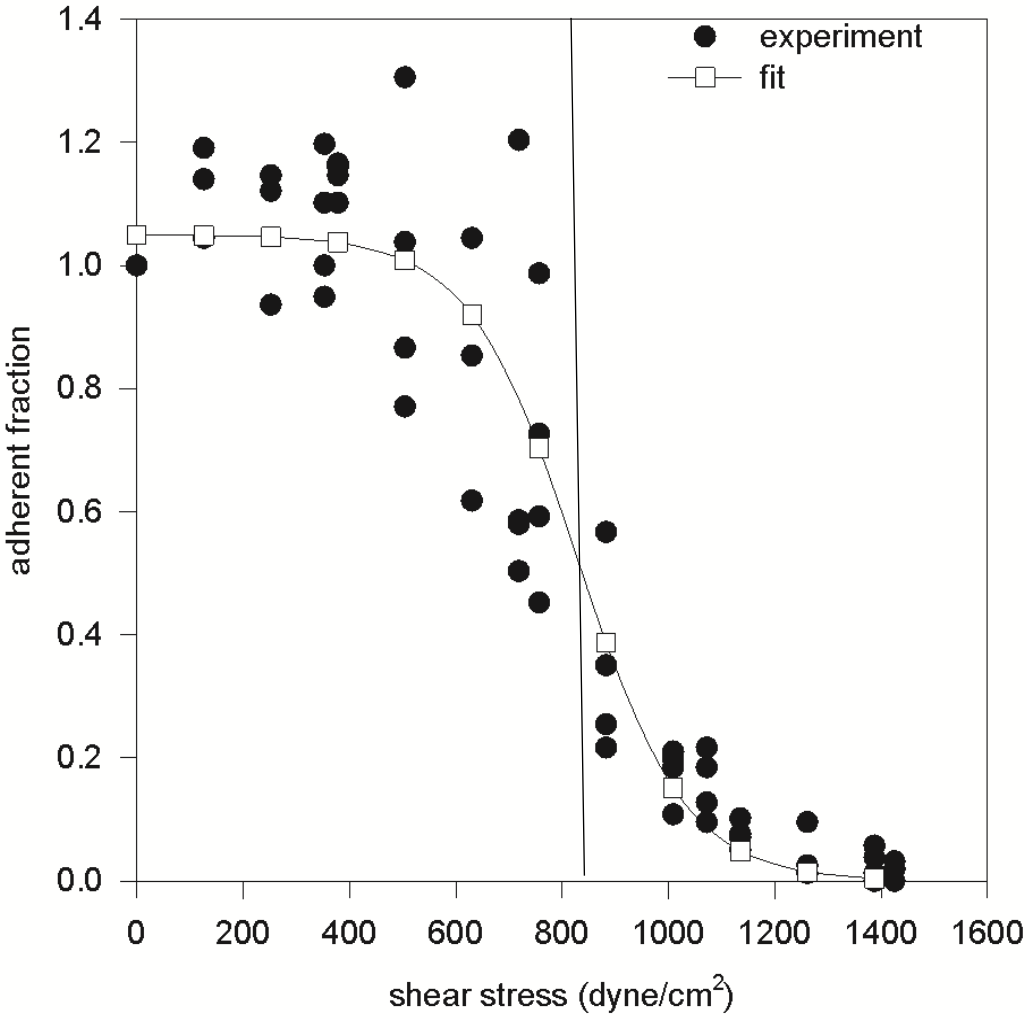


Figure 5.5 The adherent fraction and shear stress of 1:2 HAp thermally erased films

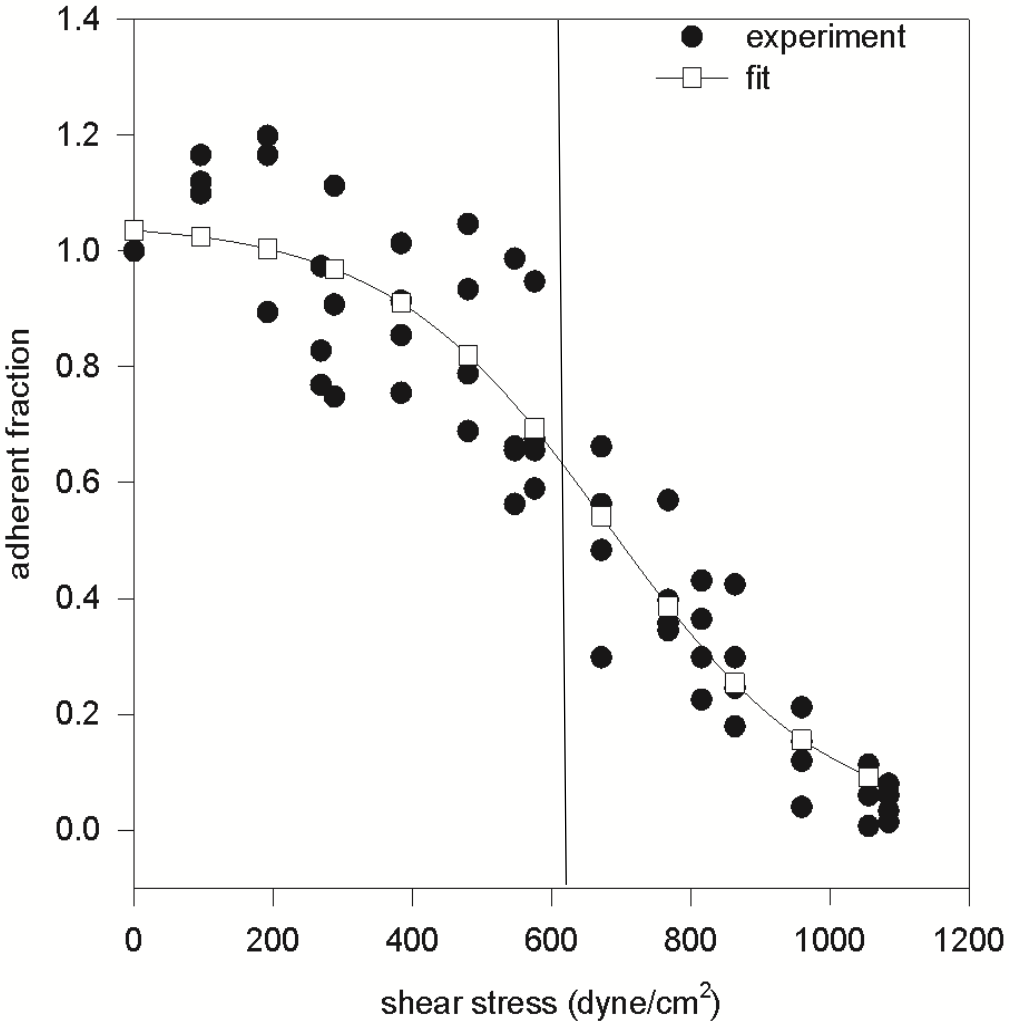


Figure 5.6 A typical plot for the adherent fraction as a function of shear stress for 24h crystallized film containing no HAp

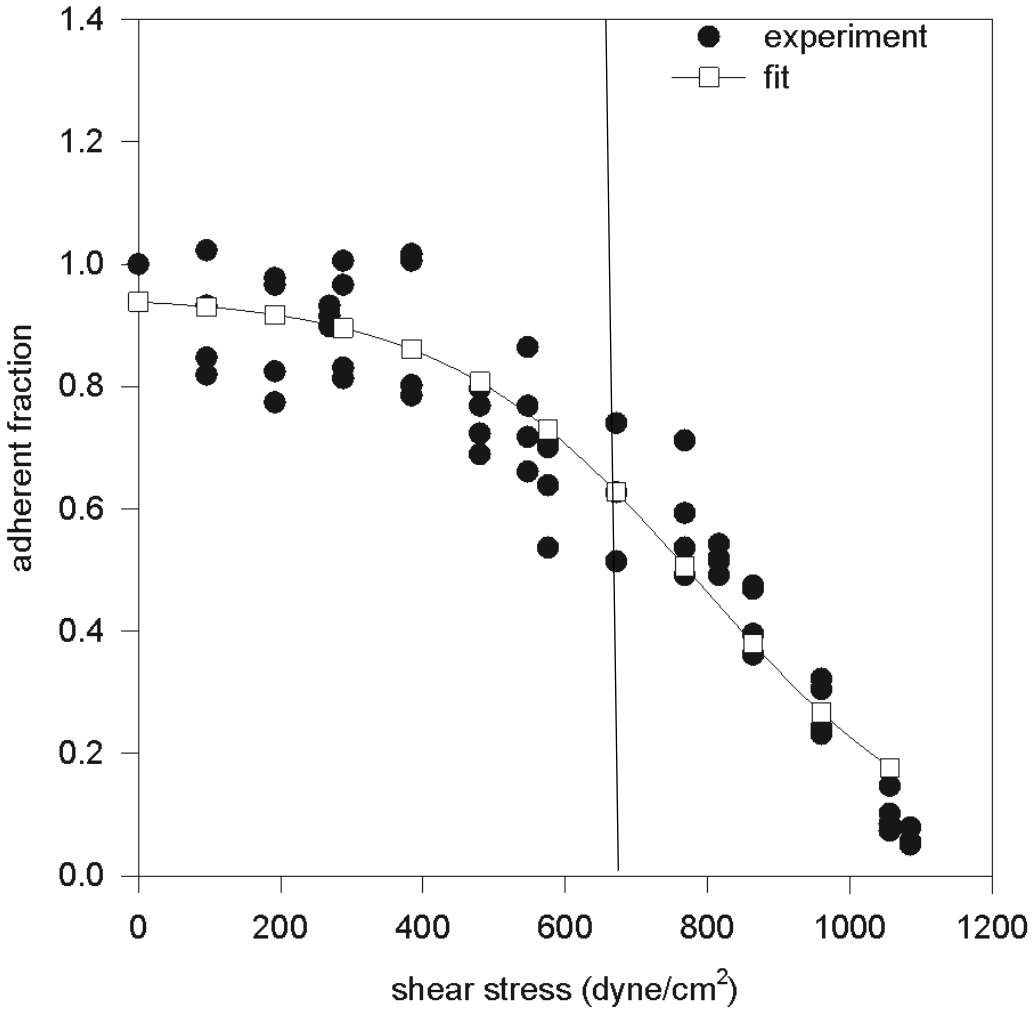


Figure 5.7 A typical plot for the adherent fraction as a function of shear stress for 24h crystallized film containing 1:4 HAp

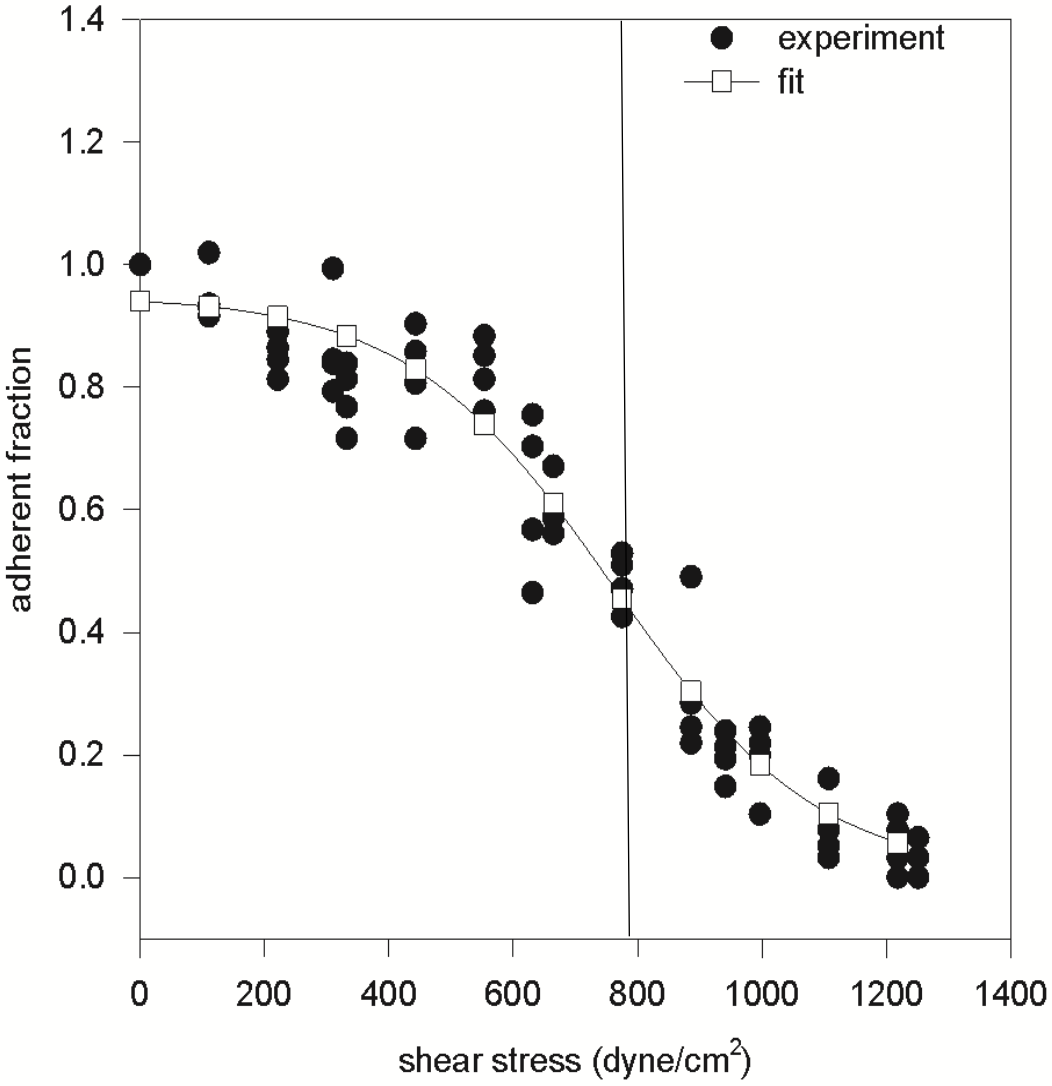


Figure 5.8 A typical plot of the adherent fraction as a function of shear stress for 24h crystallized films containing 1:2 mass ratio of HAp

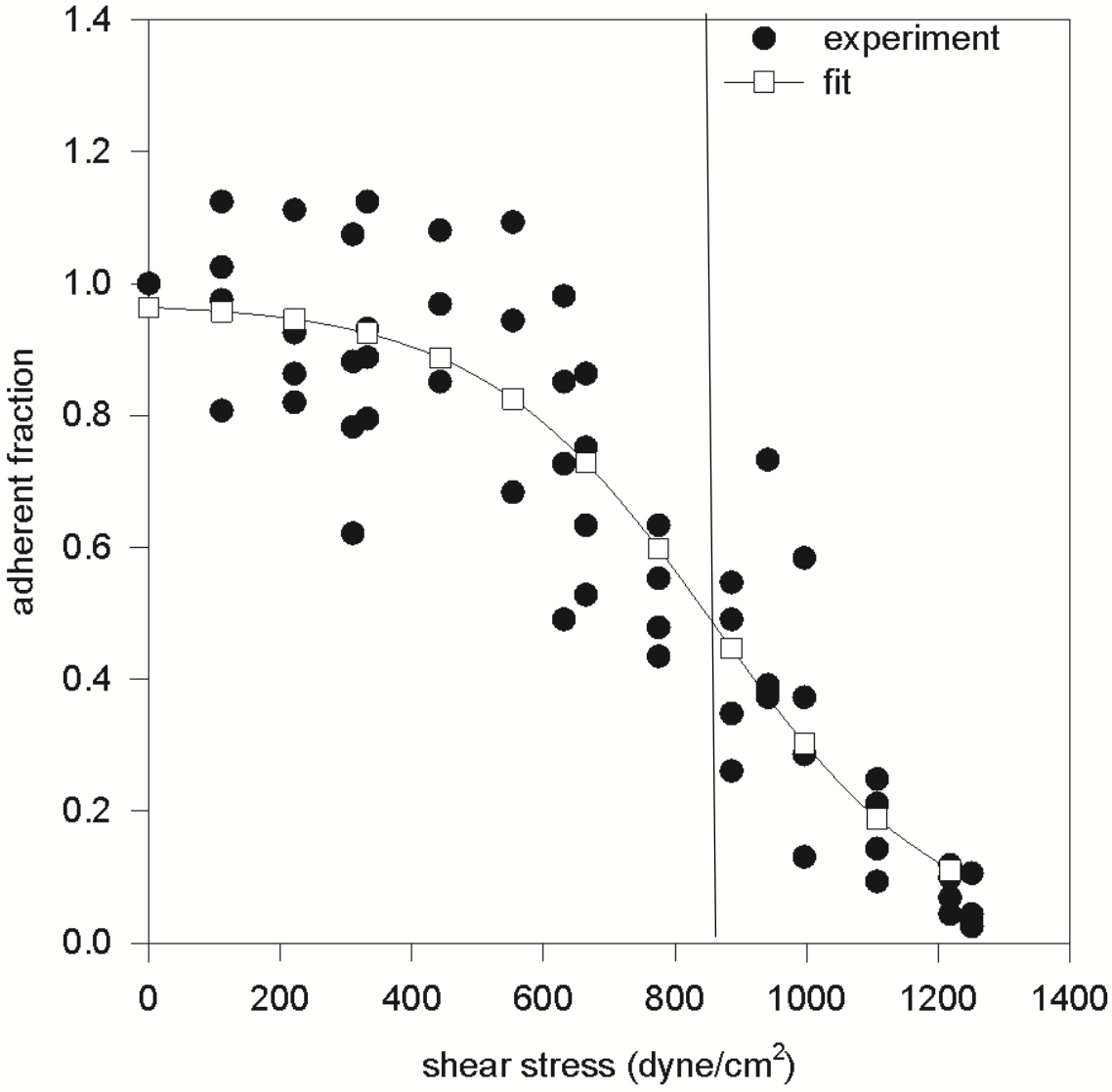


Figure 5.9 A typical plot of the adherent fraction as a function of shear stress for 24h crystallized films containing 1:1 mass ratio of HAp

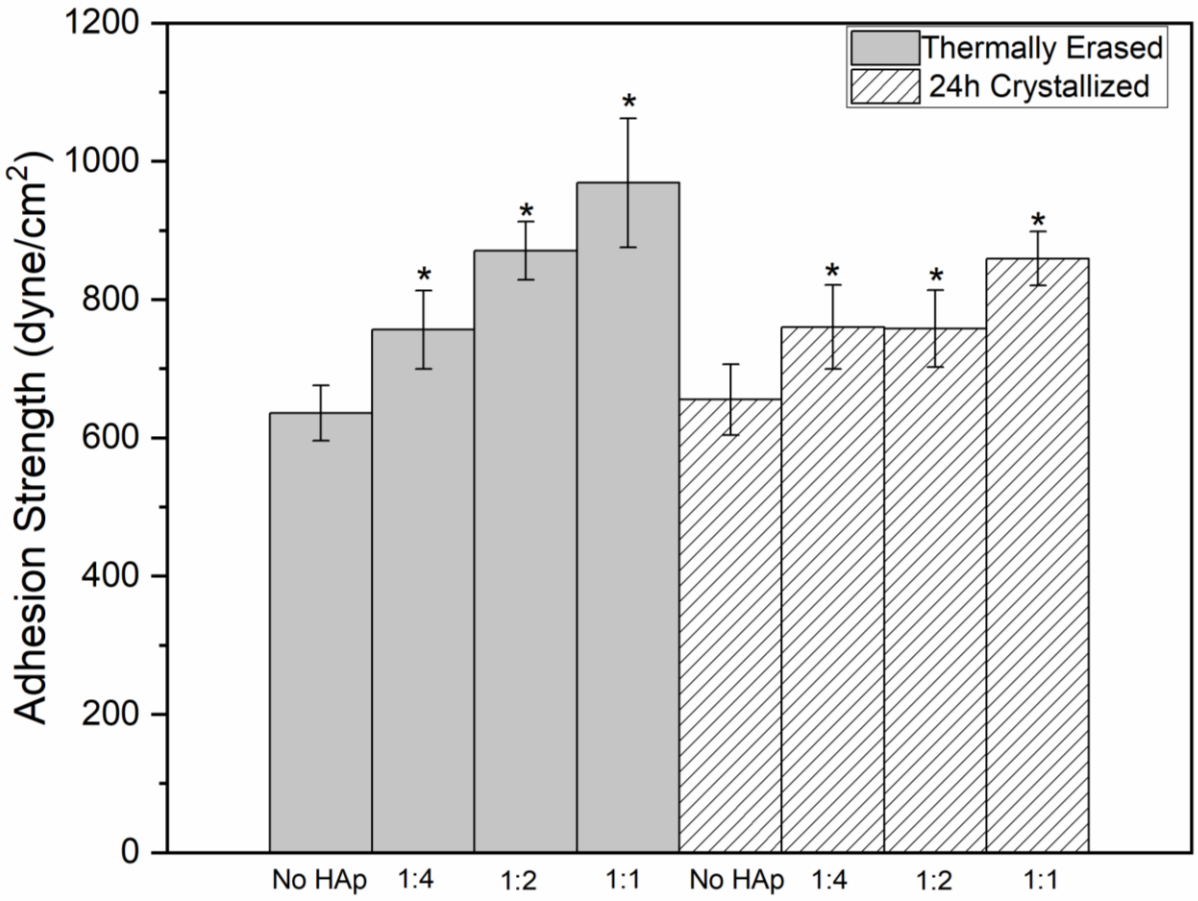


Figure 5.10 Adhesion of MC3T3 cells to crystallized and thermally erased hydroxyapatite treated films

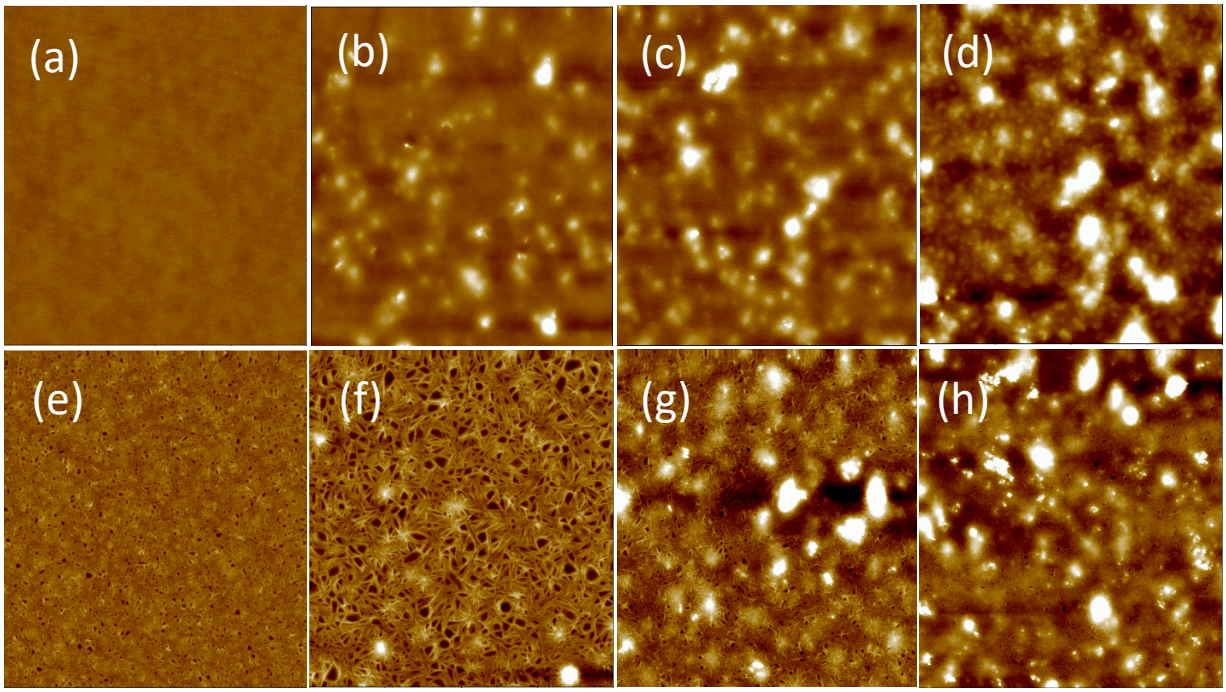


Figure 5.11 Surface morphology of hydroxyapatite-PLGA films. Surface roughness increased with higher doses of HAp. All images were taken at a scan size of 10µm. (a)TE: no HAp, (b)TE: 1:4 HAp, (c)TE: 1:2 HAp, (d)TE: 1:1 HAp; (e)24h: no HAp, (f)24h: 1:4 HAp, (g)24h: 1:2 HAp, (h)24h: 1:1

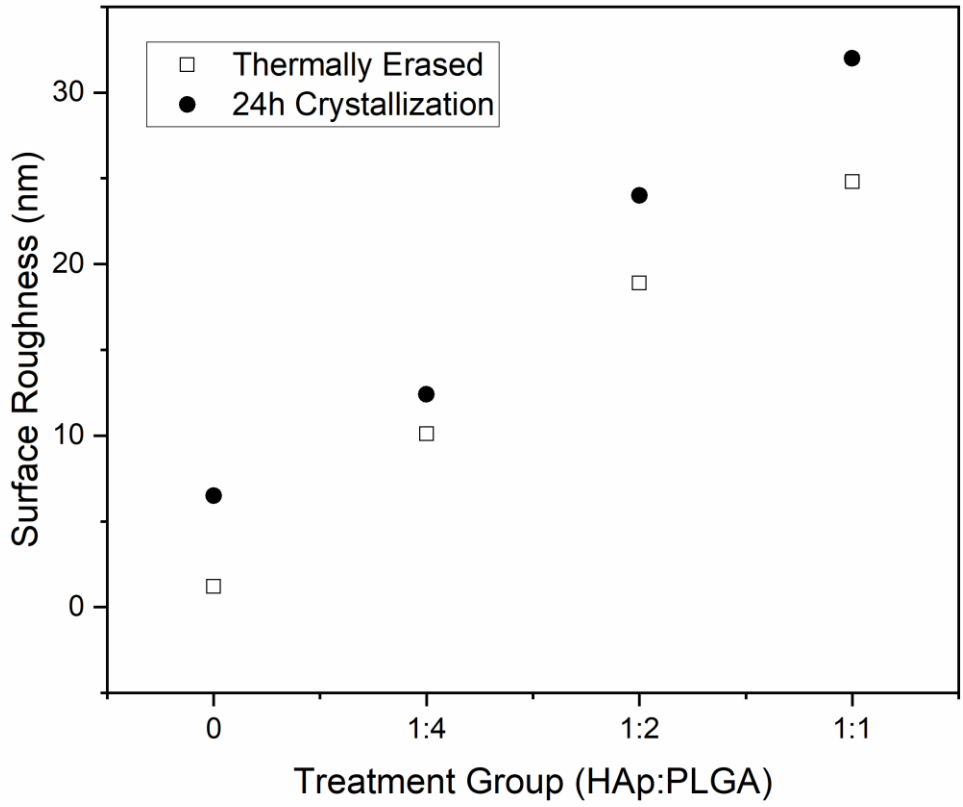


Figure 5.12 Surface roughness of crystallized and thermally erased hydroxyapatite treated films

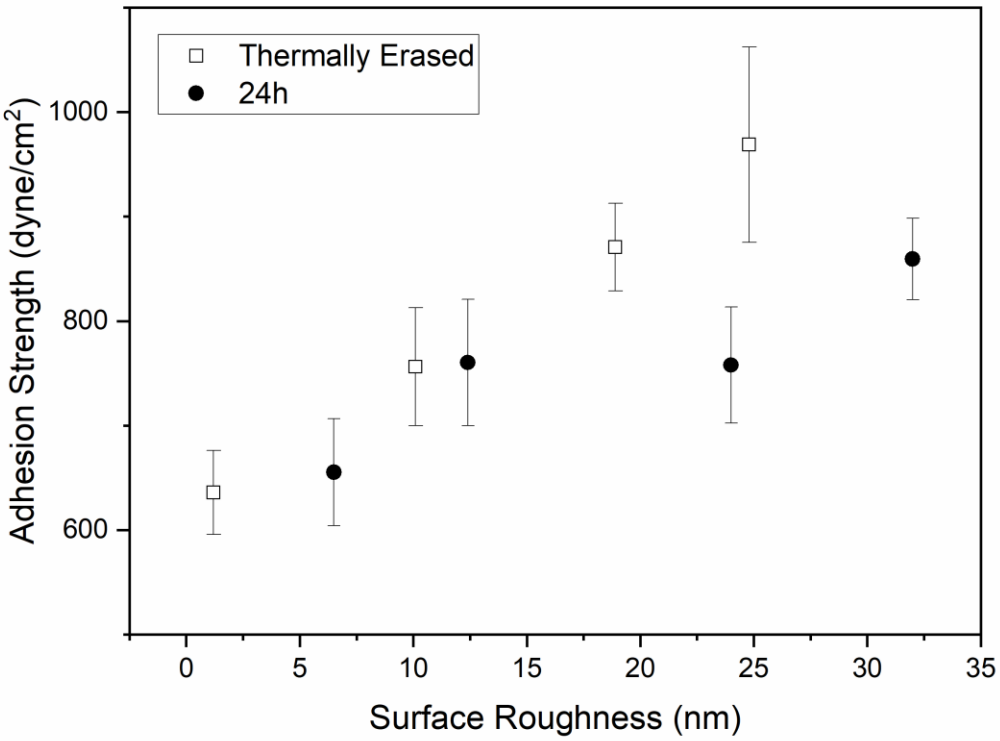


Figure 5.13 MC3T3 adhesion strength increased with surface roughness

# Chapter 6: Conclusion and Future Work

## 6.1 Conclusion

The goal of this dissertation was to determine the viability of using semi-crystalline thin films as coatings for magnesium-based orthopedic implants. This discussion first began by characterizing the crystalline behavior of thin PLGA films ranging from 50 to 200nm. Characterization of the thin films was predominately performed by ellipsometry, differential scanning calorimetry, atomic force imaging, and x-ray diffraction. Following, crystallization was used to tune the degradation of the films. Lastly, the adhesion strength of the osteoblast cells on treated hydroxyapatite crystallized films was evaluated using the spinning disk method. The results from this dissertation demonstrate that hydroxyapatite crystallized thin films can be used as surface coatings for resorbable implants.

To summarize, the key findings of this dissertation were:

- The degree of crystallization shifted the melt temperature by up to 6°C
- Crystallization occurred rapidly in thin films and 60nm films became fully crystalline within 24 hours
- Maximum crystallization was achieved in five days of annealing for thin films versus the seven days for the bulk
- The glass transition temperature on heating was found to be independent of crystallization

- The bulk glass transition temperature on heating was found to be dependent on the heating rate
- The bulk melt temperature and glass transition temperature were found to be independent of heating and cooling rate, respectively
- For films with no sample history, the glass transition temperature was independent of thickness for films ranging between 50nm-200nm
- For films with no sample history, the glass transition temperature was found dependent on thickness for films less than 50nm
- Thermal expansion occurred volumetrically in one-dimension and reduced with higher percentages of crystallinity
- The thermal expansion coefficient was found to be a thickness dependent property
- Thin crystallized layers form on the thin film surface but remained undetectable using ellipsometry
- Surface erosion can be reduced by the presence of crystallization
- The rate of surface erosion was found to be a thickness dependent rate property
- Surface roughness was higher on crystallized films and hydroxyapatite increased surface roughness of both crystallized and thermally erased films
- Incorporation of hydroxyapatite into PLGA coatings resulted in higher osteoblast adhesion strengths
- MC3T3 cells may have nanometer size sensitivity to surface roughness

## 6.2 Future work

The present work investigated the influence of surface roughness, crystallization, and percentage of hydroxyapatite on the adhesion strength of MC3T3-E1 cells to PLGA thin films. It is also important to determine the bioactivity of the thin film surface. Alkaline phosphatase activity can be measured to investigate osteogenic differentiation on the film surfaces. The alkaline phosphatase activity assay is an indicator of osteoblast enzyme activity. To do this, MC3T3 cells can be cultured on thermally erased and crystallized thin films containing 1:4 and 1:1 HAp. Selection of the 1:4 and 1:1 HAp treatments will provide insight into how hydroxyapatite stimulates osteogenic activity. MC3T3 cells can be cultured for three days and seven days to determine initial osteoblast activity on the film surface and osteoblast activity over a longer time period. By seven days, it is expected that the adhesion strength would improve and that there would be high osteoblast activity. To carry out the investigation, cells can be scraped into Tris-HCL and 4-methyl-umbelliferyl-phosphate fluorescent substrate can be added for one hour. The protein concentration can be measured using a Pierce MicroBCA protein assay kit and read with a plate reader at 360nm [151, 152].

Furthermore, in light of the discovery of the thin crystallized surface layers in PLGA thin films, there should be more investigation into the role mobility has in producing crystallized surface layers during cooling. To investigate the dynamics at the free surface of films, relaxation time studies should be performed. Studying the relaxation behavior may provide insight into the time that is required for the films to return to equilibrium under heating and cooling conditions. Additionally, relaxation times will also provide understanding into the relationship of the confinement of the molecular chain groups, silicon substrate, and thermal expansivity. The

relaxation studies should also be coupled with atomic force microscopy imaging in order to develop a visual and mathematical relationship between mobility and surface morphology. These studies can also be done in comparison with bulk PLGA so that the deviations between bulk and thin film behavior can be fully understood.

Future work should also include investigating the dynamic flow behavior of thin films and the adhesion behavior in a dynamic environment. In a dynamic environment, the adhesion strength of osteoblast cells to crystallize films can be simulated for conditions pertinent to the internal body environment. A peristaltic pump can be attached to fluid chamber filled with simulated body fluid. The pump can be used to provide a flow rate consistent with the flow rate of blood and other fluids in the body. The dynamic flow chamber can be simultaneously heated to 37°C to maintain internal body temperature. Films can be prepared at a variety of film thicknesses and immersed in the dynamic flow chamber. Films can be removed on a weekly basis, vacuum dried and the dry thickness can be measured. It would also be interesting to measure the changes to the glass transition temperatures, melt temperature, and thermal expansion coefficient due to fluid dynamics. Additionally, the pH of the fluid in the dynamic flow chamber can also be measured weekly to monitor the contribution of acidity and acidic by-products on the degradation rate.

### 6.2.1 Dynamic Flow Modelling

Figure 6.1 illustrates a conceptual design idea for the dynamic flow chamber. The chamber can be filled with simulated body fluid (SBF) or cell growth medium. The flow rate of the fluid in the chamber can be controlled by a pump in order to investigate the effects of fluid flow rate on the degradation behavior of PLGA thin films and magnesium. The temperature of the chamber can be maintained at 37°C by using a temperature controller and can be changed to test the effects of temperature on different material properties. The sidewalls of the chamber can be adjustable, so that the effects of length and pressure gradients can be understood. An advantage of the flow chamber is that different fluids can be utilized. For cases, where cell testing is desired, growth media can replace the water or simulated body fluid already in the tank. The flow chamber can continue to be modified to accomadate for changes in material size, pressure gradients, and various cell lines.

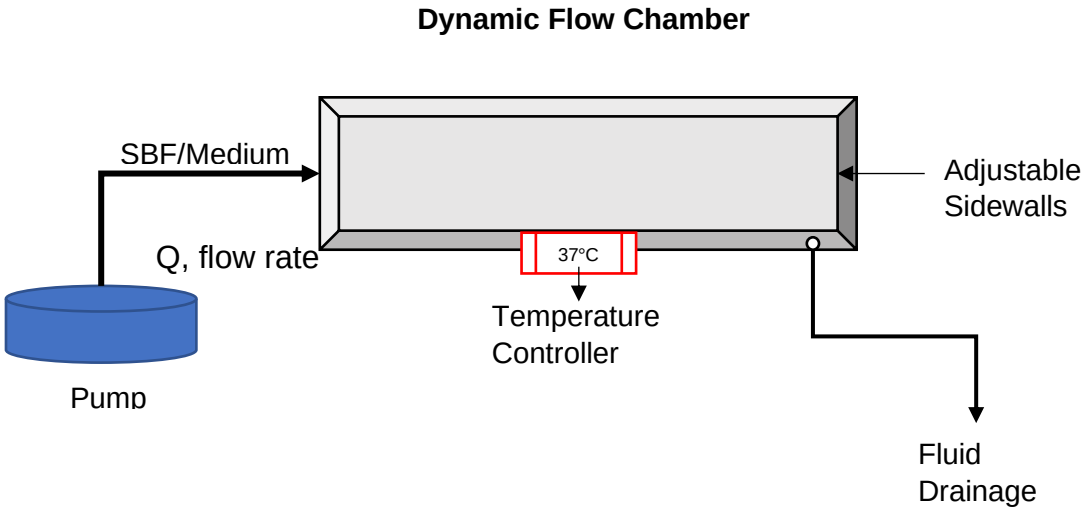


Figure 6.1 A schematic of a dynamic flow chamber for degradation, corrosion and cell adhesion testing

Poiseuille's law can be modified and used to model the blood flow rate, Q, near skeletal and bone tissue for laminar flow [153]. Adaptation of this equation can be used to modify the flow rate in the dynamic chamber and tested for the changes in the pressure gradient. Poiseuille's equation will also be helpful in understanding the relationship between dynamic flow, degradation and corrosion resistance.

$$Q = \frac{\pi r^4 \Delta P}{8\mu L} \tag{6.1}$$

where r is the blood vessel radius, ΔP is change in pressure, μ is the viscosity of the liquid and L is blood vessel length.

Modelling of the corrosivity of the magnesium coated implant can be done using Tafel's equation and the equation for resistivity [153]. The polarization resistance, $R_p$, would reflect the ability of the implant to resist corrosion at varying corrosion currents, $I_{corr}$ and can be studied with degradation time.

$$I = I_{corr}\left(10^{\frac{E-E_{corr}}{\beta_a}} - 10^{\frac{-(E-E_{corr})}{\beta_a}}\right) \tag{6.2}$$

where, I is the current, $E_{corr}$ is the corrosion potential, $\beta_a$ is the anodic Tafel coefficient and $\beta_b$ is the cathodic Tafel coefficient.

$$R_{p,E_{corr}} = \frac{(\beta_a \beta_c)}{I_{corr}(\beta_a + \beta_c) ln10} \tag{6.3}$$

where, $R_{p,Ecorr}$ is the polarization resistance when E = $E_{corr}$.

Furthermore, the dynamic flow chamber can also be used to investigate the role of fluid dynamics on cell adhesion, proliferation, adhesion strength, and surface roughness on glass substrates and hydroxyapatite-PLGA coated films. Evaluation of the adhesion behavior of MC3T3 cells in dynamic flow will also provide insight into the performance of hydroxyapatite-PLGA films for in *vitro* applications. In a static environment, in *vitro* flow is heavily dominated by focal adhesion and integrin binding and there is less environmental factors to disturb cell adhesion. But under dynamic flow, the role of shear stress becomes highly important in order to determine the success of cell adhesion on the substrate, where a collection of different non-covalent bond types must be utilized to ensure adhesion [130].

Contact angle measurements should be performed to test the resistance of the surface coating to water. Because of the hydrophobic nature of PLGA, it would be expected that there would be a high contact angle. Higher degrees of hydrophobicity would result in higher degrees of the surface to repel water. However, it would also be desirable to have some hydrophilic properties, so that there can be permeation of hydroxyapatite out of the film. Water repellent characteristics are important to investigate in order to extend the longevity of the surface coating and inevitably the internal fixation device.

In the present work ATPES was used to promote better adhesion of the film to the silicon wafer substrate. Moving forward, it is also important to optimize the adhesion of PLGA thin films to magnesium-based implants to prevent premature delamination of the films. This could be done by using stronger binding materials or by surface modification of the magnesium alloy. Afterwards, the overall degradation rate of magnesium coated with PLGA can be assessed.

Magnesium can be coated by either spin casting or dip coating and then isothermally annealed to ensure maximum crystallization of PLGA. Coated magnesium should be tested in both static and dynamic environments of simulated body fluid at 37°C in order to account for both the internal body environment and also for the shelf-life of the implants. The surface morphology, surface roughness, and any evidence of pitting and corrosion of coated magnesium associated with degradation should be studied using scanning electron microscopy and atomic force microscopy. The corrosion resistance, mass loss, adhesion strength and osseointegration can be tested. By doing so, evaluation of the design and degradation of crystallized PLGA coated magnesium implants, can be optimized for in *vitro* applications as internal fixation devices. All this information together can be used to design the film for optimal performance as a surface coating for magnesium alloys.

One of the challenges of applying the thin films to the magnesium implants is ensuring that the integrity of the film is maintained. Because the thicknesses of the films are in the range of 200nm or less, there is a higher risk of the films being sheared and destroyed when being tapped or screwed into human bone. A crucial component of future applications of thin surface coatings for orthopedic implants is developing technologies that protect the film during implantation. One way to protect the films is by improving their mechanical properties, fragility and toughness, which could be done by modification of end groups, addition of functional groups, or by utilizing different blends of polymers.

Another alternative to protecting thin films during implantation is by developing rubbery films. Rubbery films may be at a lower risk of tearing because they would be less brittle than rigid films. One way to develop rubbery surface coatings would be by maintaining films above their glass transition temperature or by chemical modification of the polymer. Another way to develop rubbery surface coatings is by utilizing thermoresponsive technologies. For example, the coatings could be maintained in a rubbery state during implantation and after implantation and adjustment to body temperature, the coatings can transform into a glassy state.

With regards to the orthopedic implant, more work should be done to understand how surface coatings tune the glass transition temperatures, the melt temperature, and thermal expansivity of the magnesium material. Understanding the impact that implants have on the thermal properties of surface coatings is also essential in order to control their degradation rate. The release of magnesium ions through the thin films may not only alter the morphology, but also the glass transition temperature and the ability of the film to maintain its crystallinity structure throughout the degradation process. In order to investigate this, magnesium nanoparticles can be incorporated into the thin film, crystallized at 100°C and immersed in simulated body fluid. The glass transition temperature and the quantity of magnesium nanoparticles that leach out of the films can be studied over an extended period of time. Furthermore, this study can be coupled with adhesion strength and osteoblast differentiation studies to understand the impact of magnesium ions on MC3T3 cells.

### 6.2.2 Resorbable Implant Product Concept

In light of the profound discovery in this dissertation, it is possible to develop a product concept for potential magnesium internal fixation devices. The model proposed here is in the form of a screw. A screw was chosen because screws are commonly used in several bone break and fracture procedures. The findings of this dissertation are key in developing this concept model, where tuning the degradation time is primarily controlled by changing the thickness and crystallinity of the thin films. For example, we were able to demonstrate that there were no indications of surface erosion within six weeks for crystallized films and that erosion is thickness dependent. This finding is crucial because the average healing and recovery rate for a broken or fractured bone is between six to eight weeks. The healing time for fracture bonds may correspond nicely with the erosion rate for future thin film PLGA films. Furthermore, the cell adhesion results suggest that there will be osteoblast recruitment and adherence to the injury site, due to hydroxyapatite, which would help to stimulate bone regeneration.

The high glass transition temperature of the PLGA films of 58°C +/- 2°C is advantageous for medical device applications. For example, because both $T_{g,h}$ and $T_{g,c}$ are above body temperature, 37°C, there is less worry about the film transitioning between the glassy and rubbery state. Additionally, because the melt temperature is 140°C, which is over 100°C above body temperature, the films will remain intact and not melt, nor will they crystallize due to evaluated body temperature for cases of increased body temperature due to fever, infection, inflammation where temperatures average about 38°C.

Therefore, the following degradation model was developed. The magnesium screw was designed to be a Cortex self-tapping and nonself-tapping, fully-threaded screw with a 3.5mm diameter, and 10mm in length because they are common sizes for orthopedic screws. Cortex screws are generally used in diaphyseal bone [154, 155]. The outer layer of the screw is a crystallized ultrathin layer of PLGA that has hydroxyapatite incorporated into the film. The inner layer is the bulk magnesium implant. Because of the drug delivery capabilities of PLGA, it may be advantageous to develop a controlled release of HAp out of the thin film to increase the promotion of osteoblast recruitment, while also including an inflammation inhibitor to mitigate the immune response and reduce the chances of infection and inflammation due to implant insertion. The magnesium itself can also be modified to have time-release degradation properties.

Next, we propose four crucial stages for hydroxyapatite-PLGA surface coatings for magnesium orthopedic screws used in bone fractures and breaks. Stage I involves the recruitment and initial adhesion of osteoblast cells to the implant and injury site at the initial time of device implantation. The presence of hydroxyapatite in the film and a controlled release of HAp out of the film should stimulate and help to increase the adhesion strength of the osteoblast cells. Incorporation of inflammatory inhibitors will also help mitigate increased risks of infection. Stage II involves the surface erosion of the hydroxyapatite-PLGA layer over a period of six weeks. Stage III involves surface erosion of the hydroxyapatite-PLGA layer from week six to week twelve. At this point, it is possible that 50-80% of the hydroxyapatite-PLGA layer will be eroded.

During stage I to III, it is assumed that they hydroxyapatite-PLGA remains relatively hydrophobic to repel water and prevent water penetration to the magnesium material itself. Also, during stage I to III, it is expected that bone regeneration is occurring and there is healing of the broken or fractured bone. Stage IV involves the total breakdown of the magnesium device. At this point of time, it is expected that the bone has completely healed, and that the internal fixation device is no longer needed. Fortunately, since magnesium has a rapid degradation rate upon exposure to water, it can be assumed that there will be controlled breakdown of magnesium and the body will resorb the magnesium ions in the small intestine.

## References


[1] U. S. C. Bureau, "2017 National Population Projections Tables: Main Series." [Online]. Available: https://www.census.gov/data/tables/2017/demo/popproj/2017-summary-tables.html

[2] A. C. Looker and S. M. Frenk, "Percentage of Adults Aged 65 and Over with Osteoporosis or Low Bone Mass at the Femur Neck or Lumbar Spine: United States, 2005-2010," pp. 1-6.

[3] C. J. Padilla Colon *et al.*, "Muscle and Bone Mass Loss in the Elderly Population: Advances in diagnosis and treatment," *Journal of Biomedicine*, vol. 3, pp. 40-49, 2018.

[4] C. E. Baker *et al.*, "Bone Fracture Actue Phase Response - A Unifying Theory of Fracture Repair: Clinical and Scientific Implications," *Clinical Reviews in Bone and Mineral Metabolism*, vol. 16, pp. 142-158, 2018.

[5] E. Gomez-Barrena, P. Rosset, D. Lozano, J. Stanovici, C. Ermthaller, and F. Gerbhard, "Bone fracture healing: Cell therapy in delayed unions and nonunions," *Bone*, vol. 70, pp. 93-101, 2015.

[6] S. R. Cummings and M. C. Nevitt, "Non-skeletal Determinats of Fractures: The Potential Importance of the Mechanics of Falls," *Osteoporosis International*, vol. 1, pp. S67-70, 1994.

[7] S. D. Berry and R. Miller, "Falls: Epidemiology, Pathophysiology, and Relationship to Fracture," *Current Osteoporosis Reports*, vol. 6, no. 4, pp. 149-154, 2008.

[8] "Facts and Statistics ". [Online]. Available: https://www.iofbonehealth.org/facts-statistics

[9] R. N. Hansen, A. Pham, S. A. Strassels, S. Balaban, and G. J. Wan, "Compartative analysis of length of stay and inpatient costs for orthopedic surgery patients treated with IV Acetaminophen and IV Opioids vs IV Opioids Alone for Post-Operative Pain," *Advances in Therapy*, vol. 33, pp. 1635-1645, 2016.

[10] V. Sathiyakumar *et al.*, "Patterns of Costs and Spending Among Orthopedic Surgerons Across teh United States: A National Survey," *American Journal of Orthopedics*, pp. E7-E13, 2014.

[11] M. K. Sethi, W. T. Obremskey, H. Natividad, H. R. Mir, and A. A. Jahangir, "Incidence and Costs of Defensive Medicine Among Orthopedic Surgerons in the United States: A

National Survey Study," *American Journal of Orthopedics,* vol. 41, no. 2, pp. 69-73, 2012.

[12] J. Hermans *et al.*, "Productivity Costs and Medical Costs Among Working Patients with Osteoarthritis," *Arthritis Care & Research,* vol. 64, no. 6, pp. 853-861, 2012.

[13] G. de Lissovoy, K. Fraeman, V. Hutchins, D. Murphy, D. Song, and B. B. Vaughn, "Surgical site infection: Incidence and impact on hospital utilization and treatment costs," *American Journal of Infection Control* vol. 37, no. 5, pp. 387-397, 2009.

[14] C. Edwards, A. Counsell, C. Boulton, and C. G. Moran, "Early infection after hip fracture surgery," *The Journal of Bone & Joint Surgery,* vol. 90-B, pp. 770-777, 2008.

[15] R. Radha and D. Sreekanth, "Insight of magnesium alloys and composites for orthopedic implant applications - a review," *Journal of Magnesium and Alloys* vol. 5, pp. 286-312, 2017.

[16] "Magnesium: Fact Sheet for Health Professionals ". [Online]. Available: https://ods.od.nih.gov/factsheets/Magnesium-HealthProfessional/#en1

[17] W. Jahnen-Dechent and M. Ketteler, "Magnesium basics," *Clinical Kidney Journal* vol. 5, pp. i3-i14, 2012.

[18] J. Vormann, "Magnesium: nutrition and metabolism," *Molecular Aspects of Medicine,* vol. 24, pp. 27-37, 2003.

[19] G. Poologasundarampillai and A. Nommeots-Nomm, "Materials for 3D printing in medicine: metals, polymers, ceramics, hydrogels," in *3D Printing in Medicine*: Woodhead Publishing, 2017, pp. 43-71.

[20] B. L. Mordike and T. Ebert, "Magnesium Properties - applications - potential," *Materials Science and Engineering,* vol. A302, pp. 37-45, 2001.

[21] X.-N. Gu and Y.-F. Zheng, "A review on magnesium alloys as biodegradable materials," *Frontiers of Materials Science in China,* vol. 4, no. 2, pp. 111-115, 2010.

[22] M. Niinomi, "Mechanical properties of biomedical titanium alloys," *Materials Science and Engineering* vol. A243, pp. 231-236, 1998.

[23] M. Peron, J. Torgersen, and F. Berto, "Mg and Its Alloys for Biomedical Applications: Exploring Corrosion and Its Interplay with Mechanical Failure," *Metals,* vol. 7, pp. 1-41, 2017.

[24] L.-Y. Li *et al.*, "Advances in functionalized polymer coatings on biodegradable magnesium alloys - A review," *Acta Biomaterialia* vol. 79, pp. 23-36, 2018.

[25] D. Garlotta, "A Literature Review of Poly(Lactic Acid)," *Journal of Polymers and the Environment,* vol. 9, no. 2, pp. 63-84, 2001.

[26] K. Hamad, M. Kaseem, H. W. Yang, F. Deri, and Y. G. Ko, "Properties and medical applications of polylactic acid: A review," *eXPRESS Polymer Letters*, vol. 9, no. 5, pp. 435-455, 2015.

[27] R. Mehta, V. Kumar, H. Bhunia, and A. S. N. Upadhyay, "Synthesis of Poly(Lactic Acid): A Review," *Journal of Macromolecular Science, Part C: Polymer Reviews,* vol. 45, no. 4, pp. 325-349, 2005.

[28] P. Gentile, V. Chiono, I. Carmagnola, and P. V. Hatton, "An Overview of Poly(lactic-co-glycolic) Acid (PLGA)-Based Biomaterials for Bone Tissue Engineering," *International Journal of Molecular Sciences,* vol. 15, pp. 3640-3659, 2014.

[29] H. K. Makadia and S. J. Siegel, "Poly Lactic-co-Glycolic Acid (PLGA) as Biodegradable Controlled Drug Delivery Carrier," *Polymers,* vol. 3, pp. 1377-1397, 2011.

[30] S. M. Davachi and B. Kaffashi, "Polylactic Acid in Medicine," *Polymer-Plastics Technology and Engineering,* vol. 54, no. 9, pp. 944-967, 2015.

[31] R. Z. Khoo, H. Ismail, and W. S. Chow, "Thermal and Morphological Properties of Poly (lactic acid)/Nanocellulose Nanocomposites," *Procedia Chemistry,* vol. 19, pp. 788-794, 2016.

[32] X. Pang, X. Zhuang, Z. Tang, and X. Chen, "Polylactic acid (PLA): Research, development, and industrialization," *Biotechnology Journal* vol. 5, pp. 1125-1136, 2010.

[33] S. Saeidlou, M. A. Huneault, H. Li, and C. B. Park, "Poly(lactic acid) crystallization," *Progress in Polymer Science,* vol. 37, pp. 1657-1677, 2012.

[34] D. M. Bigg, "Polylactide Copolymers: Effect of Copolymer Ratio and End Capping on Their Properties," *Advances in Polymer Technology,* vol. 24, no. 2, pp. 69-82, 2005.

[35] L. Averous, "Chapter 21 - Polylactic Acid: Synthesis, Properties and Applications," in *Monomers, Polymers and Composites from Renewable Resources*, M. N. Belgacem and A. Gandini Eds.: Elsevier, 2008, pp. 433-450.

[36] A. J. R. Lasprilla, G. Martinez, A. R. , B. H. Lunelli, A. L. Jardini, and R. M. Filho, "Poly-lactic acid synthesis for application in biomedical devices - A review," *Biotechnology Advances,* vol. 30, pp. 321-328, 2012.

[37] N. Regibeau, J. Hurlet, R. G. Tilkin, F. Lombart, B. Heinrichs, and C. Grandfils, "Synthesis of medical grade PLLA, PDLLA, and PLGA by reactive extrusion polymerization," *Materials Today Communications,* vol. 24, p. 101208, 2020.

[38] G. Singh, T. Kaur, R. Kaur, and A. Kaur, "Recent biomedical applications and patents on biodegradable polymer-PLGA," *International Journal of Pharmacology and Pharmaceutical Sciences,* vol. 1, no. 2, pp. 30-42, 2014.

[39] T. Casalini, F. Rossi, S. Lazzari, G. Perale, and M. Masi, "Mathematical Modeling of PLGA Microparticles: From Polymer Degradation to Drug Release," *Molecular Pharmaceutics,* vol. 11, pp. 4036-4048, 2011.

[40] O. Kerimoglu and E. Alarcin, "Poly(lactic-co-glycolic acid) Based Drug Delivery Devices for Tissue Engineering and Regenerative Medicine," *Ankem Derg,* vol. 26, no. 2, pp. 86-98, 2012.

[41] J.-M. Lu *et al.*, "Current advances in research and clinical applications of PLGA-based nanotechnology," *Expert Review of Molecular Diagnostics,* vol. 9, no. 4, pp. 325-341, 2009.

[42] J.-W. Park *et al.*, "High strength PLGA/Hydroxyapatite composites with tunable surface structure using PLGA direct grafting method for orthopedic implants," *Composites Part B,* vol. 178, p. 107449, 2019.

[43] R. P. Pawar, S. U. Tekale, S. U. Shisodia, J. T. Totre, and A. J. Domb, "Biomedical Applications of Poly(Lactic Acid)," *Recent Patents on Regenerative Medicine,* vol. 4, pp. 40-51, 2014.

[44] J. S. Price, A. F. Tencer, D. M. Arm, and G. A. Bohach, "Controlled release of antibiotics from coated orthopedic implants," *Journal of Biomedical Materials Research,* vol. 30, pp. 281-286, 1996.

[45] L. J. Smith, J. S. Swaim, C. Yao, K. M. Haberstroh, E. A. Nauman, and T. J. Webster, "Increased osteoblast cell density on nanostructured PLGA-coated nanostructured titanium for orthopedic applications," *International Journal of Nanomedicine,* vol. 2, no. 3, pp. 493-499, 2007.

[46] T. W. J. Steele, C. L. Huang, E. Widjaja, F. Y. C. Boey, J. S. C. Loo, and S. S. Venkatraman, "The effect of polyehtylene glycol structure on paclitaxel drug release and mechanical properties of PLGA thin films," *Acta Biomaterialia,* vol. 7, pp. 1973-1983, 2011.

[47] Z. Lin *et al.*, "Precisely controlled delivery of magnesium ions thru sponge-like monodisperse PLGA/nano-MgO-alginate core-shell microsphere device to enable in-situe bone regeneration," *Biomaterials,* vol. 174, pp. 1-16, 2018.

[48] K. R. Zodrow, J. D. Schiffman, and M. Elimelech, "Biodegradable Polymer (PLGA) Coatings Featuring Cinnamaldehyde and Carvacrol Mitigate Biofilm Formation," *Langmuir,* vol. 28, pp. 13993-13999, 2012.

[49] L. Chen, Y. Sheng, H. Zhou, Z. Li, X. Wang, and W. Li, "Influence of a MAO + PLGA coating on biocorrosion and stress corrosion cracking behavior of a magnesium alloy in a physiological enviornment," *Corrosion Science,* vol. 148, pp. 134-143, 2019.

[50] K. F. Farraro, K. E. Kim, S. L.-Y. Woo, J. R. Flowers, and M. B. McCullough, "Revolutionizing orthopedic biomaterials: The potential of biodegradable and

bioresorbable magnesium-based materials for functional tissue engineering," *Journal of Biomechanics,* vol. 47, no. 9, pp. 1979-1986, 2014.

[51] H. Hornberger, S. Virtanen, and A. R. Boccaccini, "Biomedical coatings on magnesium alloys - A review," *Acta Biomaterialia,* vol. 8, pp. 2442-2455, 2012.

[52] N. J. Ostrowski, B. Lee, A. Roy, M. Ramanathan, and P. N. Kumta, "Biodegradable poly(lactide-co-glycolide) coatings on magnesium alloys for orthopedicd applications," *Journal of Materials Science,* vol. 24, pp. 85-96, 2013.

[53] M. Prakasam, J. Locs, K. Salma-Ancane, D. Loca, A. Largeteau, and L. Berzina-Cimdina, "Biodegradable Materials and Metallic Implants - A Review," *Journal of Functional Biomaterials,* vol. 8, no. 44, pp. 1-15, 2017.

[54] Q. Tian, Rivera-Castaneda, and H. Liu, "Optimization of nano-hydroxyapatite/poly(lactic-co-glycolic acid) coatings on magnesium substrates using one-step electrophoretic deposition," *Materials Letters,* vol. 186, pp. 12-16, 2017.

[55] S.-H. Ye *et al.*, "Biodegradable Zwitterionic Polymer Coatings for Magnesium Alloy Stents," *Langmuir,* vol. 35, pp. 1421-1429, 2019.

[56] G. A. Lakalayeh, M. Rahvar, E. Haririan, R. Karimi, and H. Ghanbari, "Comparative study of different polymeric coatings for the next-generation magnesium-based biodegradable stents," *Artificial Cells, Nanomedicine, and Biotechnology,* vol. 46, no. 7, pp. 1380-1389, 2018.

[57] J. N. Li, P. Cao, X. N. Zhang, S. X. Zhang, and Y. H. He, "In vitro degradation and cell attachemtn of a PLGA coated biodegradable Mg-6Zn based alloy," *Journal of Materials Science,* vol. 45, pp. 6038-6045, 2010.

[58] C. L. Huang, T. W. J. Steele, E. Widjaja, F. Y. C. Boey, S. S. Venkatraman, and J. S. C. Loo, "The influence of additives in modulating drug delivery and degradation of PLGA thin films," *NPG Asia Materials,* vol. 5, pp. 1-11, 2013.

[59] T. Hatanaka *et al.*, "Potential of biocompatible polymeric ultra-thin films, nanosheets, as topical and transdermal drug delivery devices," *International Journal of Pharmaceutics,* vol. 565, pp. 41-49, 2019.

[60] Y. Kikkawa, H. Abe, M. Fujita, Y. Inoue, and Y. Doi, "Crystal Growth in Poly(L-lactide) Thin Film Revealed by in situ Atomic Force Microscopy," *Macromolecular Chemistry and Physics,* vol. 204, pp. 1822-1831, 2003.

[61] Y. Kikkawa, H. Abe, T. Iwata, Y. Inoue, and Y. Doi, "Crystallization, Stability, and Enzymatic Degradation of Poly(L-lactide) Thin Film," *Biomacromolecules,* vol. 3, pp. 350-356, 2002.

[62] Y. Kong and J. N. Hay, "The measurement of the crystallinity of polymers by DSC," *Polymer,* vol. 43, pp. 3873-3878, 2002.

[63] D. Maillard and R. E. Prud'homme, "The crystallization of ultrathin films of polylactides - Morphologies and transitions," *Canadian Journal of Chemistry,* vol. 86, pp. 556-563, 2008.

[64] B. D. Fitz, D. D. Jamiolkowski, and S. Andjelic, "Tg Depression in Poly(L(-)-lactide) Crystallized under Partially Constrained Conditions " *Macromolecules,* vol. 35, pp. 5869-5872, 2002.

[65] W. J. Orts, J. H. van Zanten, W.-l. Wu, and S. K. Satija, "Observation of Temperature Dependent Thickness in Ultrathin Polystyrene Films on Silicon " *Physical Review Letters,* vol. 71, no. 6, pp. 867-870, 1993.

[66] T. Sasaki, N. Yamauchi, S. Irie, and K. Sakurai, "Differential Scanning Calorimetry Study on Thermal Behaviors of Freeze-Dried Poly(L-lactide) from Dilute Solutions," *Journal of Polymer Science: Part B: Polymer Physics,* vol. 43, pp. 115-124, 2005.

[67] O. K. C. Tsui, T. P. Russell, and C. J. Hawker, "Effect of Interfacial Interactions on the Glass Transition of Polymer Thin Films," *Macromolecules,* vol. 34, pp. 5535-5539, 2001.

[68] J. H. van Zanten, W. E. Wallace, and W.-l. Wu, "Effect of strongly favorable substrate interactions on the thermal properties of ultrathin polymer films," *Physical Review E,* vol. 53, no. 3, pp. R2053-R2056, 1996.

[69] B. Borde, H. Bizot, G. Vigier, and A. Buleon, "Calorimetric analysis of the structural relaxation in partially hydrated amorphous polysaccharides. I. Glass transition and fragility," *Carbohydrate Polymers,* vol. 48, pp. 83-96, 2002.

[70] D. Cangialosi, A. Alegría, and J. Colmenero, "Effect of nanostructure on the thermal glass transition and physical aging in polymer materials," *Progress in Polymer Science,* vol. 54-55, pp. 128-147, 2016.

[71] M. Y. Efremov, E. A. Olson, M. Zhang, Z. Zhang, and L. H. Allen, "Glass Transition in Ultrathin Polymer Films: Calorimetric Study," *Physical Review Letters,* vol. 97, no. 8, pp. 085703-1-4, 2003.

[72] C. J. Ellison, S. D. Kim, D. B. Hall, and J. M. Torkelson, "Confinement and processing effects on glass transition temperature and physical aging in ultrathin polymer films: Novel fluorescence measurements," *The European Physical Journal E,* vol. 8, pp. 155-166, 2002.

[73] S. Gao, Y. P. Koh, and S. L. Simon, "Calorimetric Glass Transition of Single Polystyrene Ultrathin Films," *Macromolecules* vol. 46, pp. 562-570, 2013.

[74] Y. Grohens, L. Hamon, G. Reiter, A. Soldera, and Y. Holl, "Some relevant parameters affecting the glass transition of supported ultra-thin polymer films," *The European Physical Journal E,* vol. 8, pp. 217-224, 2002.

[75] C. T. Moynihan, A. J. Easteal, J. Wilder, and J. Tucker, "Dependence of the Glass Transition Temperature on Heating and Cooling Rate," *The Journal of Physical Chemistry,* vol. 78, no. 26, pp. 2673-2677, 1974.

[76] Y. Zhang *et al.*, "Long-range correlated dynamics in ultra-thin molecular glass films," *The Journal of Chemical Physics,* vol. 145, pp. 114502-1-9, 2016.

[77] G. Beaucage, R. Composto, and R. S. Stein, "Ellipsometric Study of the Glass Transition and Thermal Expansion Coefficients of Thin Polymer Films," *Journal of Polymer Science: Part B: Polymer Physics,* vol. 31, pp. 319-326, 1993.

[78] C. B. Roth, K. L. McNerny, W. F. Jager, and J. M. Torkelson, "Eliminating the Enhanced Mobility at the Free Surface of Polystyrene: Fluorescence Studies of the Glass Transition Temperature in Thin Bilayer Films of Immiscible Polymers," *Macromolecules,* vol. 40, pp. 2568-2574, 2007.

[79] M. Bhattacharya, M. K. Sanyal, T. Geue, and U. Pietsch, "Glass transition in Ultrathin Polymer Films: A Thermal Expansion Study," *Physical Review E,* vol. 71, pp. 041801-1-5, 2018.

[80] J. A. Forrest, K. Dalnoki-Veress, and J. R. Dutcher, "Interface and chain confinement effects on the glass transition temperature of thin polymer films," *Physical Review E,* vol. 56, no. 5, pp. 5705-5716, 1997.

[81] B. Frank, A. P. Gast, T. P. Russell, H. R. Brown, and C. Hawker, "Polymer Mobility in Thin Films," *Macromolecules,* vol. 29, pp. 6531-6534, 1996.

[82] J. L. Keddie, R. A. L. Jones, and R. A. Cory, "Size-Dependent Depression of the Glass Transition Temperature in Polymer Films," *Europhysics Letters,* vol. 27, no. 1, pp. 59-64, 1994.

[83] J.-Y. Park and G. B. McKenna, "Size and confinement effects on the glass transition behavior of polystyrene/o-terphenyl polymer solutions," *Physical Review B,* vol. 61, no. 10, pp. 6667-6676, 2000.

[84] P. Rittigstein and J. M. Torkelson, "Polymer-Nanoparticle Interfacial Interactions in Polymer Nanocomposites: Confinement Effects on Glass Transition Temperature and Suppression of Physical Aging " *Journal of Polymer Science: Part B: Polymer Physics,* vol. 44, pp. 2935-2943, 2006.

[85] R. M. A. Azzam and N. M. Bashara, "Reflection and Transmission of Polarized Light by Stratified Planar Structures," in *Ellipsometry and Polarized Light*: North-Holland Publishing Company, 1977, pp. 269-363.

[86] M. V. Massa, K. Dalnoki-Veress, and J. A. Forrest, "Crystallization kinetics and crystal morphology in thin poly(ethyle oxide) films," *The European Physical Journal E,* vol. 11, pp. 191-198, 2003.

[87] B. K. Money and J. Swenson, "Dynamics of Poly(ethylene oxide) around its Melting Temperature," *Macromolecules,* vol. 46, no. 17, pp. 6949-6954, 2013.

[88] S. Kasap, J. Málek, and R. Svoboda, "Thermal Properties and Thermal Analysis: Fundamentals, Experimental Techniques and Applications," in *Springer Handbook of Electronic and Photonic Materials*, S. Kasap and P. Capper Eds., 2 ed.: Springer International Publishing, 2017, pp. 436-446.

[89] N. Saba and M. Jawaid, "A review on thermomechanical properties of polymers and fibers reinforced polymer composites," *Journal of Industrial and Engineering Chemistry,* vol. 67, pp. 1-11, 2018.

[90] D. E. Henton, P. Gruber, J. Lunt, and J. Randall, "Polylactic Acid Technology," in *Natural Fibers, Biopolymers, and Biocomposites*: Bacon Raton, FL: Taylor & Francis, 2005, pp. 527-577.

[91] Y. Wang and J. F. Mano, "Multiple melting behaviour of poly(L-lactide-co-glycolide) investigated by DSC," *Polymer Testing,* vol. 28, pp. 452-455, 2009.

[92] S. Jia, D. Yu, Y. Zhu, Z. Wang, L. Chen, and L. Fu, "Morphology, Crystallization and Thermal Behaviors of PLA-Based Composities: Wonderful Effects of Hybrid GO/PEG via Dynamic Impregnating," *Polymers,* vol. 9, no. 258, pp. 1-18, 2017.

[93] M. Vayer, A. Pineau, F. Warmont, M. Roulet, and C. Sinturel, "Constrained crystallization of poly(L-lactic acid) in thin films prepared by dip coating," *European Polymer Journal,* vol. 101, pp. 332-340, 2018.

[94] P. Badrinarayanan, W. Zheng, Q. Li, and S. L. Simon, "The glass transition temperature versus the fictive temperature," *Journal of Non-Crystalline Solids,* vol. 353, pp. 2603-2612, 2007.

[95] K. Fukao and Y. Miyamoto, "Glass transition temperature and dynamics of α-process in thin polymer films," *Europhysics Letters,* vol. 46, no. 5, pp. 649-654, 1999.

[96] P. Z. Hanakata, J. F. Douglas, and F. W. Starr, "Local variation of fragility and glass transition temperature of ultra-thin supported polymer films," *The Journal of Chemical Physics,* vol. 137, pp. 244901-1-7, 2012.

[97] A. Serghei, M. Tress, and F. Kremer, "Confinement Effects on the Relaxation Time Distribution of the Dynamic Glass Transition in Ultrathin Polymer Films," *Macromolecules* vol. 39, pp. 9385-9387, 2006.

[98] R. Katsumata, A. R. Dulaney, C. B. Kim, and C. J. Ellison, "Glass Transition and Self-Diffusion of Unentangled Polymer Melts Nanoconfined by Different Interfaces," *Macromolecules,* vol. 51, pp. 7509-7517, 2018.

[99] S. Napolitano, E. Glynos, and N. B. Tito, "Glass transition of polymers in bulk, confined geometries, and near interfaces," *Reports on Progress in Physics,* vol. 80, no. 036602, pp. 1-51, 2017.

[100] S. Srivastava and J. K. Basu, "Experimental Evidence for a New Parameter to Control the Glass Transition of Confined Polymers," *Physical Review Letters,* vol. 98, pp. 165701-1-4, 2007.

[101] J. A. Torres, P. F. Nealey, and J. J. de Pablo, "Molecular Simulation of Ultrathin Polymeric Films near the Glass Transition," *Physical Review Letters,* vol. 85, no. 15, pp. 33221-33224, 2000.

[102] S. Loher *et al.*, "Improved degradation and bioactivity of amorphous aerosol derived tricalcium phosphate nanoparticles in poly(lactide-co-glycolide)," *Nanotechnology,* vol. 17, pp. 2054-2061, 2006.

[103] T. Malwela and S. S. Ray, "Enzymatic degradation behavior of nanoclay reinforced biodegradable PLA/PBSA blend composites " *International Journal of Biological Macromolecules*, vol. 77, pp. 131-142, 2015.

[104] Y. Xu, C.-S. Kim, D. M. Saylor, and D. Koo, "Polymer degradation and drug delivey in PLGA-based drug-polymer applications: A review of experiments and theories," *Journal of Biomedical Materials Research Part B: Applied Biomaterials,* vol. 105B, no. 6, pp. 1692-1716, 2017.

[105] A.-C. Albertsson and S. Karlsson, "The Three Stages in Degradation of Polymers - Polyethylene as a Model Substance," *Journal of Applied Polymer Science,* vol. 35, pp. 1289-1302, 1988.

[106] A. Kulkarni, J. Reiche, and A. Lendlein, "Hydrolytic degradation of poly(rac-lactide) and poly[(rac-lactide)-co-glycolide] at the air-water interface," *Surface and Interface Analysis,* vol. 39, pp. 740-746, 2007.

[107] S. C. J. Loo, C. P. Ooi, S. H. E. Wee, and Y. C. F. Boey, "Effect of isothermal annealing on the hydrolytic degradation rate of poly(lactide-co-glycolide) (PLGA)," *Biomaterials,* vol. 26, pp. 2827-2833, 2005.

[108] G. Schliecker, C. Schmidt, S. Fuchs, R. Wombacher, and T. Kissel, "Hydrolytic degradation of poly(lactide-co-glycolide) films: effect of oligomers on degradation rate and crystallinity," *Internal Journal of Pharmaceutics,* vol. 266, pp. 39-49, 2003.

[109] F. von Burkersroda, L. Schedl, and A. Gopferich, "Why degradable polymers undergo surface erosion or bulk," *Biomaterials,* vol. 23, pp. 4221-4231, 2002.

[110] S. Boimvaser, R. N. Mariano, L. N. Turino, and J. R. Vega, "In vitro bulk/surface erosion patter of PLGA implant in physilogical conditions: a study based on auxiliary micropshere systems," *Polymer Bulletin,* vol. 73, pp. 209-227, 2016.

[111] V. Piemonte and F. Gironi, "Kinetics of Hydrolytic degrdation of PLA," *Journal of Polymers and the Environment* vol. 21, pp. 313-318, 2013.

[112] M. Korber, "PLGA Erosion: Solubility- or Diffusion-Controlled?," *Pharmaceutical Research,* vol. 27, pp. 2414-2420, 2010.

[113] G. K. Jain *et al.*, "Mechanistic study of hydrolytic erosion and drug release behaviour of PLGA nanoparticles: Influence of chitosan," *Polymer Degradation and Stability,* vol. 95, pp. 2360-2366, 2010.

[114] S. C. J. Loo, C. P. Ooi, M. L. Tan, and F. Y. C. Boey, "Isothermal annealing of poly(lactide-co-glycolide) (PLGA) and its effect on radiation degradation," *Polymer International,* vol. 54, pp. 636-643, 2005.

[115] K. Numata *et al.*, "Enzymatic Degradation Processes of Lamellar Crystals in Thin Films for Poly[(R)-3-hydroxybutyric acid] and Its Copolymers Revealed by Real-Time Atomic Force Microscopy," *Biomacromolecules,* vol. 5, pp. 2186-2194, 2004.

[116] T. Ponnusamy, L. B. Lawson, L. C. Freytag, D. A. Blake, R. S. Ayyala, and V. T. John, "In vitro degradation and release characteristics of spin coated thin films of PLGA with a "breath figure" morphology," *Biomatter,* vol. 2, no. 2, pp. 77-86, 2012.

[117] M. A. Sabino, J. Albuerne, A. J. Muller, J. Brisson, and P. h. R. E., "Influence of in Vitro Hydrolytic Degradation on the Morphology and Crystallization Behavior of Poly(p-dioxanone)," *Biomacromolecules* vol. 5, pp. 358-370, 2004.

[118] H. Tsuji, "Poly(lactide) Stereocomplexes: Formation, Structure, Properties, Degradation, and Applications," *Macromolecular Bioscience,* vol. 5, pp. 569-597, 2005.

[119] T. Yoshioka, N. Kawazoe, T. Tateishi, and G. Chen, "In vitro evaluation of biodegradation of poly(lactic-co-glycolic acid) sponges," *Biomaterials,* vol. 29, pp. 3438-3443, 2008.

[120] D. Bayraktar and A. C. Tas, "Chemical Preparation of Carbonated Calcium Hydroxyapatite Powders at 37°C in Urea-containing Synthetic Body Fluids " *Journal of the European Ceramic Society,* vol. 19, pp. 2573-2579, 1999.

[121] E. Pamula and E. Menaszek, "In vitro and in vivo degradation of poly(L-lactide-co-glycolide) films and scaffolds," *Journal of Materiasl Science: Materials in Medicine,* vol. 19, pp. 2063-2070, 2008.

[122] M. K. Heljak, W. Swieszkowski, and K. J. Kurzydlowski, "Modeling of the Degradation Kinetics of Biodegradable Scaffolds: The Effects of the Enviornmental Conditions," *Journal of Applied Polymer Science,* vol. 131, p. 40280, 2014.

[123] Y.-y. Huang, M. Qi, M. Zhang, H.-z. Liu, and D.-z. Yang, "Degradation mechanisms of poly(lactic-co-glycolic acid) films in vitro under static and dynamic environment," *Transactions of Nonferrous Metals Society of China,* vol. 16, pp. s293-s297, 2006.

[124] Y. Kang *et al.*, "A comparative study of the in vitro degradation of poly(L-lactic acid)/β-tricalcium phosphate scaffold in static and dynamic simulated body fluid," *European Polymer Journal* vol. 43, pp. 1768-1778, 2007.

[125] C. S. Proikakis, N. J. Mamouzelos, P. A. Tarantili, and A. G. Andreopoulos, "Swelling and hydrolytic degradation of poly(D,L-lactic acid) in aqueous solutions," *Polymer Degradation and Stability,* vol. 91, pp. 614-619, 2006.

[126] H. Y. Tan, E. Widjaja, F. Boey, and S. C. J. Loo, "Spectroscopy Techniques for Analyzing the Hydrolysis of PLGA and PLLA," *Journal of Biomedical Materials Research Part B: Applied Biomaterials,* pp. 433-440, 2009.

[127] E. Vey, C. Rodger, J. Booth, M. Claybourn, A. F. Miller, and A. Saiani, "Degradation kinetics of poly(lactic-co-glycolic) acid block copolymer cast films in phosphate buffer solution as revealed by infrared and Raman spectroscopies," *Polymer Degradation and Stability,* vol. 96, pp. 1882-1889, 2011.

[128] C. Engineer, J. Parikh, and A. Raval, "Effect of copolymer ratio on hydrolytic degradation of poly(lactide-co-glycolide) from drug eluting coronary stents," *Chemical Engineering Research and Design,* vol. 89, pp. 328-334, 2011.

[129] E. Vey *et al.*, "Degradation mechanism of poly(lactic-co-glycolic) acid block copolymer cast films in phosphate buffer solution," *Polymer Degradation and Stability,* vol. 93, pp. 1869-1876, 2008.

[130] A. A. Khalili and R. M. Ahmad, "A Review of Cell Adhesion Studies for Biomedical And Biological Applications," *International Journal of Molecular Sciences,* vol. 16, pp. 18149-18184, 2015.

[131] A. Fihri, C. Len, R. S. Varma, and A. Solhy, "Hydroxyapatite: A review of syntheses, structure and applications in heterogeneous catalysis," *Coordination Chemistry Reviews,* vol. 347, pp. 48-76, 2017.

[132] K. A. Hing, S. M. Best, and W. Bonfield, "Characterization of porous hydroxyapatite," *Journal of Materials Science: Materials in Medicine,* vol. 10, pp. 135-145, 1999.

[133] J. L. Ong and D. C. N. Chan, "Hydroxyapatite and Their Use As Coatings in Dental Implants: A Review," *Critical Reviews in Biomedical Engineering,* vol. 28, no. 5&6, pp. 1-41, 1999.

[134] N. Kantharia, S. Naik, S. Apte, M. Kheur, S. Kheur, and B. Kale, "Nano-hydroxyapatite and its contemporary applications," *Journal of Dental Research and Scientific Development,* vol. 1, no. 1, pp. 15-19, 2014.

[135] M. Nagano, T. Nakamura, T. Kokubo, M. Tanahashi, and M. Ogawa, "Differences of bone bonding ability and degradation behaviour in vivo between amorphous calcium phosphate and highly crystalline hydroxyapatite coating," *Biomaterials,* vol. 17, pp. 1771-1777, 1996.

[136] J. C. Meredith *et al.*, "Combinatorial characterization of cell interactions with polymer surfaces," *Journal of Biomedical Materials Research Part A,* vol. 66A, no. 3, pp. 483-490, 2003.

[137] S. C. Rizzi, D. J. Heath, A. G. A. Coombes, N. Bock, M. Textor, and S. Downes, "Biodegradable polymer/hydroxyapatite composites: Surface analysis and initial attachment of human osteoblasts," *Journal of Biomedical Materials Research,* pp. 475-486, 2001.

[138] A. Abdal-hay, N. A. M. Barakat, and J. K. Lim, "Hydroxyapatite-doped poly(lactic acid) porous film coating for enhanced bioactivity and corrosion behavior of AZ31 Mg alloy for orthopedic applications," *Ceramics International,* vol. 39, pp. 183-195, 2013.

[139] K. Cai *et al.*, "Influence of different surface modification treatments on poly(D,L-lactic acid) with silk fibroin and their effects on the culture of osteoblast in vitro," *Biomaterials,* vol. 23, pp. 1603-1611, 2002.

[140] A. Fuhrmann, A. Banisadr, P. Beri, T. D. Tlsty, and A. J. Engler, "Metastatic State of Cancer Cells May be Indicated by Adhesion Strength," *Biophysical Journal,* vol. 112, pp. 736-745, 2017.

[141] M. Jager, C. Zilkens, K. Zanger, and R. Krauspe, "Significance of Nano- and Microtopography for Cell-Surface Interactions in Orthopaedic Implants," *Journal of Biomedicine and Biotechnology,* vol. 2007, pp. 1-19, 2007.

[142] R. L. Price, K. Ellison, K. M. Haberstroh, and T. J. Webster, "Nanometer surface roughness increases select osteoblast adhesion on carbon nanofiber compacts," *Journal of Biomedical Materials Research Part A,* vol. 70A, no. 1, pp. 129-138, 2004.

[143] H. Cui and P. J. Sinko, "The role of crystallinity on differential attachment/proliferation of osteoblasts and fibroblasts on poly(caprolactone-co-glycolide) polymeric surfaces," *Frontiers of Materials Science,* vol. 6, no. 1, pp. 47-59, 2012.

[144] N. R. Washburn, K. M. Yamada, C. G. Simon Jr., S. B. Kennedy, and E. J. Amis, "High-throughput investigation of osteoblast response to polymer crystallinity: influence of nanometer-scale roughness on proliferation," *Biomaterials,* vol. 25, pp. 11215-1224, 2004.

[145] G. Kickelbick, "Concepts for the incorporation of inorganic building blocks into organic polymers on a nanoscale," *Progress in Polymer Science,* vol. 28, pp. 83-114, 2003.

[146] M. Supova, "Problem of hydroxyapatite dispersion in polymer matrices: a review," *Journal of Materials Science: Materials in Medicine,* vol. 20, pp. 1201-1213, 2009.

[147] A. J. García, P. Ducheyne, and D. Boettiger, "Quantification of cell adhesion using a spinning disc device and application to surface-reactive materials," *Biomaterials,* vol. 18, pp. 1091-1098, 1997.

[148] B. K. Samanta, "Stress distribution in a thin rotating circular disk having transient shearing stress applied on the outer edge," *Journal of the Franklin Institute* vol. 281, no. 4, pp. 315-323, 1966, doi: https://doi.org/10.1016/0016-0032(66)90227-4.

[149] D. Boettiger, "Quantitative Measurements of Integrin-Mediated Adhesion to Extracellular Matrix," in *Methods in Enzymology*, vol. 426: Academic Press, 2007, pp. 1-25.

[150] C. G. Simon Jr., N. Eidelman, S. B. Kennedy, A. Sehgal, C. A. Khatri, and N. R. Washburn, "Combinatorial screening of cell proliferation on poly(L-lactic acid)/poly(D,L-lactic acid) blends," *Biomaterials*, vol. 26, pp. 6906-6915, 2005.

[151] C. A. Gersbach, B. A. Byers, G. K. Pavlath, and A. J. Garcia, "Runx2/Cbfal stimulates transdifferentiation of primary skeletal myoblasts into a mineralizing osteoblastic phenotype," *Experimental Cell Research*, vol. 300, pp. 406-417, 2004.

[152] C. D. Reyes and A. J. Garcia, "α2β1 Integrin-specific collagen-mimetic surfaces supporting osteoblastic differentiation," *Journal of Biomedical Materials Research Part A*, vol. 69A, no. 4, pp. 591-600, 2004.

[153] D. B. Prabhu, P. Gopalakrishnan, and K. R. Ravi, "Coatings on implants: Study on similarites and differences between the PCL coatings for Mg based lab coupons and final components," *Materials and Design*, vol. 135, pp. 397-410, 2017.

[154] N. Douglass and J. Y. Yao, "Nuts and Bolts: Dimensions of Commonly Utlized Screws in Upper Extremity Surgery," *The Journal of Hand Surgery*, vol. 40, no. 2, pp. 368-382, 2015.

[155] E. A. Friis, T. A. DeCoster, and J. C. Thomas, "7 - Mechanical testing of fracture fixation devices," in *Mechanical Testing of Orthopaedic Implants*: Woodhead Publishing, 2017, pp. 131-141.